DANISH METEOROLOGICAL INSTITUTE

—— SCIENTIFIC REPORT ——

02-04

# Numerical ocean and sea ice modelling: the area around Cape Farewell

## Ph.D thesis

**Nicolai Kliem**

Department of Geophysics
Faculty of Science, University of Copenhagen
and
Danish Meteorological Institute


**Copenhagen 2002**

**Title of Thesis:**
Numerical ocean and sea ice modelling: the area around Cape Farewell

**Graduate Student:**
Nicolai Kliem

**Email:**
nk@dmi.dk

**Address:**
Danish Meteorological Institute
Lyngbyvej 100
DK-2100 Copenhagen
Denmark

**Supervisor:**
Carl Christian Tscherning

**Email:**
cct@gfy.ku.dk

**Address:**
Department of Geophysics
Faculty of Science
University of Copenhagen
Juliane Maries Vej 30
DK-2100 Copenhagen
Denmark

Thesis accepted in fulfilment of the requirements
for the ph.d.-degree at the University of Copenhagen.
Submitted: Nov. 1999; Defended: Feb. 2000

DMI Scientific Report
Available from: http://www.dmi.dk/f+u/publikation/vidrap/videnskabrap.html
ISSN 0905-3263 (printed)
ISSN 1399-1949 (online)
ISBN 97-7478-455-2

# Summary

Different aspects of numerical ocean and sea ice modelling are presented. The primary goal is to simulate ocean currents and drift of sea ice in the area around Cape Farewell, Greenland. The study is split into three parts; a study of the pressure gradient error in sigma coordinate ocean models, ocean simulations of the Cape Farewell area, and sea ice simulations of the Cape Farewell area. Of these the first and the last parts cover the major innovations, whereas previously developed models are applied for the ocean simulations.

A study of the pressure gradient error in sigma coordinate ocean models is performed. The error arises in the baroclinic part of the pressure gradient, under conditions of a density stratification above a sloping bed. Different methods for calculation of the gradient are implemented in the Princeton Ocean Model. A laboratory experiment of the circulation in the Skagerrak is used as reference solution. The numerical model is set up similar to the laboratory model, and simulations are performed with different resolutions using a sigma and a $z$-level-based method. The results are compared to those from the laboratory experiment with respect to the general circulation in the area and for current velocities at three different sections. It is concluded that at fine resolution the methods perform similarly and give better results than at coarse resolution. At coarse resolution the sigma method apparently produces good results with respect to the circulation and the surface elevation, but artificial currents are found at the slopes of the Norwegian trench. These flows are reduced using the $z$-level-based method.

The area around Cape Farewell is characterised by the cold and fresh Arctic water found above the warmer and more saline Atlantic water. The current system is strongly controlled by the continental slope close to the coast. Finite element models are applied for this area. Simulations with a linear, diagnostic and a non-linear, prognostic ocean model are performed. The models have previously been applied for shallower coastal regions. An attempt is made to adapt the models to the deep ocean as well by implementing the dependence of the density on pressure in the equation of state. In addition, an optimisation of the prognostic model by implementation of the conjugate gradient is investigated. Simulations with and without wind stress and baroclinic effects are performed. The simplest simulation, performed for a barotropic ocean without influence of the wind, gives a reasonable picture of the current system and velocities in agreement with measurements. Hence it is concluded that there is a large barotropic component in the surface currents in this region.

A finite element sea ice model is developed and implemented for the Cape Farewell area. The model calculates the ice drift based on wind, sea surface elevation and current, Coriolis force, and internal ice stress. Initial conditions are based on observations of sea ice concentration, wind fields are received from an operational atmospheric model, and sea surface elevation and current are obtained from the diagnostic ocean simulation. Ice drift is simulated for a period of 10 days, and the results are compared with observations of ice concentration. Different ice rheologies are tested. Furthermore, sensitivity tests of different model coefficients are performed. The model

results are in agreement with observations, thus it is reasonable to expect that the model can be used to predict ice drift in this area. A set-up for an operational forecasting system is proposed. In addition, several directions for further development of the model are given.

In order to include the interaction between the sea ice and ocean, the ice model is coupled to the prognostic ocean model. This is performed through the ice-ocean stress and the sea surface tilt. At first the results for the ice drift are not improved, compared to the sea ice simulations with an ocean at steady state. It is believed that this is partly because of the relatively short time scale, and that better results would be obtained by using other values of the drag coefficients.

# Dansk resumé

Forskellige aspekter ved numerisk ocean og havis modellering præsenteres. Det primære mål er at kunne simulere havstrømme og isdrift i området omkring Kap Farvel, Grønland. Arbejdet er delt op i tre dele; en undersøgelse af fejlen ved beregningen af den horisontale trykgradient i sigma-koordinat ocean modeller, simulering af havstrømme i Kap Farvel området, samt simulering af isdrift i Kap Farvel området. Heraf indeholder første og sidste del de væsentligste nyskabelser, mens der for ocean simuleringerne er benyttet tidligere anvendte modeller.

Der er foretaget en undersøgelse af fejlen ved beregningen af den horisontale trykgradient i sigma-koordinat ocean modeller. Fejlen opstår i den barokline del af trykgradienten, hvis der er en densitetsstratifikation over en skrånende bund. Forskellige metoder til beregningen af gradienten er implementeret i Princeton Ocean Modellen. Et laboratorie-eksperiment over cirkulationen i Skagerrak benyttes som referenceløsning. Den numeriske model er sat op svarende til laboratorie-modellen, og der er foretaget simuleringer med forskellige opløsninger med en sigma og en $z$-niveau-baseret metode. Resultaterne er sammenlignet med laboratorie-modellen på den generelle cirkulation i området samt på strømhastigheder i tre forskellige snit. Det konkluderes, at begge metoder giver bedst resultat ved fin opløsning. I den fine opløsning ligner resultaterne hinanden med de to metoder. I den grovere opløsning giver sigma metoden tilsyneladende fine resultater med hensyn til cirkulationen i Skagerrak, men fejlagtige strømme er fundet på skråningerne af Norske Renden som en følge af fejlen i trykgradienten. De fejlagtige strømme reduceres med den $z$-niveau-baserede metode.

Kap Farvel området er kendetegnet ved at koldt Arktisk vand findes over varmere og mere salt Atlantisk vand. Strømforholdene er kraftigt styret af kontinentalskråningen, som findes tæt ved kysten. Endelig element modeller er anvendt for dette område. Der er foretaget simuleringer med en lineær, diagnostisk samt en ikke-lineær, prognostisk ocean model. Modellerne er tidligere fortrinsvis anvendt for mere lavvandede kystområder, men er her søgt tilpasset området ved implementering af densitetens afhængighed af tryk i tilstandsligningen. Desuden er der foretaget en undersøgelse af muligheden for en optimering af den prognostiske model ved implementering af konjugeret gradient metoden til løsning af et system af lineære ligninger. Der er foretaget simuleringer med og uden vindpåvirkning og barokline effekter. Den simpleste simulering, foretaget for et barotropt ocean uden vindpåvirkning, giver et rimeligt billede af strømforholdene med strømhastigheder, der er i overensstemmelse med målinger. Det konkluderes deraf, at der er en kraftig barotrop komponent i overfladestrømmene i området.

En endelig element havis model er udviklet og sat op for Kap Farvel området. Modellen beregner isdriften på baggrund af vind, overfladestrøm, hældningen af havoverfladen, Coriolis kraften samt interne kræfter i isen. Begyndelsesbetingelser er baseret på observationer af iskoncentration, vindfelter fås fra en operationel meteorologisk model, og havoverfladehældning og -strøm fås fra den diagnostiske ocean simulering. Isdriften er simuleret for en 10 dages periode, og resultaterne er sammenlignet med observationer af iskoncentration. Der er foretaget test med forskellige udtryk

for isens interne kræfter. Desuden er der foretaget sensitivitetstests for forskellige koefficienter, der indgår i modellen. Modelresultaterne er i rimelig overensstemmelse med observationer, og der er grund til at antage, at modellen kan benyttes til forudsigelse af udbredelsen af havis i området. Der gives forslag til en opsætning af modellen for operationel brug. Der gives desuden flere forslag for yderligere udvikling af modellen.

For at inkludere vekselvirkningen mellem ocean og is er ismodellen koblet til den prognostiske oceanmodel. Dette er sket gennem is-ocean friktionsleddene, samt via havoverfladehældningen. Resultaterne for isdriften er ikke umiddelbart forbedret i forhold til havis-simuleringerne med et stationært ocean. Det skønnes, at dette til dels skyldes den relativt korte tidsskala, og at bedre resultater ville kunne opnås ved benyttelse af andre værdier for friktionskoefficienterne.

# Preface

This thesis is the culmination of my Ph.D. project. I have finally made a version suitable for publication in the DMI scientific report series.

The thesis is written with blood, sweat, toil, and tears. When I started the study, I expected that writing the thesis would be the hardest part. I was right. I have had some hard months, and it has been necessary to neglect my daughter and my wife. Nevertheless, I think it was worthwhile doing it. I have learned so much during the study. I enjoy, what I am doing, and I have had three good years.

I spend the fall 1998 at the Institute of Marine Research in Bergen. I am happy, I had the opportunity to go abroad. It was a very inspiring time. Actually, most of the work presented here was made in Bergen; suddenly the ocean simulations gave decent results, and there the sea ice model was developed and coded. I even had the opportunity to give a presentation on the pressure gradient stuff, and got some useful response on that. My family was there as well. We liked the city and enjoyed the nature and surrounding mountains.

Before I started, I neither knew about sea ice modelling nor about the finite element method. Now, I suddenly have the feeling that I am at the frontier of numerical ocean modelling. I really do believe in the finite elements and the use of unstructured grids for ocean models, and I feel privileged to be in the Quoddy User's Group.

I have tried to document my work so far. I hope this text is of use for other people, and can inspire other students. There is still much to be developed on the sea ice model. I have tried to pass on some of my ideas for future work.

# Acknowledgements

I am grateful to all the people that have helped while preparing this thesis. Two persons deserve a special thanks; Julie D. Pietrzak, who got me to start the Ph.D. project, and is co-author on the enclosed paper, and Paul Budgell, who suggested that I look into the finite element method, and was a great host and advisor, while I was visiting the Institute of Marine Research in Bergen during the fall 1998.

I would like to acknowledge my supervisor Professor Carl Christian Tscherning for the guidance and inspiration given throughout the work. I would also like to acknowledge the head of the oceanographic section at the Danish Meteorological Institute, Erik Buch, for the motivation and for helping me structure the thesis. Professor Stig Skelboe is acknowledged for the advice on the implementations in Quoddy, and Thomas McClimans is acknowledged for making the comparison to his laboratory experiment possible.

All (present and former) members of the ocean group at the Danish Meteorological Institute were very helpful to this work. Furthermore, the Quoddy User's Group meetings which I attended during the work, were indeed very inspiring. The crew at the vessel "M/S Kista Arctica" kindly provided information on ice thickness.

My English is far from perfect. I would like thank Paul Budgell, Jacob Woge Nielsen and Mads Hvid Nielsen for correcting the text.

I will not thank my daughter Freja, on the contrary I will blame her. I am sure I would have reached much further, if it were not for her. With her beauty, exceptional good mood and happiness she made it difficult to stay at the computer. Instead I will thank Freja's grandparents, great-grandmother and of course Bodil, my wife and Freja's mother, for taking over in the final phase of writing the thesis.

The project was funded jointly by the Danish Research Academy and the Danish Meteorological Institute.

# Contents

# List of Figures

# List of Tables

# Chapter 1

# Introduction

The objective of this study is to investigate different aspects of numerical ocean and sea ice modelling, on a relative small spatial scale of a few kilometres and time scales of a few days. The primary aim is to be able to predict sea ice drift in the area around Cape Farewell and southern Greenland. On a longer perspective the aim is to be able to predict the ocean state not only around Cape Farewell, but in Greenland waters in general. By the ocean state is meant the sea ice and surface ocean conditions, as well as the conditions at depth.

The Danish Meteorological Institute produces maps of sea ice concentration in the Cape Farewell area. The maps are mainly used for safety of navigation and are produced every 2-3 days. They are based on remote sensing, that is, satellite-borne measurements primarily from Radarsat, and by airborne measurements with a specially-equipped aircraft and helicopter. Development of the service system goes in two directions. One is to exploit the number of different kinds of satellite observations (Gill and Valeur, 1996; Gill, 1998; Gill and Valeur, 1999). The other is to use numerical models to predict sea ice drift, in order to produce forecasts of the ice extent a few days ahead. The latter approach is represented by this study.

The currents transporting the ice along the Greenland coast are to a large degree influenced by the continental slope. All the way along the east and southwest Greenland coast the distance between the slope and the coast is less than a few hundred kilometres and in the Cape Farewell area the shelf is only 50-100 km wide. To resolve both the shallow shelf and the continental slope, it is advantageous to exploit the terrain following $\sigma$-coordinate in the vertical giving a smooth representation of the bathymetry. On the other hand, the $\sigma$-coordinate is known to give errors on the pressure gradient calculation in the case of a density stratification over a sloping bed. This is the case in the Cape Farewell area, where the fresh Arctic water of the East Greenland Current lies above the more saline water. There does not seem to be consensus in the literature of the importance on the error. In order to use a well-defined test with a known reference solution, consideration of the Greenland waters will be postponed while the Skagerrak area including the north-eastern North Sea and the Kattegat is simulated instead. The pressure gradient error is of general relevance and applies to the Skagerrak, as well. Furthermore, the results of a laboratory experiment for that area are available as a benchmark for the numerical models.

The study of the pressure gradient error is performed with the Princeton Ocean Model (POM), which uses the finite difference method. For various reasons, the finite element method is used for the simulations of the Cape Farewell area.

The two finite element ocean models, Fundy and Quoddy, are used for the simulations of the Cape Farewell area. They are diagnostic and prognostic, respectively, and were originally

developed for coastal ocean simulations. Here they will be used for deep ocean simulations, as well. This capability has already been demonstrated by a simulation of the North Atlantic (Greenberg et al., 1998), and in a simulation of the continental slope off the west Canadian coast (Foreman and Thomson, 1997). Other models developed for shallow water have been used in deep water with success. POM, for example, is now frequently used as a general-purpose model, and is applied to such different cases as estuarine exchange through a narrow inlet of 2.5 km width (Wheless and Vale-Levinson, 1996), the Atlantic (Ezer and Mellor, 1997; Häkkinen, 1999; Gan et al., 1998), and the Arctic coupled with a sea ice model (Häkkinen, 1993).

The main innovation in this work is the development of a finite element sea ice model. It is a dynamic model that simulates the ice drift forced by wind and ocean current, and the sea surface tilt. The governing equations are basically the same as in most other sea ice models. The ice is assumed to be a continuum having a thickness, an area concentration and a velocity, and the evolution with time is described by continuity equations and a momentum equation. In continuous form these are written as partial differential equations. The models differ in the physics through the parameterisation of the internal ice stress and in the numerical formulation. The model presented here is able to resolve the ice edge and other interesting features, exploiting the unstructured grid and varying resolution of the finite element method. In most applications sea ice models are set up for a much larger scale with a climate perspective, such as for simulating the entire Arctic Ocean. Here the model is used on other length and time scales. However, it is still a large-scale simulation in the sense that the length scale of the mesh is much larger than a typical floe size and the continuum description of the ice is applied.

Altogether, the work presents some of the important aspects of numerical modelling with special focus on the ocean and sea ice condition in the Cape Farewell area. An attempt is made to build up the thesis in a natural order starting with a fundamental problem of ocean modelling, then showing some ocean simulations, and ending with the development of a sea ice model and simulations of the ice drift.

The thesis is outlined as follows. The study of the horizontal pressure gradient does not apply directly to the Cape Farewell area, but is of general relevance and is presented in Chapter 2. The rest of the thesis concerns the Cape Farewell area. Chapter 3 describes the hydrography of the area, and the data available for initial values, forcing and validation. The ocean models and simulations are presented in Chapter 4. The sea ice model is presented in Chapter 5, together with simple tests of the model and simulations of the drift of sea ice around Cape Farewell. In addition, a section describing the coupling of the sea ice model to the prognostic ocean model and a simulation with the coupled ice-ocean model is included.

Brief descriptions of the basics of the numerical methods used in the study are given in appendices. An introduction to the finite difference and finite element methods is given in appendix A, while appendix B gives a brief outline of the power method and how to calculate the condition number. Finally internet addresses for most of the data and programs that are used in the work are collected in appendix C.

# Chapter 2

# Sigma coordinates in ocean models

## 2.1 Introduction

This chapter deals with the truncation error in the numerical calculation of the horizontal pressure gradient in $\sigma$-coordinate ocean models. This problem arises when a vertical density stratification is present and the bed is sloping, as is the case in the Cape Farewell area.

The problem has been recognised in atmospheric models for many years, and Haney (1991) brought the problem to the attention of ocean modellers as well. While Haney (1991) argues that the error might be serious, Mellor et al. (1994) found that the error is of only minor relevance and that the temperature and salinity fields will adjust by advection to remove the error. Other people seem to take a point of view somewhere in between and different schemes have been proposed in order to minimise the error.

Apparently, it is still relevant to study the topic, owing to this lack of consensus, and also to perform a fair comparison of the different methods. This has been done using the Princeton Ocean Model (POM) and is described by Kliem and Pietrzak (1999) (henceforth KP99). In KP99 the second-order sigma method originally used in the model is compared with a fourth-order sigma method inspired by McCalpin (1994), second- and fourth-order versions of a $z$-level-based correction by Beckmann and Haidvogel (1993), a $z$-coordinate method by Stelling and van Kester (1994), the modification of this by Slørdal (1997) and a true and quite straightforward $z$-level-based method. It is noted that by the term "sigma method" is simply meant a method using $\sigma$-coordinates.

This chapter relies heavily on the work presented in KP99. The simple tests performed in KP99 are discussed only very briefly, with emphasis on the comparison with a laboratory model of the circulation in the Skagerrak. Four simulations are presented and compared with the laboratory model. The simulations are performed with the original second-order sigma and the $z$-level-based methods with resolutions of 1852 m and 3704 m (1 and 2 nautical miles, respectively).

The four simulations are all performed with POM (see Blumberg and Mellor (1987) for details on the model). It is non-linear, 3-dimensional and hydrostatic, and includes a free surface and the level 2.5 turbulence closure scheme by Mellor and Yamada (1982).

POM has been applied to the Skagerrak before (Svendsen et al., 1996) with satisfactory results for the general circulation. Also in KP99 the circulation is simulated well with all methods. However differences between the various methods are demonstrated in the vertical structure of the velocity field. The best result in the comparison with the laboratory model is found with the simple $z$-level-based method, while a flow reversal at the steep northern slope of the Norwegian

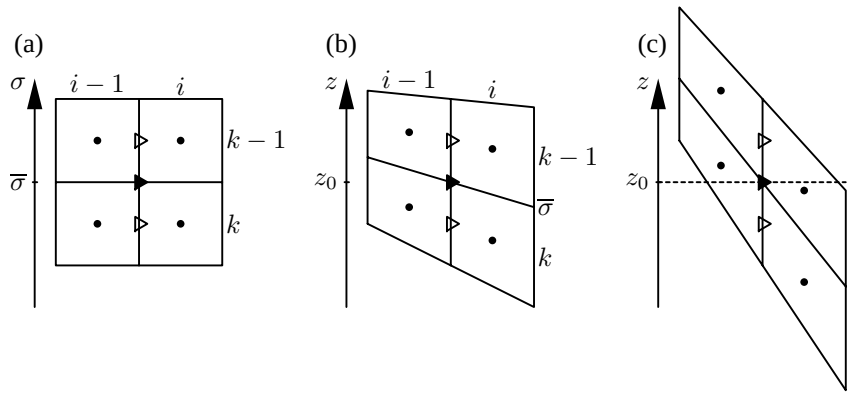


Figure 2.1: Vertical grid and notation employed. The buoyancy points (solid circles) are located at the cell centres $(i, k)$, the velocity points (open triangles) at the cell interfaces $(i - 1/2, k)$, and the density gradients (solid triangles) are calculated in between $(i - 1/2, k - 1/2)$. (a) Sigma coordinate $C$ grid. (b) Hydrostatically-consistent grid. (c) Hydrostatically-inconsistent grid.

trench is found with the original second-order sigma method.

The theoretical error evaluation suggests that decreasing the horizontal grid size reduces the error. Therefore the 3704 m simulations from KP99 are compared with simulations performed with a resolution of 1852 m. Three of the simulations are presented elsewhere. The 3704 m simulations are taken from KP99, the 1852 m simulation with the $z$-level-based method are presented by McClimans et al. (2000) and to complete the comparison, the second-order sigma method is used in a 1852 m simulation not presented elsewhere.

## 2.2 Pressure gradient error

### 2.2.1 Sigma coordinate model

Sigma coordinates are terrain following, meaning that the surface and the bottom define constant levels. In POM the surface is at $\sigma = 0$ and the bottom at $\sigma = -1$. For simplicity the rigid lid approximation will be made setting the surface elevation to zero, and the analysis here is made for two dimensions only. The extension to three dimensions and inclusion of a free surface is straitforward. The horizontal coordinates in the Cartesian coordinate system is denoted with a star and $(x, \sigma)$ corresponds to $(x^*, z)$. With $H$ denoting the depth the relation between the coordinate systems is

$$x = x^* \qquad \sigma = \frac{z}{H} \tag{2.1}$$

In the model, the order of calculation is such that the density gradient is calculated, and is then integrated to give the baroclinic pressure gradient. The density is represented by the buoyancy, $b = g\rho/\rho_0$, where $g$ is the gravity acceleration and $\rho_0$ is a reference density. It is in the calculation of the horizontal density gradient that the error arises. Therefore, mainly the density gradient is discussed in the following. When the density gradient is integrated, the error is integrated as well giving an error on the part of the pressure gradient term in the momentum equation.

Using the chain rule the horizontal density gradient is calculated as

$$\frac{\partial b}{\partial x^*} = \frac{\partial b}{\partial x} - \frac{\sigma}{H}\frac{\partial H}{\partial x}\frac{\partial b}{\partial \sigma} \tag{2.2}$$

This equation simply states that the horizontal gradient (left-hand side) equals the gradient along a surface of constant $\sigma$ (first term on the right-hand side) corrected for the vertical gradient (second term on the right-hand side). The equation is mathematically correct, the problem arise in the numerical discretization. In POM this is done with second-order central differences. The computational grid is illustrated in figure 2.1a. The density gradient is calculated at the position $(i-1/2, k-1/2)$ using the four surrounding density points

$$\frac{\partial b}{\partial x^*} = \frac{b_{i,k} + b_{i,k-1} - b_{i-1,k} - b_{i-1,k-1}}{2\Delta x} - \frac{\overline{\sigma}}{\overline{H}}\frac{\Delta H}{\Delta x}\frac{b_{i,k-1} + b_{i-1,k-1} - b_{i,k} - b_{i-1,k}}{2\Delta \sigma} \tag{2.3}$$

where $\Delta x = x_i - x_{i-1}$, $\Delta\sigma = \sigma_{k-1} - \sigma_k$, $\Delta H = H_i - H_{i-1}$, $\overline{\sigma} = (\sigma_{k-1} + \sigma_k)/2$ and $\overline{H} = (H_i + H_{i-1})/2$.

The order of accuracy is found by performing a Taylor expansion of the density and inserting this into the algorithm. For simplicity a horizontally homogeneous stratification is assumed. This is a common assumption (e.g. Mellor et al., 1994). Then the error is found to be

$$E\left(\frac{\partial b}{\partial x^*}\right) = \frac{\overline{H}}{4}\frac{\partial H}{\partial x}\left|(\Delta\sigma)^2 - \left(\Delta x\frac{\overline{\sigma}}{\overline{H}}\frac{\partial H}{\partial x}\right)^2\right| \cdot \left[\left(\frac{\partial^2 b}{\partial z^2}\right) + \frac{\overline{\sigma}\overline{H}}{3}\left(\frac{\partial^3 b}{\partial z^3}\right) + \ldots\right] \tag{2.4}$$

From the last pair of brackets it is seen that the error is zero for a linear density profile, and the method is therefore said to of be second order.

One of the disagreements found in the literature is whether the sigma method is convergent or not. Haney (1991) and Stelling and van Kester (1994) claim that the method is nonconvergent, if the hydrostatic consistency condition (eq. 2.5) is violated. This is denied by Mellor et al. (1994) and Fortunato and Baptista (1996). To judge this eq. 2.4 is slightly rewritten compared with the expression in KP99, using that $\Delta H = \Delta x(\partial H/\partial x)$. In this way $\Delta x$ is included in the equation. It is then seen that the method is convergent, as $E \to 0$ for $\Delta\sigma \to 0$ and $\Delta x \to 0$. On the other hand, it is also seen that just increasing the vertical resolution will not necessarily decrease the error, owing to the second term in the first pair of brackets. This is the reason for introducing the hydrostatic consistency condition

$$\left|\frac{\sigma}{H}\frac{\partial H}{\partial x}\right|\frac{\Delta x}{\Delta \sigma} < 1 \tag{2.5}$$

This assures that the content of the first pair of brackets is positive. When this condition is violated the error is mainly due to a large $\Delta x$ and will not decrease for a refinement in the vertical. When $\Delta x$ is decreased, the error also decreases, until the hydrostatic consistency conditions is satisfied. Then the main part of the error lies in the vertical discretization, and the error actually increases as $\Delta x$ is reduced further.

The consequence of the hydrostatic consistency condition is seen in figure 2.1b and c, with the grid sketched in Cartesian coordinates. If the hydrostatic consistency condition is satisfied, the depth of the density gradient (denoted $z_0$) is located in between the density points, and the vertical differentiation in eq. 2.2 is performed as an interpolation. If the hydrostatic consistency condition is violated the two points in one water column is above $z_0$ while the two points in the other column is below $z_0$, and the vertical differentiation is now an extrapolation.

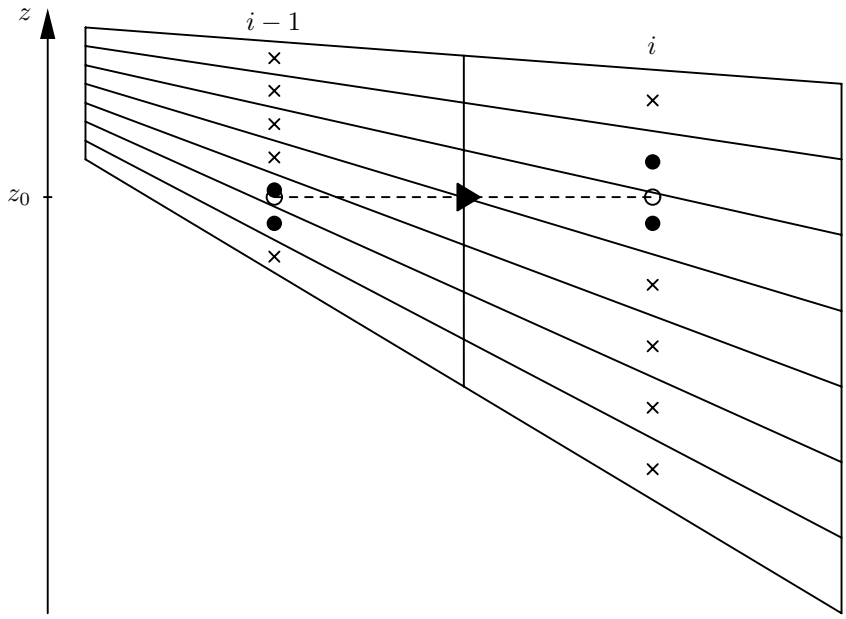


Figure 2.2: Grid used for the $z$-level interpolation. Open circles indicate interpolated density values for the $z$-level method. Solid circles are the buoyancy points used to calculate the horizontal gradients and crosses are the locations of the buoyancy points on the sigma grid.

In $\sigma$-coordinates the grid is always nicely structured (figure 2.1a) with the position for the density gradient in between the four density points used to calculate the gradient and is independent of the hydrostatic consistency condition. This is the reason why the method converges as $\Delta x$ and $\Delta\sigma$ goes to zero.

Usually extrapolation is undesirable, the reasoning being that ideally the grid should be hydrostatically-consistent. However, this condition is severe with respect to the horizontal resolution in the presence of steep slopes. Satisfying it will in some cases lead to such a fine resolution that the computational burden becomes overwhelming. The interesting questions are thus: how serious is the error when the condition is violated? Is it possible to define a limit of how far the condition can be violated while still giving satisfactory results, and do other methods give smaller error?

In KP99 a number of different methods are tested. Here only the simple $z$-level-based method is compared with the second-order sigma method originally used in the model. The $z$-level-based method is sketched in figure 2.2. Instead of using the densities at the corresponding levels $k-1$ and $k$ as in the second-order sigma method, a search is made down through the water column to find the two densities around the depth $z_0$. These are then interpolated to $z_0$, and the horizontal density gradient is calculated as

$$\frac{\partial b}{\partial x^*} = \frac{b_i(z_0) - b_{i-1}(z_0)}{\Delta x} \tag{2.6}$$

This procedure is repeated for all the density gradient points in the grid. If the hydrostatic consistency condition is violated, the $z$-level-based method is expected to be superior, since it assures interpolation. On the other hand if the condition is satisfied, the $z$-level-based and the second-order sigma method use the same four density points in the calculation, and the two methods are expected to be of the same accuracy.

A problem with the $z$-level based method arises, if $z_0$ is actually in the bed at one of the two columns. The density gradient is then assumed to be zero, as also by Stelling and van Kester (1994) and Slørdal (1997).

It should be noted that the error evaluation above is based on the assumption of zero horizontal gradients. Then it is expected that the $z$-level-based method perform better, since it always interpolates. Fortunato and Baptista (1996) made an error evaluation with the isopycnals parallel to the bed and found the lowest error with the sigma method in this case. This can be explained by the fact that then the vertical derivative at the grid position $(i-1/2, k-1/2)$ is actually well represented by the density points at $k-1$ and $k$. In other words, if the isopycnals are parallel to the $\sigma$-levels, the sigma method interpolates even for large $\Delta x$. This suggests that a discussion of interpolation versus extrapolation should be performed neither in $z$- nor $\sigma$-coordinates but in isopycnal coordinates, with the density as the vertical coordinate. In the error evaluation above, isopycnal and $z$-coordinates equal each other, owing to the assumption of horizontal stratification.

### 2.2.2 Testing the methods

Usually the various methods are tested through simple tests. The model is set up for an idealised case, often in 2 dimensions, i.e. in a section, with a specified density field and a known analytical solution. The tests are performed as follows: A bathymetry and a density field are specified. They must be simple such that the corresponding pressure gradient can be calculated analytically. Often the pressure gradient is expressed as a geostrophic velocity, since this gives a better idea of the effect of the error. For the given density field the model calculates the pressure gradient, which is then compared with the analytical solution. The model performs only one step. This gives a very quick execution, with the possibility of testing the various methods for different bathymetries and density fields, and of performing sensitivity tests, for example of the grid size.

In KP99 two simple tests, of Slørdal (1997) and Haidvogel and Beckmann (1999) respectively, are performed. The main conclusion of the tests is that the $z$-level-based method performs best, with lower errors than the sigma methods. The set-up and results are described in detail in KP99 and will not be discussed further here. However, a few comments on the simple tests in general are given.

The advantages of the simple tests, with the quick execution and possibility of performing different tests and sensitivity analysis, make them attractive for the evaluation of the various methods. There are weaknesses, however, that should be taken into account, when the results are interpreted.

First of all, the error depends upon the given set-up, and some methods might be favoured by the set-up. For example, if the density profile is a second- or third-order polynomial, fourth-order methods have advantages over second-order methods. Likewise, based on the findings of Fortunato and Baptista (1996), it might be reasonable to expect that $z$-level-based methods are favoured by a horizontally homogeneous stratification, while the sigma methods are favoured if the isopycnals are parallel to sigma surfaces.

In the Slørdal (1997) test (test 1 in KP99) the largest errors using the sigma methods are found where the pycnocline intersects the bed (see figures 2(top) and 4 in KP99). If this coincides with the position of density gradients the error will be large. If the grid is moved to one side or the other the error decreases. Thus, the error depends on the actual position of the grid points, and moving the grid horizontally will change the value of the error.

Sometimes it is convenient to express the error as a relative error. However, it is quite often seen that the tests are performed with horizontal homogeneous stratification. This density field is convenient, since the two terms on the right hand side of eq. 2.2 cancel each other and the analytic

solution is a zero pressure gradient. Therefore, if the model gives something different from zero, this equals the error. In this case, the evaluation should not be on relative error, for the obvious reason that even a small error will show up as a huge (infinite) relative error, when the reference solution is very small (zero).

Keeping in mind the above mentioned weaknesses the simple tests are a powerful tool in the evaluation of the various methods. However, the direct error of the pressure gradient corresponding to the idealised set-up is calculated. But actually, it is the model result for the elevation and velocity that is of interest. The complexity of a full three dimensional model gives the possibility of feedback mechanisms and cancellation of the error. Thus, realistic simulations with the model are needed in addition to the simple tests. Unfortunately, it is necessary to know the solution in order to perform a fair evaluation of the different methods. This problem is overcome here through comparison with a laboratory experiment.

## 2.3 Simulations of Skagerrak

### 2.3.1 Set-up

As a step towards a more realistic simulation, the model is set up for the Skagerrak and the results are compared with a simulation performed with a laboratory model. The set-up is configured as close to the laboratory experiment as possible. The simulations are thus performed on the real bathymetry, but with simple initial fields and controlled forcing.

The laboratory tank diameter is 5 m, the maximum depth is about 0.5 m, and length and time scales are given according to a consistent set of scaling laws (McClimans, 1990). The laboratory model is described in detail by McClimans et al. (1996) and McClimans et al. (2000).

Two different sets of scales are possible for the numerical simulations. The model can be set up either to simulate the exact laboratory experiment (same length and time scales as in the laboratory) or it can be set up with the scales of the Skagerrak. The latter is chosen here, since the aim is to investigate the model's ability to simulate the circulation in the Skagerrak using the real scales. It is noted that, in this case, the reference solution is actually also just a model result. Exact agreement is therefore not expected, but the laboratory result is used more as a guide in the comparison of the different numerical methods.

The bathymetry is shown in figure 2.3. The model domain covers the Kattegat, the Skagerrak and a part of the North Sea in a circular region with a diameter of about 625 km. The boundary through the North Sea (to the west and south-west of the model domain) is a closed wall determined by the laboratory tank. In KP99 two sections (A and C) are used in the comparison, here the results from section B are also shown.

| Source | Inflow ($10^6 m^3/s$) | Salinity (psu) | Position (km,km) |
|---|---|---|---|
| Atlantic ocean | 1.0 | 35.2 | (59-70,483) |
| Central North Sea | 0.7 | 34.9 | (16,226-314) |
| German Bight | 0.05 | 31.0 | (204-328,65) |
| The Belts | 0.07 | 20.0 | (483-515,168) |
| The Sound | 0.03 | 20.0 | (585-594,185) |

Table 2.1: Inflow sources. The positions correspond to the full domain (e.g. figure 2.3).

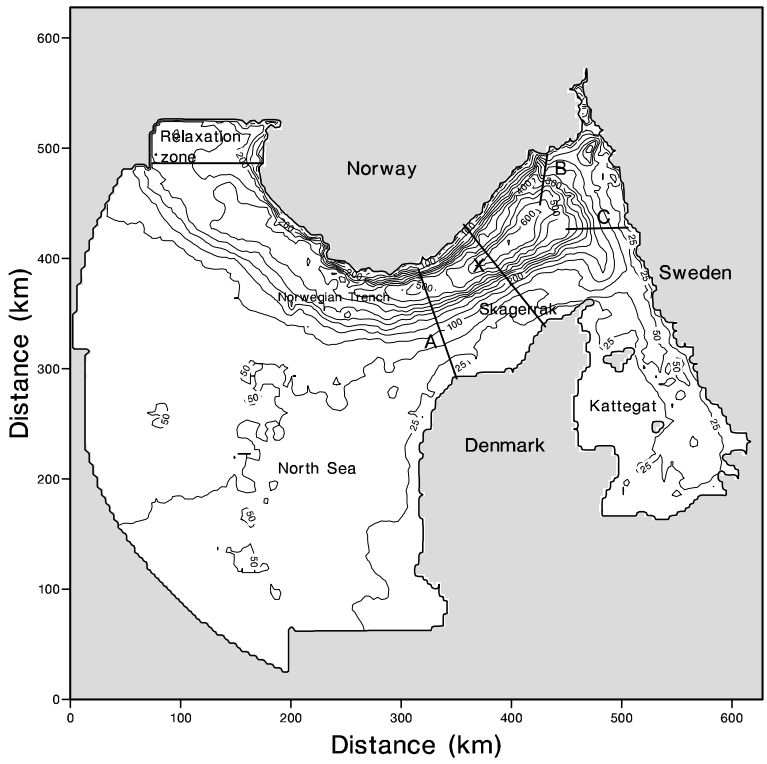


Figure 2.3: Bathymetry of the Skagerrak model. The three sections, A, B and C, used to compare the numerical results with the laboratory experiment are shown. Section X is an extra section used for the intercomparison of the various numerical simulations.

The model is initialised with homogeneous water at a salinity of 35.2 psu, a temperature of 18°C and zero velocity. It is forced by five inflow sources (see table 2.1). The temperature is kept uniform throughout the simulations and the baroclinic forcing arises from the salinity differences.

In the laboratory model the outflow takes place at an overflow weir. In the numerical simulations a flow relaxation scheme is applied, relaxing the interior solution toward zero elevation and velocity and a salinity of 35.2 psu (Atlantic water at rest) over a 10 grid point wide zone.

The simulations are performed for two different resolutions; a grid of $340\times340$ points with a grid size of 1852 m and a grid of $170\times170$ points with a grid size of 3704 m. Sixteen levels are used in the vertical with a fine resolution close to the surface and bed, in order to resolve the surface and bottom boundary layers.

The measurements in the laboratory experiment were performed after the model had reached steady state. In KP99 it is found that 100 days are suitable for the numerical simulations to reach the steady state. Thus the simulations are performed for a 100-day period and all results shown in the following section are extracted at the end of this period[1].

The hydrostatic consistency fraction (left-hand side of eq. 2.5) is shown in figure 2.4. For the 3704 m resolution the hydrostatic consistency condition is violated in large areas, and close to the

[1]The results shown by McClimans et al. (2000) are after 90 days. In order to make a fair comparison of the simulations shown in KP99 with the 1852 m simulation with the $z$-levels-based method performed by McClimans et al. (2000), the latter is extended for another 10 days for this study.

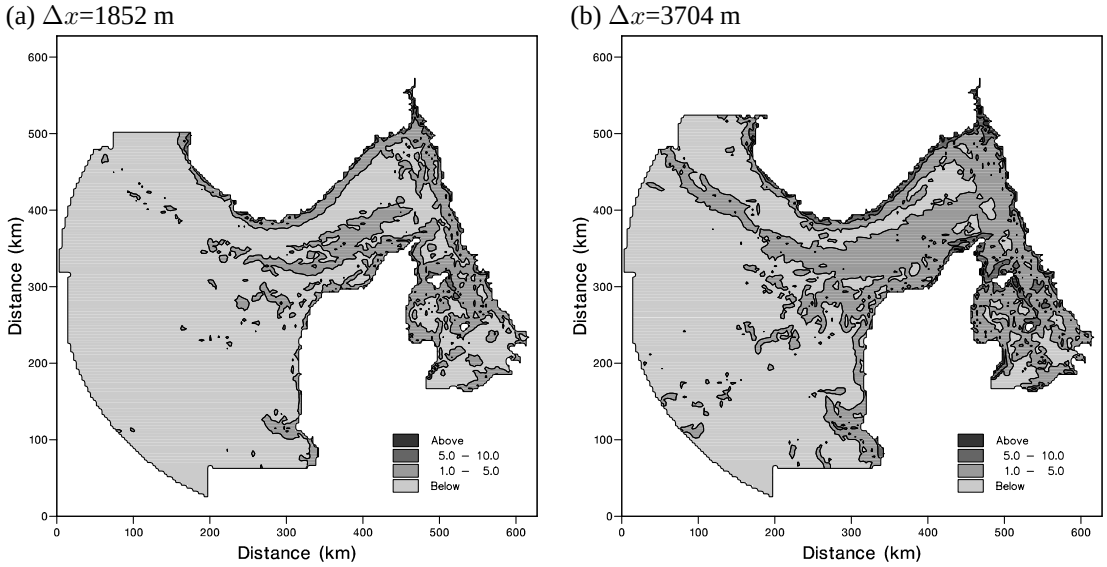


Figure 2.4: Hydrostatic consistency fraction (left-hand side of equation 2.5) for the numerical simulations using 16 vertical sigma levels. (a) Horizontal grid spacing of 1852 m (1 n.m.). (b) Horizontal grid spacing of 3704 m (2 n.m.) (from KP99 figure 10).

Norwegian coast values of up to 20 are found. As $\Delta x$ is halved, the hydrostatic consistency fraction is also halved, and in parts of the Skagerrak the hydrostatic consistency condition is satisfied with the 1852 m resolution while violated with the 3704 m. Close to the coast, though, the value is high in both cases. Also, in the Kattegat and on the Danish side of the Norwegian trench the condition is violated for both resolutions owing to the small depths.

### 2.3.2 Results

The results of the simulations are shown in figures 2.5-2.8. The results of the 3704 m simulations are also shown in KP99 and are here plotted together with the 1852 m simulations to facilitate the comparison on different resolutions. As mentioned above (section 2.2.1), it is to be expected that the results with the sigma and the $z$-level-based methods converge as the resolution is increased. This is seen in all the figures. While the two 3704 m simulations show distinct differences as discussed in KP99, the two 1852 m simulations are much more similar.

Figure 2.5 shows the surface elevation field after 100 days. A strong cyclonic circulation is seen in all simulations. The gradient of the surface elevation is slightly sharper in the 1852 m than in the 3704 m simulations, probably owing to the higher resolution. This is especially distinct in the northernmost corner of the Skagerrak. Here the isolines for elevation closely follow the Swedish coast until the Norwegian coast is reached. They then turn southwest following the Norwegian coast. In the 1852 m simulations the isolines make an almost 90° turn, while with the coarser resolution the turn is more smooth. The same features is seen in the surface salinity (not shown).

Figure 2.6 shows the alongshore component of the current at the surface and at 50 m depth at sections A, B and C. The results of the four numerical simulations agree with each other and conform to the laboratory model at section C and to some extent also at section B. It is uncertain

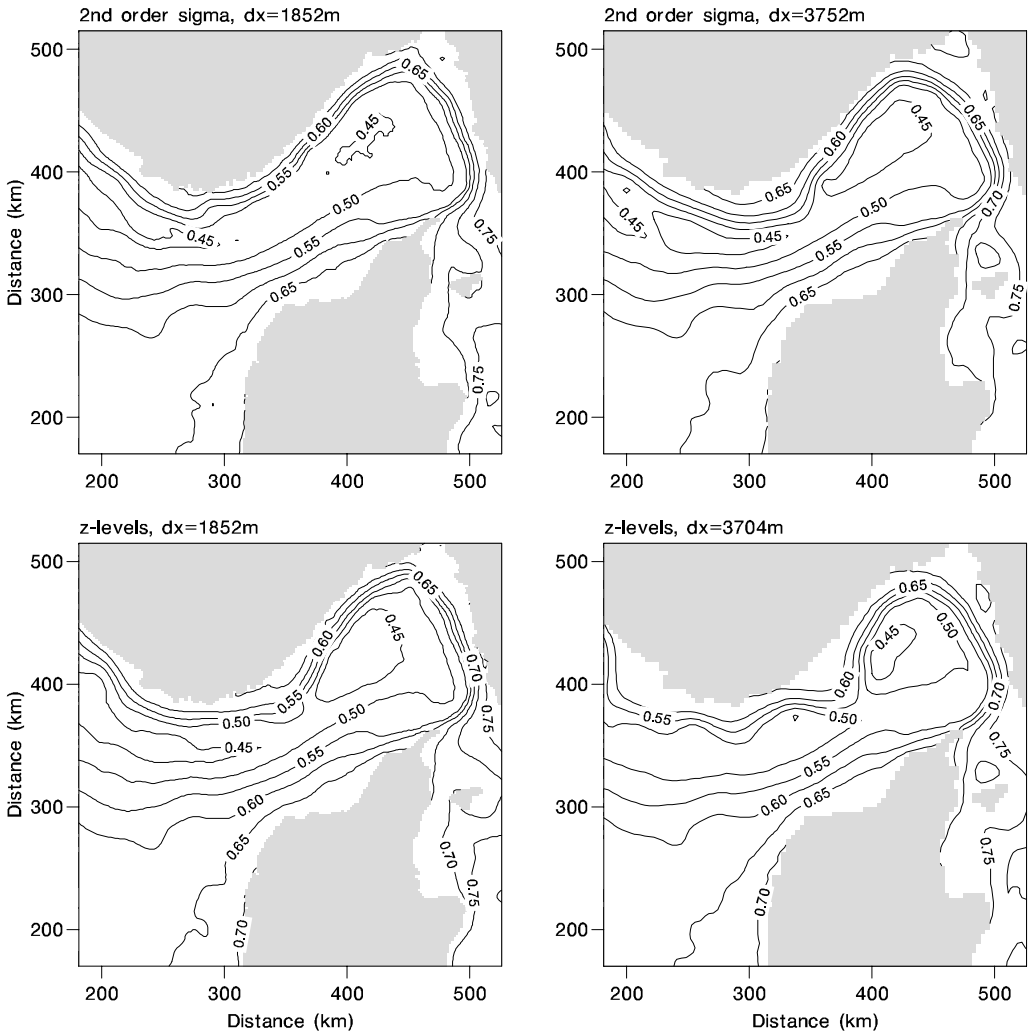


Figure 2.5: Surface elevation (meters). The coordinates correspond to the full domain (e.g. figure 2.3).

why the velocity at section C is so much higher in the numerical simulation than in the laboratory model, while the current speed agrees much better at sections A and B.

At section C the results agree with the laboratory model both with respect to the position and the width of the coastal current. The velocities at 50 m depth are almost identical in the four numerical simulations. At the surface the coastal current is slightly broader with the coarse than with the fine resolution, and the peak velocity is correspondingly smaller, in agreement with the findings of the elevation gradient mentioned above. Furthermore, it is seen that the $z$-level-based method gives a slightly narrower current than the sigma method.

At section B the surface current maximum is found to be further offshore than expected from the laboratory model. The best result with respect to the distance from the Norwegian coast to the peak velocity is found with the finer resolution with a slightly better performance of the $z$-level-based method than the sigma method. On the other hand the sigma method seems to perform better at coarse resolution. This is contrary to the expectations from the theoretical error evalua-

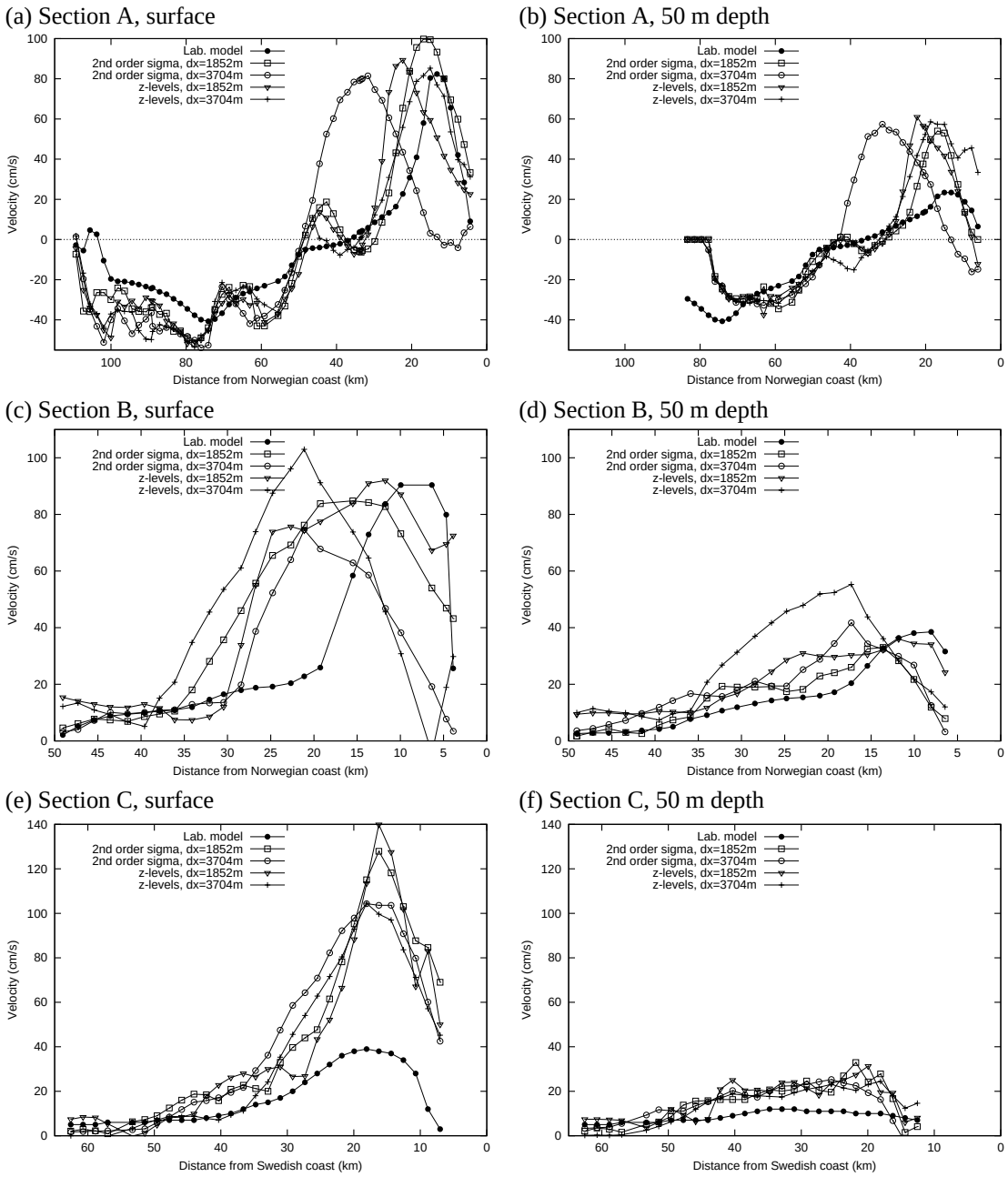


Figure 2.6: Alongshore component of the velocity at the surface and at 50 m depth at sections A, B and C. (a,b) Section A. A positive current indicates a westward flow. (c,d) Section B. A positive current indicates a south-westward flow. (e,f) Section C. A positive current indicates a northward flow.

tion (section 2.2.1), where it was suggested that the $z$-level-based method should have the lowest error at coarse resolution (hydrostatically-inconsistent grid), but the two methods should perform equally well at fine resolution (hydrostatically-consistent grid). This contradiction is not directly explainable and shows some of the problems with the complexity of the realistic simulations.

The most pronounced differences in the comparison of the simulations are found at section A. This is to be expected since section A goes right across the Norwegian trench with its steep slopes. At figure 2.6 it is seen that all four numerical simulations agree with the laboratory model to within 20 cm/s with respect to the peak value of the surface velocity. However, at 50 m depth the simulated velocities are much higher than in the laboratory model. The reason why the velocities in the simulations decrease less with depth than in the laboratory model is probably that there is too much vertical mixing in the numerical model.

The 3704 m simulation with the $z$-level-based method apparently performs best. The width and position of the coastal current correspond closely to the laboratory model and the peak value is the same within a few cm/s. The worst result is found with the coarse resolution sigma method, where the current is moved too far away from the Norwegian coast. In between, the two 1852 m simulations are found. They both agree reasonably well with the laboratory model with the sigma method giving a slightly better result, i.e. the current is closer to the coast in agreement with the laboratory model.

In KP99 it is found that the differences between the various methods become more apparent in the cross sections of salinity and velocity. In figure 2.7 the cross section of the velocity at section A is shown. The curves of figure 2.6a,b are actually the same as shown in figure 2.7 for the surface and 50 m depth. However, the velocities shown in figure 2.6 are "measured" in the numerical simulations exactly at the same positions as in the laboratory model. Therefore, both figures contain useful information. Figure 2.6 gives the exact comparison of the simulations with the laboratory model and with each other, while figure 2.7 gives a better overview of the variation of the velocities with depth.

In figure 2.7 the similarity of the two methods in the 1852 m simulations is clear, with only small differences in the magnitudes of the velocities and the position of the core of the Norwegian coastal current. More pronounced differences are found with the coarser resolution, with the $z$-level-based method in better agreement with the laboratory model. With the sigma method there is a flow reversal at the steep slope of the Norwegian trench and the coastal current is moved away from the coast to the deep part of the Skagerrak. With the $z$-level-based method the result compares much better with the laboratory model, with the Norwegian coastal current close to the coast and no flow reversal.

The result with the sigma method is improved by decreasing the grid size from 3704 m to 1852 m; the area of the cross section covered by the flow reversal is decreased and the Norwegian coastal current is considerably closer to the coast. Surprisingly, the $z$-level-based method does not gain by increased resolution; rather, the result seems to be worse with the smaller grid size. While there is no flow reversal with the larger grid size, this is clearly seen with the fine resolution.

It is not clear why the $z$-level-based method apparently performs better with the coarser resolution. It may be that it just looks so by chance. On figure 2.5 it is seen that the elevation isolines meander in the 3704 m simulation using the $z$-level-based method rather than being parallel to the Norwegian coast and exactly at section A the isolines are closest to the coast. Since the elevation field to some extent is a picture of the surface currents, the coastal current meanders too and is closest to the coast exactly at section A. It should be noted that the positions of the sections are decided in the laboratory experiment, i.e. before the numerical simulations were performed. In the other simulations the elevation isolines are much more parallel to the coast and the bathymetry.

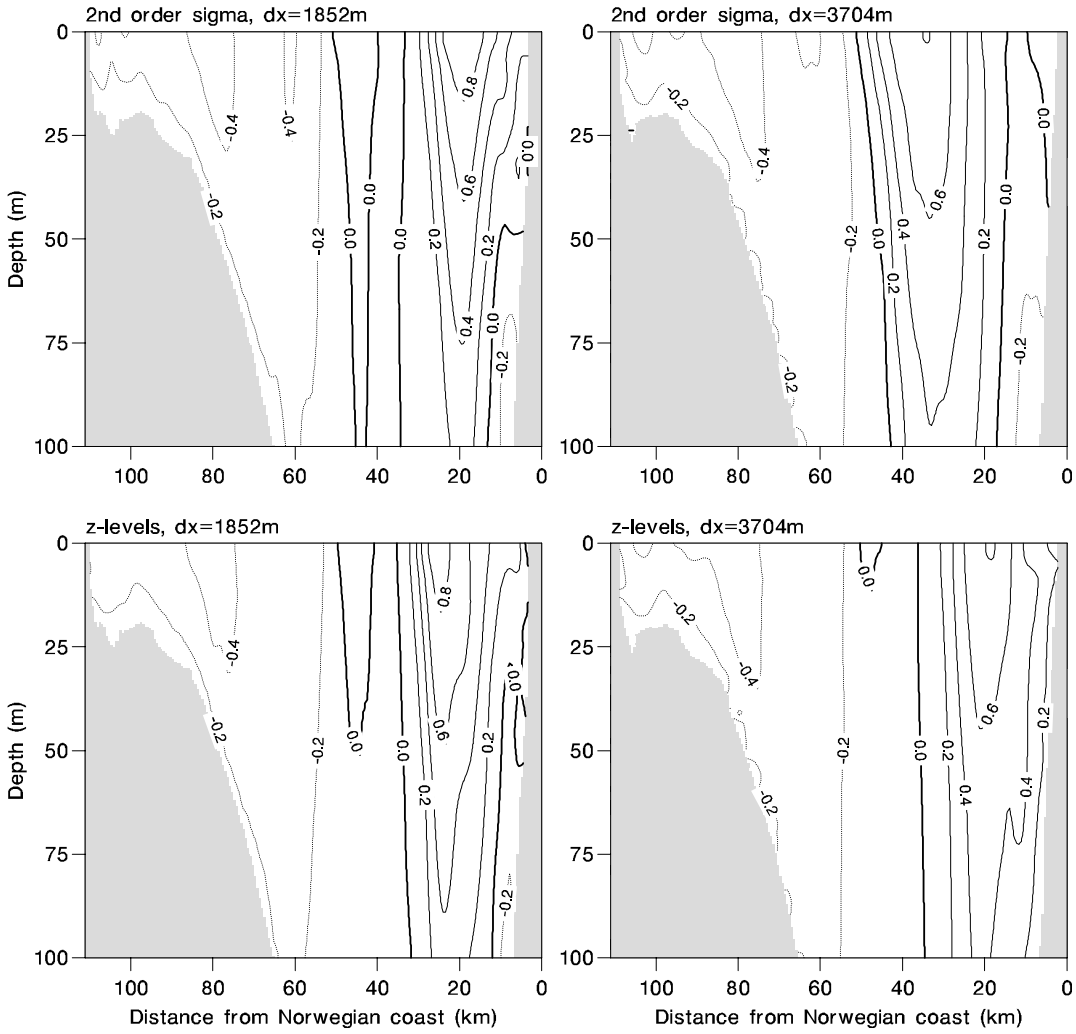


Figure 2.7: Cross section of velocity (m/s) at section A.

This is to be expected due to topographical steering.

An extra cross section (section X on figure 2.3) is shown in figure 2.8 to support the argument that the coarse resolution $z$-level-based method has the best performance only by chance. The extra section is positioned where the surface current in this simulation is far off-shore. This simulation also shows a flow reversal and does not seem to perform better than the 1852 m simulations.

The results of sections A and X show the difficulties encountered in comparing the various methods in a full and realistic simulation. This has to do with the complexity of the model with possible feedback mechanisms and a large number of variables and positions available for use in the comparison. At one position one simulation seems to be the best, while at other position another simulation might be better.

The overall impression of the figures is that the results are better at the finer resolution with a grid size of 1852 m. At this resolution the sigma and the $z$-level-based methods seem to perform similarly. However, this resolution involves a large number of grid points ($340 \times 340$ in the horizontal). And even with this resolution the hydrostatic consistency condition is not satisfied

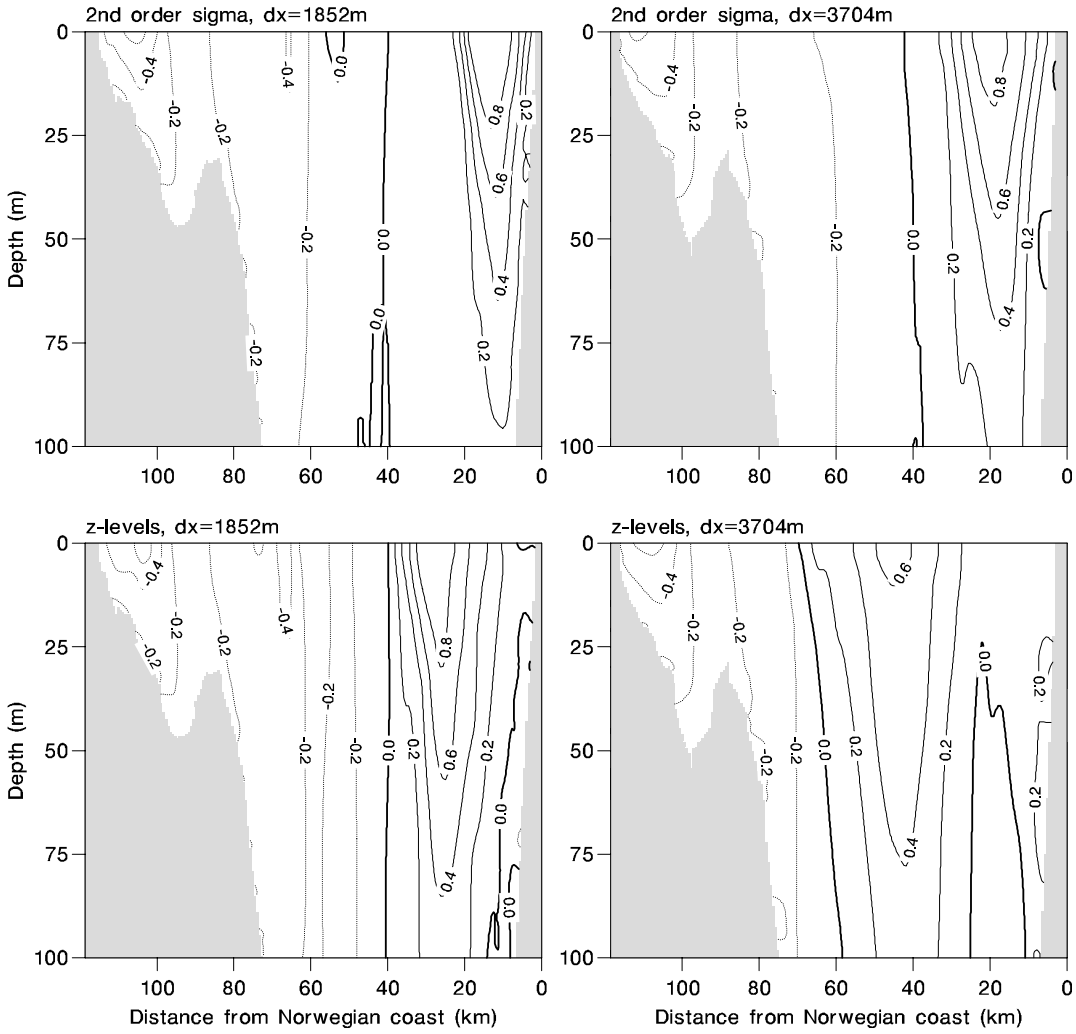


Figure 2.8: Cross section of velocity (m/s) at section X.

everywhere (figure 2.4) and there is an artificial flow reversal of 20-30 cm/s (figure 2.7). It took about 10 days of real time to perform one 100 days simulation on the supercomputer (NEC SX-4) at the Danish Meteorological Institute. If one wishes to extend the area and at the same time cover the Skagerrak with a satisfactory resolution, the computations might easily become overwhelming. Therefore, the simulations at the coarser resolutions are indeed interesting. A grid size of 3704 m is still a low value if a larger domain is simulated. At this resolution the sigma method as originally used in the model apparently gives good quality results with respect to the circulation and the elevation, but artificial currents are found at the slopes of the Norwegian trench. These flows are reduced using the $z$-level-based method but they are not removed totally as illustrated by section X (figure 2.8).

The $z$-level-based method has a problem when the interpolation goes into the bottom. In this case the simple assumption of no gradient has been made. The $z$-level-based method would probably perform better with more sophisticated assumptions near the bottom. This has not been studied here, but might be a relevant topic for future work.

# Chapter 3

# The area around Cape Farewell

## 3.1 Background description

The circulation in the area around Cape Farewell is strongly influenced by the continental slope close to the coast giving a strong topographical steering. The shelf is narrow - less than 100 km, with depths up to 500 m. The deep ocean, with depths exceeding 3000 m, is found less than 200 km off the coast.

Three types of water masses are found in the area. At the surface on the shelf and partly on the continental slope Arctic water is found. It is cold and relatively fresh, with temperature less than $-1.5°$C and salinity less than 33.3 psu (Krauss, 1995). On the outside of the Arctic water and partly mixed with it, is the Irminger water of about 4°-5°C and 34.9-35.0 psu. Below these water masses and further off the coast is the warm and saline Atlantic water of about 7°C and 35.05 psu.

The ocean dynamics of the region are influenced by the current pattern in the northern North Atlantic. Here is given a brief description only, see Dietrich et al. (1980) for a general description of the North Atlantic circulation, Schmitz and McCartney (1993) for a more recent review, and Mortensen (1997) for a detailed description of the water masses.

The North Atlantic Current brings the relatively warm and saline water northward. Between Iceland and the Faeroe Islands it bifurcates with one branch going northeast into the Norwegian Sea, and another branch trapped by the western slope of the Mid Atlantic Ridge, turning west to form the Irminger Current. This divides further, with one branch going through the east side of the Denmark Strait up north of Iceland. The other branch merges with the East Greenland Current flowing southward along the east coast of Greenland to the Cape Farewell area. The East Greenland Current initiates with the outlet through Fram Strait. It follows the continental slope along the east coast of Greenland transporting the relatively cold and fresh Arctic water southward passing Cape Farewell.

Buoy drift studies have given an essential contribution to the picture of the circulation in the area. Krauss (1995) deployed 18 buoys at a section between the Faeroe Islands and Greenland at 62°N to study the branching of the Irminger Current. The buoys deployed on the western side of the Reykjanes Ridge (west of 28°W) joins the East Greenland Current. The largest current speed of 0.7 m/s was found at the continental slope. Uotila et al. (1997) deployed two buoys in the Denmark Strait. Both buoys followed the East Greenland Current to Cape Farewell. Uotila et al. (1997) observed current velocities up to 0.5 m/s with stable directions.

Ice is formed in the Arctic Ocean by freezing. It becomes 2-4 m thick and up to 3 years old before it drifts out of the Arctic Ocean (McLaren et al., 1994; Thomas et al., 1996; Harder, 1997).

The Arctic Ocean is enclosed by land except for a few straits. The Fram Strait between Greenland and Spitsbergen is one of the main outlets of ice. The annual ice transport through Fram Strait shows significant variations from year to year with values of 2000-4000 $km^3$/year (Harder et al., 1998; Vinje et al., 1998). In Fram Strait the ice floes are up to 50 km in diameter. The ice is transported with the East Greenland Current, breaking up on the way, and at Cape Farewell the floe size is typically less than 100 m (Gill and Valeur, 1996). Along the way new ice is formed by freezing. This is usually called first year ice, in contrast to the multi-year ice originating from the Arctic.

## 3.2 Numerical simulations

The numerical simulations of the ocean and sea ice conditions in the area are performed for a 10-day period. All simulations are made on the same set-up, i.e. on the same mesh and for the

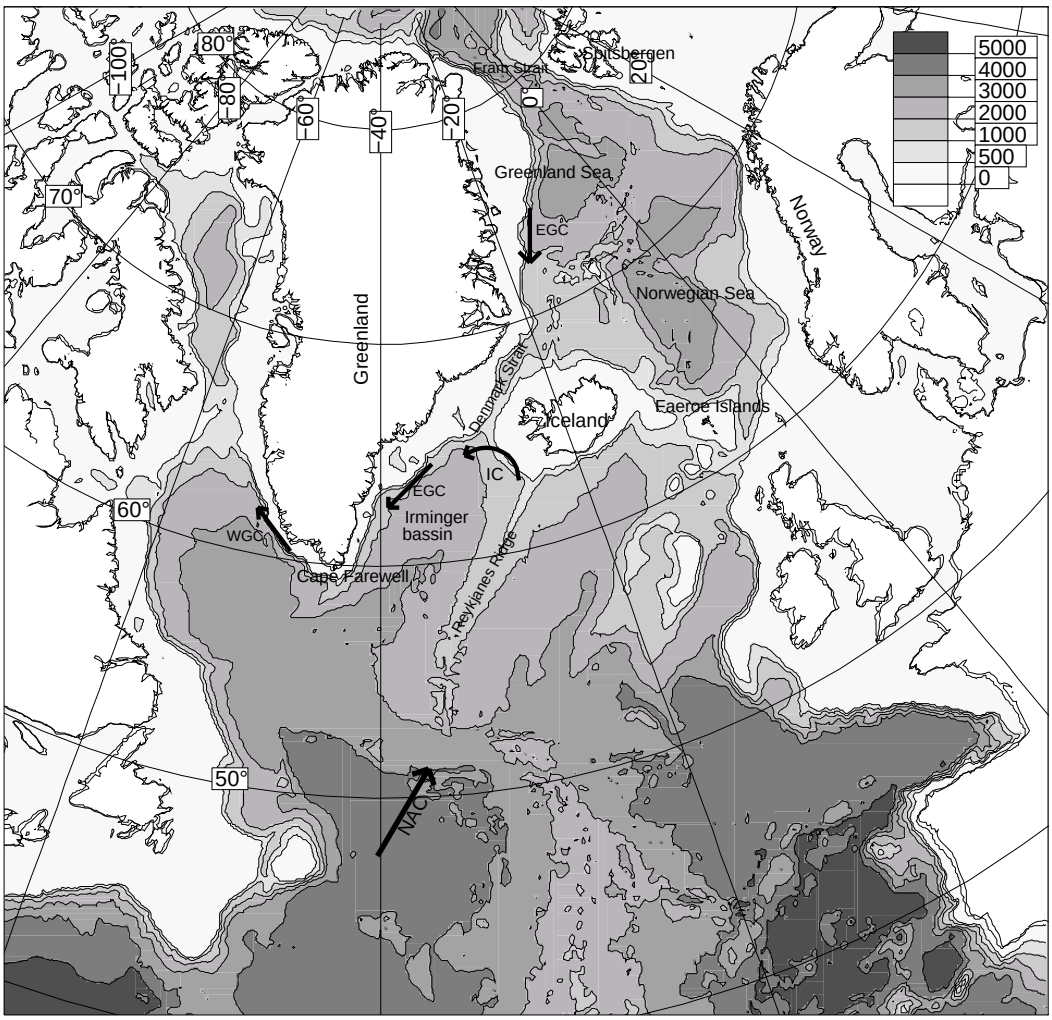


Figure 3.1: Bathymetry and surface currents of the North Atlantic. NAC: North Atlantic Current, IC: Irminger Current, EGC: East Greenland Current, WGC: West Greenland Current.

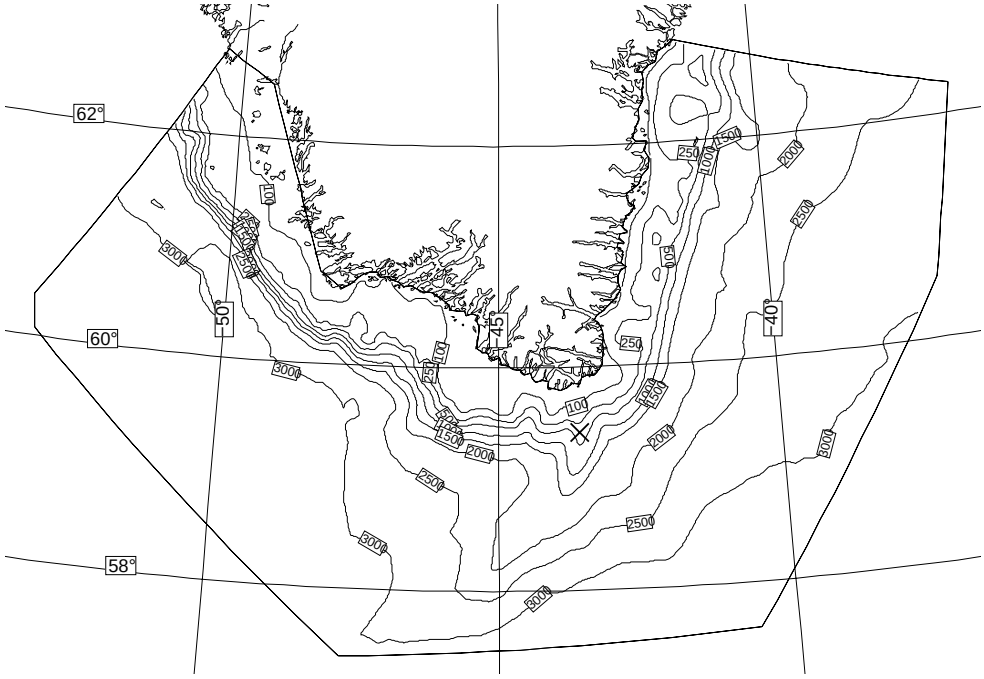


Figure 3.2: Bathymetry of the model domain. The position (about 50 km south of Cape Farewell) used for comparison of velocity (table 4.1 and figure 4.6) is indicated with a cross.

same period, to facilitate model comparison. The period March 17-27 1997 is simulated due to the good coverage of sea ice observations used for validation of the sea ice model.

The bathymetry of the model domain is shown in figure 3.2. The domain covers the area around Cape Farewell with open boundaries normal to the isobaths about 300 km up the east and west coasts, respectively, and an open boundary on deep water almost parallel to the coast and isobaths about 250 km offshore. The inflow of water and sea ice takes place at the boundary normal to the east coast, and outflow will primarily be at the boundary normal to the west coast, while the currents at the boundary on the deep water will be very small.

The computational mesh is shown in figure 3.3. It consists of 3420 nodes connected by 6611 elements. The generation of the mesh exploits the possibility with the finite element method to have a varying resolution, thus having high resolution in areas of interest and where necessary for good model results, and coarse resolution on the deep parts to place the boundaries well away from the coast without unnecessary computations. The sea ice and ocean models are set up on the same mesh. This is done to facilitate model comparison and so that output from one model easily can be used as input in other models. In addition, in the simulations with the coupled ocean and sea ice model it is necessary, or at least preferable, to use the same mesh.

As described in Chapter 2 it is preferable for the ocean simulations to have a high resolution on steep bottom slopes to decrease the truncation error on the baroclinic pressure gradient. Also for the barotropic currents the bottom slopes should be well resolved due to the topographical steering and the resolution therefore depends on the bathymetry with high resolution on the shelf break and the continental slope. Moreover, the resolution depends on the square root of the depth to get the same Courant number everywhere in order to achieve a better use of the time step, thus having high resolution on the shelf and coarse resolution on deep water. Finally the resolution was

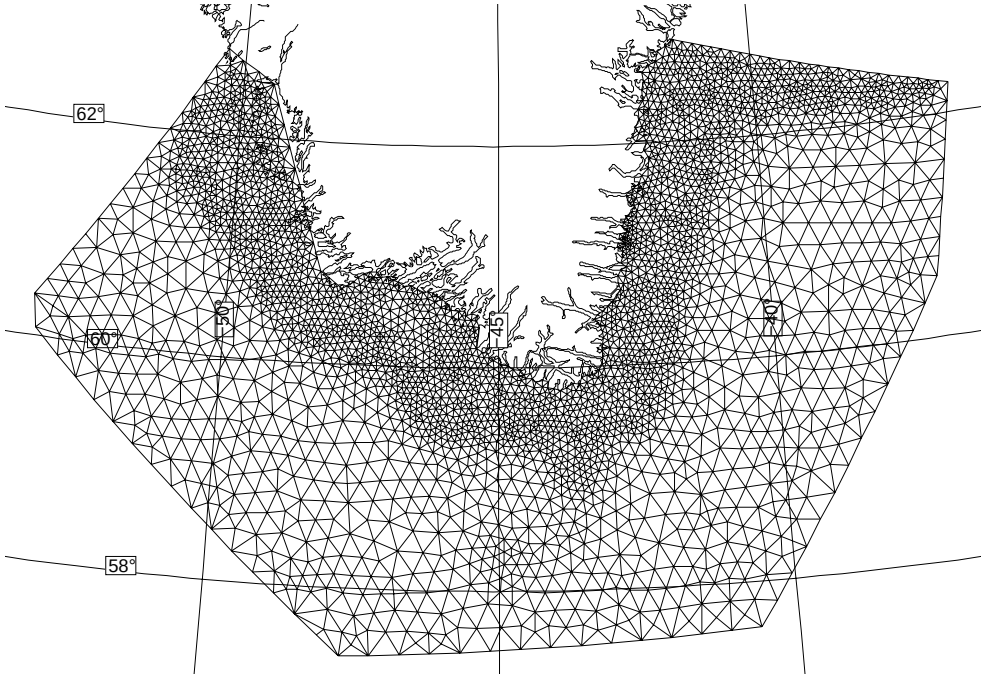


Figure 3.3: Computational mesh with 3420 nodes and 6611 elements.

increased close to the inflow boundary in order to decrease the error sources at this boundary, such that the inflow is well-behaved and smooth.

Even though the ocean model is mainly used as forcing for the sea ice model in the work presented here, and the emphasis and especially the validation are on the results from the sea ice model, the criteria for the resolution are mainly determined by considerations concerning the ocean models. There are several reasons for this. First of all, due to the decision of having one mesh which is used in all simulations, it should meet both the sea ice and the ocean needs, particularly with respect to the coupled ice-ocean simulations. Furthermore, it is difficult in advance to define criteria for the sea ice simulations, since this involves high resolution on the ice edge and where the ice is found, which is unknown before the simulations are actually performed. Of course, the mesh could be constructed based on observations, for example those used for initial values. But due to the highly changing ice conditions in the area, this carries the risk of a mesh suitable only for a part of the simulation period. One solution could then be to use an adaptive mesh. This has not been investigated in this study, although it might also be beneficial for the advection calculations.

Instead, the more intuitive procedure is used, simply to construct the mesh based on some other criteria, no matter how, and then just check if there is high resolution where the ice is expected to be found. This seems to be the case, since the mesh based on the ocean criteria gives high resolution on the shelf and continental slope, where most of the ocean dynamics take place and where the ice is usually found. Thus, it seems to be a suitable mesh for both sea ice and ocean simulations.

When the resolution is given by the bathymetry, as is done here, the node separation goes to zero as the depth goes to zero at the coast, and becomes very large for the deep areas. It is therefore necessary to specify proper minimum and maximum node separations. Requirements on the resolution also appear from the formulation of the sea ice model (Flato, 1998). A lower

bound on the resolution is defined by the fact that the assumption of the ice as a continuum with a concentration and thickness field breaks down if the scale gets too small. On the other hand, if the scale gets too large, real geophysical variations are not resolved. Based on observations Flato (1998) estimates the lower and upper bound to be roughly 10 and 200 km for the Arctic. It is expected that the lower bound of the resolution is smaller in the area around Cape Farewell than in the Arctic, since the floe size is smaller, and the minimum and maximum separation between two nodes are chosen to be 5 and 50 km, respectively.

## 3.3 Data

This section describes the data that are used for initial and forcing fields and for validation of the model simulations. Except for the wind fields and the ice maps, all data are freely available on the internet (see appendix C).

### 3.3.1 Bathymetry

The bathymetry shown in figure 3.2 and used in the mesh generation and in the ocean simulations is the ETOPO5 bathymetry (NGDC, 1988). It has a global coverage of 5x5 minutes, i.e. a resolution of about 4.5 km in the east-west direction and 9 km in the north-south direction in the area around Cape Farewell. The World Data Bank II coastline is used to extract the land boundary and is also shown in figure 3.2. It has a resolution of approximately 500 meters.

### 3.3.2 Temperature and salinity fields

The ocean simulations require initial temperature and salinity fields. It takes many profile measurements to get a reasonable coverage and therefore a climatology is usually used. The Levitus climatology (Levitus et al., 1994; Levitus and Boyer, 1994) is widely used (e.g. Ezer and Mellor, 1994, 1997) and there is a new global climatology (Gouretski and Jancke, 1998) that is partly based on the Levitus data. In this study the Levitus monthly mean salinity and potential temperature for March are used for the baroclinic forcing. Figures 3.4 and 3.5 show the surface temperature and salinity fields. It is noted that numerical models usually solve for potential rather than *in situ* temperature. The potential temperature is available from the Levitus climatology as monthly and annual means, while the *in situ* temperature is also available as seasonal mean.

The advantage of the Levitus climatology and the reason to use it here, is that it covers the entire area and is easy to get and use. The greatest disadvantage is that the fields are very smooth, as clearly seen in figures 3.4 and 3.5. This is caused by the spatial interpolation and time averaging procedures and further by the low coverage of observations in the polar regions. Unfortunately, the Levitus climatology seems to be too smooth, and the baroclinic forcing is found to have no real effect on the results of the limited area simulations performed in this study as discussed in section 4.3.

Mortensen (1997) performed simulations of a limited area of the Denmark Strait and waters around Iceland. Instead of using climatological temperature and salinity fields for the initialisation, he constructed his own data set on a regional scale and representative for a specific year. Even though this might be the preferred procedure, it is regarded as outside the scope of this study.

Holland et al. (1996) performed a sensitivity test of the temperature and salinity fields for simulations of the Arctic ocean and the Greenland-Iceland-Norwegian Sea with a resolution of 2 degrees. They made simulations with and without the Levitus data as initial values and found

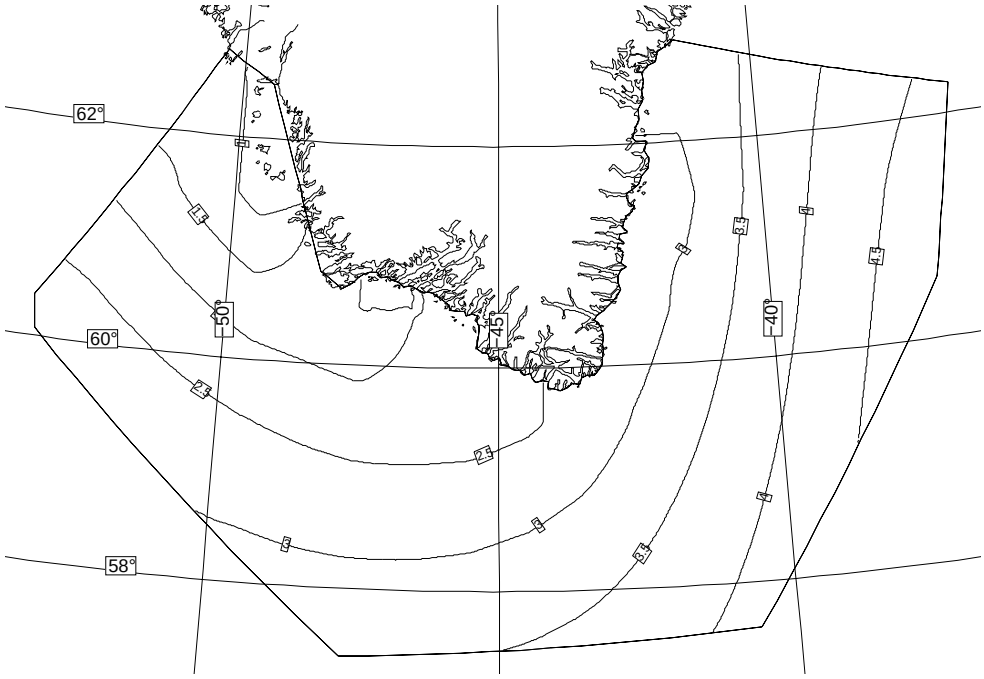


Figure 3.4: March surface temperature field from the Levitus climatology.

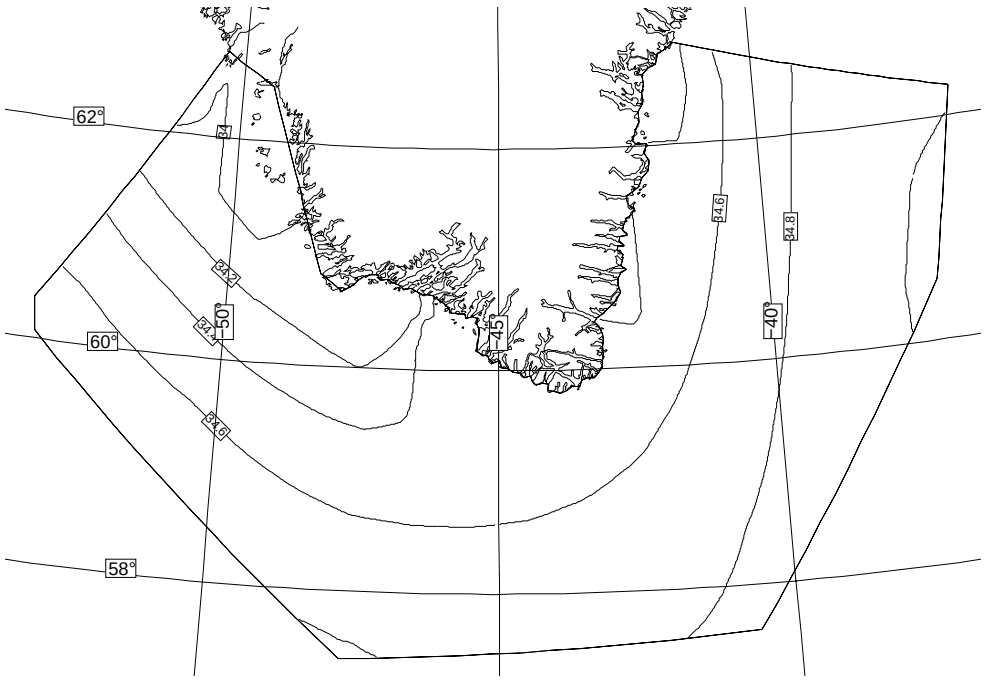


Figure 3.5: March surface salinity field from the Levitus climatology.

that the horizontal density variations in the Levitus data did influence the result. Thus, on a large scale the climatological fields apparently capture the important structure of the density field and perform well.

### 3.3.3 Wind fields

The models are forced by the analysed wind fields from the High Resolution Limited Area Model (HIRLAM) (Källén, 1996), run operationally at the Danish Meteorological Institute. The model is set up for an area covering the North Atlantic. The wind fields are available every 6 hours. Figure 3.6 shows the wind fields at 06 GMT at the first 4 and the last 4 days of the simulation period.

### 3.3.4 Ice concentration

The ice concentration fields for initialisation and for validation of the sea ice model are obtained from sea ice maps produced at the Danish Meteorological Institute. The ice maps are based on Radarsat images. Figure 3.7 shows the ice concentration at March 17, 20 and 27 all at 09 GMT. The ice is situated on the shelf, indicating the drag from the East Greenland Current. The ice edge is very sharp east of Greenland and the concentration is high with values of about 90% all the way from the inflow boundary to Cape Farewell. When the ice has passed Cape Farewell the concentration rapidly decreases, probably due to melting.

In the first 3 days only small changes of the concentration field are seen, while the next 7 days are much more dynamically active. A few distinct features are pointed out here and used in the discussion in section 5.5.

First, it is noticed that at March 17 the ice edge off the east coast is almost a straight line with a distance to land varying from about 50 km at the inflow boundary to about 10 km at Cape Farewell. The ice extends about 200 km further to the west of Cape Farewell and there separates from the land. Three days later, at March 20, the ice edge is still about 50 km off land at the inflow boundary, but now makes a sudden turn towards land around 61°N. The ice extends further along the west coast and has moved northward and is almost connected to the land. Another 7 days later at March 27, the ice cover along the east coast has broadened to a width of 50-60 km all the way to Cape Farewell and the ice edge is now meandering. A few of these meanders will be used in the discussion section 5.5 and have been marked (A, B and C) to clarify the discussion. South of Cape Farewell an ice free area has formed and to the west the ice has moved away from the coast and is spread out, extending the area of the ice cover substantially.

On the plot of March 20 it seems as if there is no ice just inside the inflow boundary. The reason for this apparent ice free area is simply that the observations do not cover the total domain at that date and it is expected that, in reality, the ice did extend all the way along the east coast.

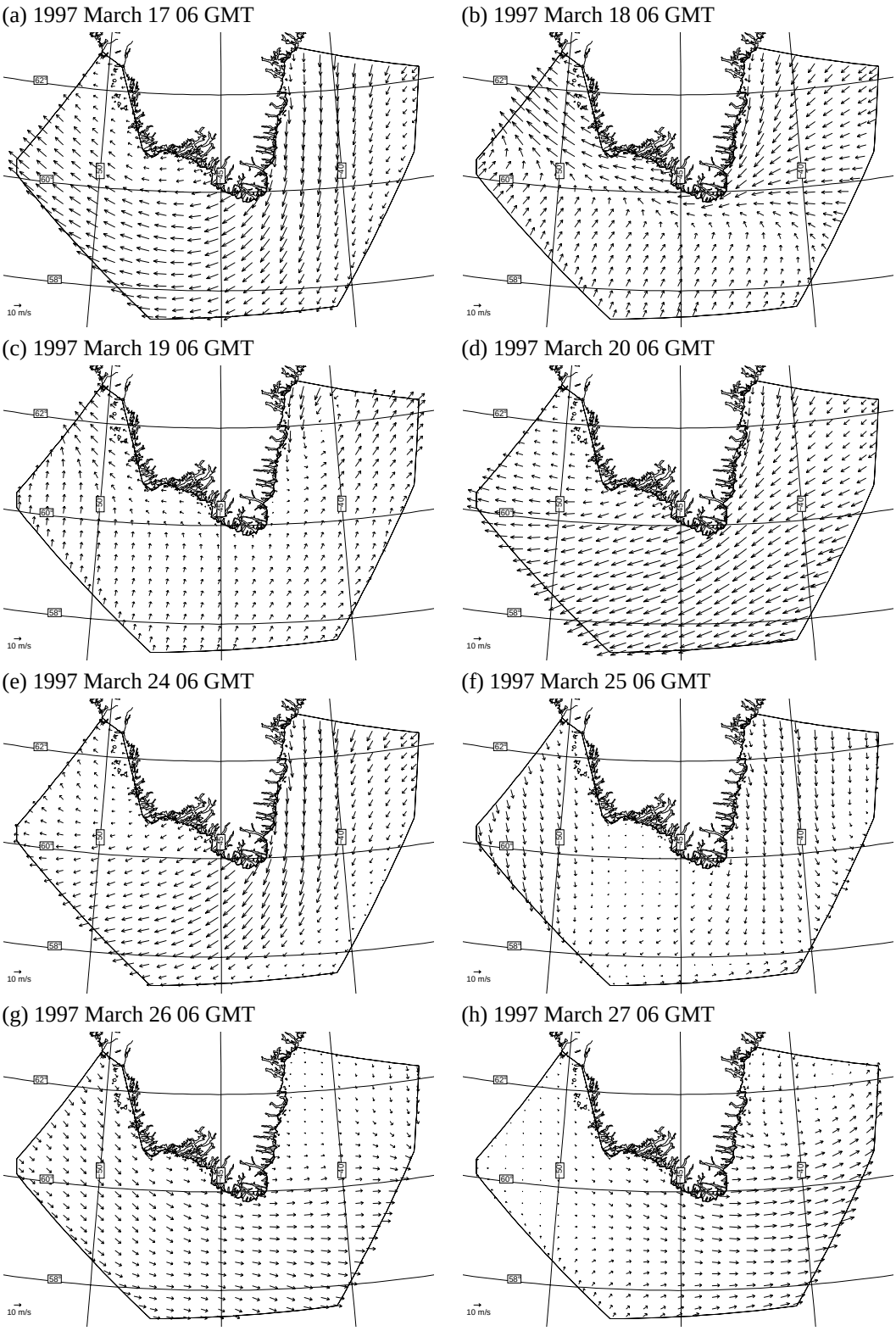


Figure 3.6: Analysed wind fields from HIRLAM.

(a) 1997 March 17 09 GMT

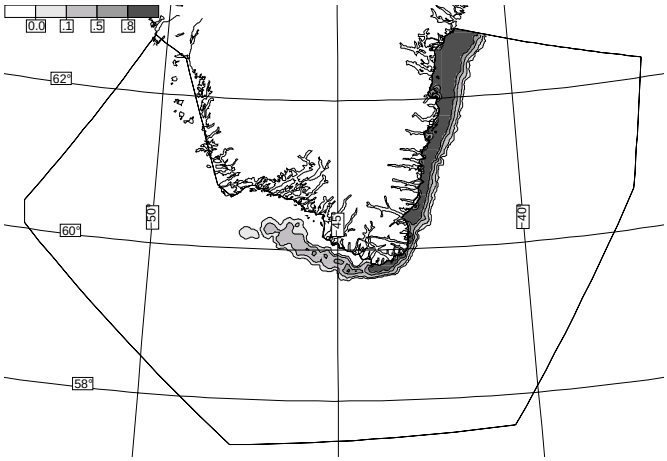


(b) 1997 March 20 09 GMT

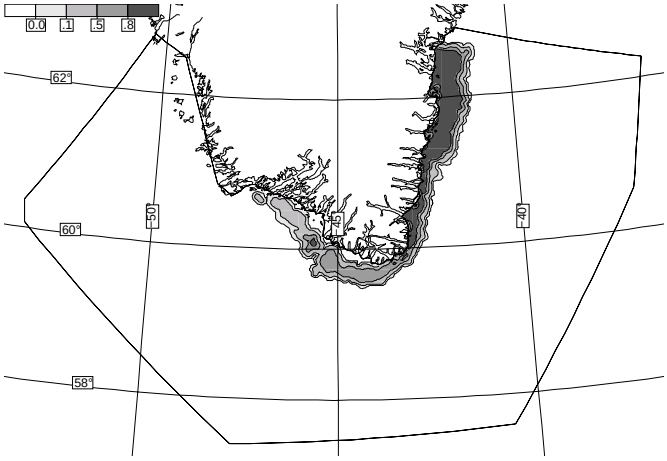


(c) 1997 March 27 09 GMT

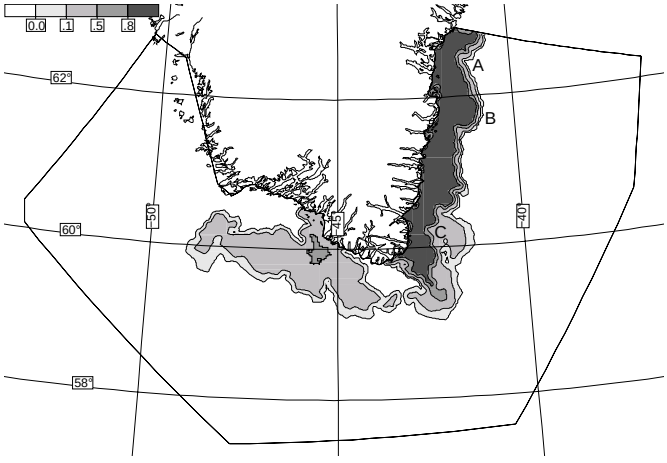


Figure 3.7: Sea ice concentration fields.

# Chapter 4

# Finite element ocean simulations

## 4.1 Finite element method

In Chapter 2 it was found that for ocean models with terrain following coordinates ($\sigma$-coordinates) it is necessary, or at least preferable, to maintain high spatial resolution on the steep bottom topography, if a density stratification is present, in order to minimise the error from the numerical treatment of the pressure gradient. Simulations with high resolution were performed, but due to the constant grid size the resolution was high everywhere, including areas where it was not needed, causing unnecessary computation. Further, as mentioned in section 3.2, with the grid size proportional to the square-root of the depth, the Courant number on the external mode will be uniform, making a better use of the time step.

It is thus preferable when using a variable grid size to be able to resolve interesting or necessary features, while still having low resolution elsewhere. This is one of the reasons for leaving the finite difference method in favour of the finite element method in this study. Whereas the finite difference grid always contains some kind of regularity or structure, the finite element method uses an unstructured mesh, i.e. there is no specific requirement[1] on the position of the nodes. This provides a high degree of freedom in varying the resolution, as for example seen in figure 3.3. The variable grid size can to some extent be achieved with the finite difference method by using curvilinear coordinates (e.g. Ezer and Mellor, 1994), or by nesting grids of different resolution into each other (e.g. Vested et al., 1995). The nesting technique is known to produce small scale noise at the grid boundaries, while the curvilinear coordinates seem to perform well, but none of them are as flexible as the finite element method.

Another reason for using the finite element method is the smooth representation of the coasts. Due to the unstructured mesh and the linear elements an irregular coastline is piecewise linearly represented (see figure 4.1a) and the method is well suited to handle the irregular coastal areas. With the finite difference method the coastline becomes staircase-shaped due to the pointwise representation. The shape of the coast depends on the orientation of the computational grid to the coast, as indicated in figure 4.1b,c. The problem is described by Adcroft and Marshall (1998), who found that the circulation is sensitive to the orientation of the computational grid to the coast.

The disadvantages with the finite element method is that it is not as easy to apply as the finite difference method and it might require more cpu time (Meyers and Weaver, 1995). Nevertheless, the advantages mentioned above makes the finite element method an attractive method for ocean

[1] In the two dimensional mesh with triangular elements, these should not be extremely distorted. Ideally, the elements should be equilateral triangles. This is not a limitation in practice.

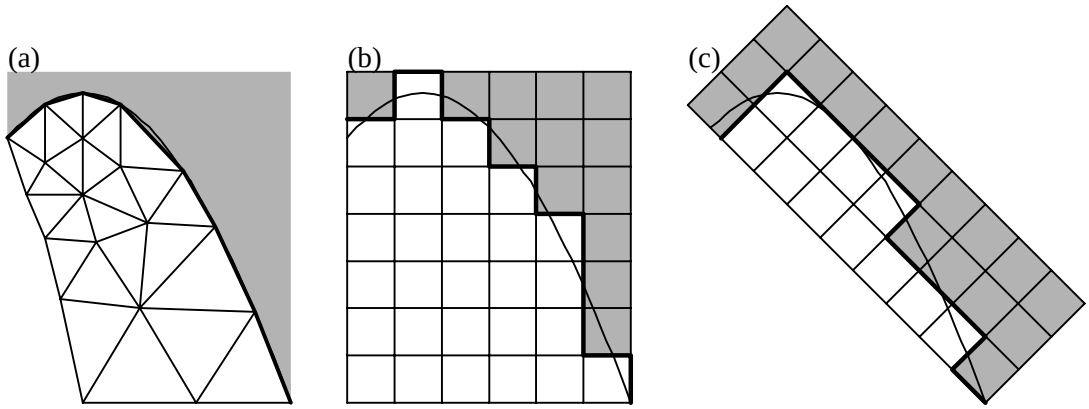


Figure 4.1: Representation of coastline. (a) Finite element method. (b) Finite difference method. (c) Finite difference method with rotated grid.

studies and forecasting.

## 4.2 Two ocean models

This chapter describes the simulations of the Cape Farewell area with two finite element ocean models, Fundy and Quoddy. Fundy is a diagnostic model, i.e. the calculations are based on specified baroclinic forcing. Quoddy is a prognostic model, i.e. it is a time stepping model, where the temperature and salinity fields are dependent variables, developing with time. They belong to the same family of finite element ocean models and possess many similarities, as for example in the representation of the mesh.

In both models, the mesh basically consists of a 2-dimensional horizontal mesh of triangles (figure 3.3) and a 1-dimensional vertical mesh discretised into the same number of levels at each horizontal node. The grid is terrain-following with the lower level at the bottom and the upper level following the sea surface. This gives a mesh that is slightly more general than the $\sigma$-coordinates used in Chapter 2, since the only restriction is that the number of vertical nodes is the same everywhere, while, in principle, it is possible to use different vertical resolution at various places.

The combination of the two models is advantageous. The diagnostic model solves for the dynamical variables, i.e. elevation and current. These are then used as initial fields in the prognostic model. This saves the long spin-up simulation usually necessary to get the dynamics in balance with the diagnostic forcing fields, i.e. salinity and temperature. In addition, the climatological salinity and temperature fields are provided in $z$-levels. These are used for the pressure gradient calculation in the diagnostic model, thereby avoiding the problems described in Chapter 2. The model interpolates the pressure gradient field to the terrain-following coordinates. The same interpolation routine is used to interpolate salinity and temperature. The diagnostic model is thus used to interpolate the diagnostic fields to the mesh and provides all initial fields for the prognostic model.

## 4.3 Linear diagnostic model

The linear harmonic model, Fundy, is used for the diagnostic simulations. The model is described in detail by Lynch and Werner (1987), Lynch et al. (1992) and Greenberg et al. (1998). The time dependence is based on the assumption that the dependent variables are harmonic, oscillating with frequency $\omega$. The model is not time-stepping, but instead operates in the frequency domain. The variables are written as $\phi(x,y,t) = \phi_0 e^{i(\omega t+\varphi)}$ with $\phi_0(x,y)$ the amplitude and $\varphi(x,y)$ the phase, and where $i$ is the imaginary unit with the property $i^2 = -1$. The time derivatives are then $\frac{\partial \phi}{\partial t} = i\omega\phi$. The elevation $\zeta$ is calculated according to the depth-integrated continuity equation

$$i\omega\zeta = -\nabla_{xy} \cdot \left(h\overline{\vec{v}}\right) \tag{4.1}$$

where $h$ is the depth and $\overline{\vec{v}}$ is the depth averaged velocity. The velocity $\vec{v}$ is found from the momentum equation

$$i\omega\vec{v} + \vec{f} \times \vec{v} = -g\nabla_{xy}\zeta - \frac{g}{\rho_0}\int_z^0 \nabla_{xy}\rho dz + \frac{\partial}{\partial z}\left(N_m \frac{\partial \vec{v}}{\partial z}\right) \tag{4.2}$$

where $\vec{f}$ is the Coriolis parameter written as a vector pointing upward, $g$ is the gravitational acceleration, $\rho$ is the density, and $N_m$ is the vertical turbulent mixing coefficient.

For a given frequency, the model equations with specified density gradient, wind stress, and boundary conditions, can be solved for amplitudes and phases. Zero frequency gives the steady-state solution. If there is more than one frequency, a simulation is performed for each of them. Since there is no non-linear interaction, the solutions are simply added together.

## 4.4 Linear diagnostic simulations

### 4.4.1 Set-up

Simulations with the diagnostic ocean model are performed for the Cape Farewell area on the mesh described in section 3.2. The simulations are performed for zero frequency giving a steady-state solution. All the simulations are made on the same set-up, with different choices of parameters in order to investigate the importance of the different terms. The simulations are summarised in table 4.1. The results are shown as elevation and velocity fields in figure 4.2. There is no direct comparison with observations.

| No. | T and S | $C_{aw}$ | cpu (s) | velocity (m/s) |
|---|---|---|---|---|
| F0 | barotropic | 0 | 3.4 | 0.21 |
| F1 | Levitus | | 9.8 | 0.19 |
| F2 | | $1.4 \cdot 10^{-3}$ | 3.6 | 0.69 |
| F3 | | $0.7 \cdot 10^{-3}$ | 3.6 | 0.45 |

Table 4.1: Simulations performed with the diagnostic ocean model for the Cape Farewell area. Where no value is given, it is as in F0. The velocity is found about 50 km south of Cape Farewell (position marked on figure 3.2).

Seven nodes are used in the vertical. This is very few, and many more could easily be afforded both with respect to memory requirements and time usage. Since the output of the diagnostic simulations is used as input for prognostic simulations, the vertical meshes should agree. The prognostic model is more demanding and the relatively coarse vertical resolution is because of these simulations.

As mentioned in section 3.2, it is assumed there is inflow at the northernmost boundary normal to the east coast. This is achieved by specifying the elevation along this boundary with zero elevation at the northeast corner of the domain over deep water increasing towards the coast. The slope of the sea surface is chosen by trial and error. From simulations on a larger domain (not shown) it was found that the strongest surface current and the steepest slope of the sea surface are found on the continental slope. This is a reasonable result, argued for by the topographic steering. Thus, as seen in figure 4.2 the boundary conditions are set to zero elevation on the deep water with a high increase over the continental slope and a small increase on the shelf to a value of almost 0.25 m at the coast. At the rest of the open boundaries the water is allowed to flow out according to geostrophy.

One simulation is forced by variations in the density field. The baroclinic forcing is based on the Levitus climatological salinity and potential temperature fields. The density is calculated as a function of salinity, potential temperature and pressure $\rho(S, \theta, p)$ (eqs. 4.20-4.21).

Two simulations are forced by analysed HIRLAM winds from March 17 (see figure 3.6a). A quadratic drag law is used. The drag coefficient is a constant set to $1.4 \cdot 10^{-3}$ for F2 and half the value for F3. The value $1.4 \cdot 10^{-3}$ is given by Pond and Pickard (1983).

### 4.4.2 Results

The elevation and velocity fields of the simulations are shown in figure 4.2.

The barotropic simulation, F0, without wind forcing is depicted as the reference solution of the linear model for the intercomparisons and is used as initial condition for the simulations with the time stepping ocean model (section 4.5), and for the ocean forcing in the sea ice simulations (section 5.5). The elevation field follows closely the bathymetry, as expected. For example, the meanders on the elevation isolines between the inflow boundary and 62°N are related to the 250 m and 1500 m isobaths (see figure 3.2) and the spur in the continental slope just south of Cape Farewell is clearly seen in the elevation field. The highest current velocity is found on the continental slope. On the shelf the velocity is smaller and the velocity is very small at deep water. The sea surface current is 0.21 m/s about 50 km south of Cape Farewell. In general the current is up to about 0.3 m/s, with a maximum value of 0.55 m/s. The maximum value is found just inside the inflow boundary and is probably an artifact of the boundary condition. The simulated velocity is in agreement with observations, for example Uotila et al. (1997) found velocities up to 0.5 m/s in the East Greenland Current.

The baroclinic simulation, F1, is almost indistinguishable from F0 indicating that the baroclinic forcing is not important for the circulation. At the position south of Cape Farewell the current is slightly smaller, 0.19 m/s. The maximum current speed is 0.55 m/s as in F0 and found at the same node just inside the inflow boundary. Small differences are also found close to land. The elevation is slightly higher within F1 than within F0 especially at the west coast, where the surface current is slightly larger too.

As discussed previously (section 3.3.2) the reason for the similarity between the barotropic and the baroclinic simulations must be sought in the climatological temperature and salinity fields that are used for the baroclinic forcing. They are based on measurements from several years resulting

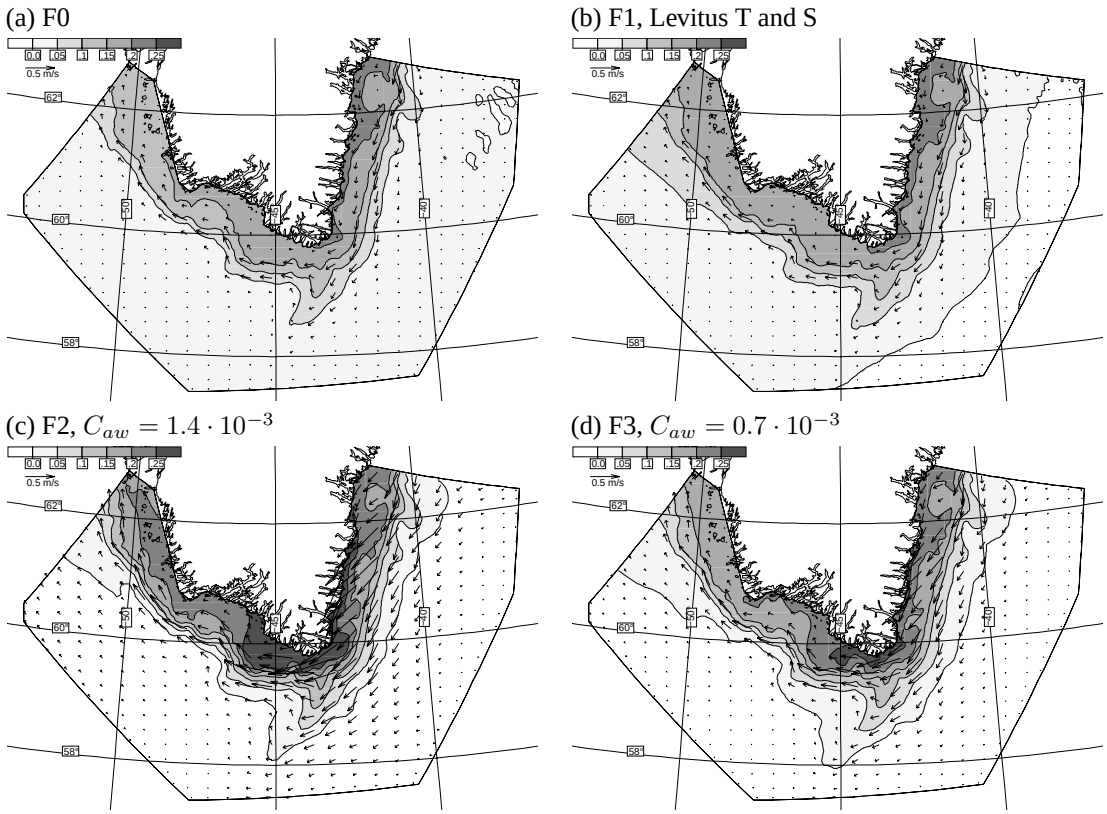


Figure 4.2: Sea surface current and elevation, linear diagnostic simulations.

in very smooth fields with weak baroclinic forces. Since the effect of the baroclinicity is so small, it is regarded as no real improvement to the result, and F0 will be used for the ocean forcing in the sea ice simulations.

The two simulations, F2 and F3, are forced by the wind field of March 17 with different drag coefficients. The general result is the same for the two simulations, although the response to the wind forcing is clearly demonstrated to depend upon the magnitude of the drag coefficient. As the wind is toward the south and west the water is forced in the same direction as the existing current pattern of F0 resulting in a 5-10 cm increase of the coastal set-up. The sea surface elevation still reflects the bottom topography.

The surface current increases substantially with the drag coefficient. For example, at the given position south of Cape Farewell the current speed is 0.21 m/s for F0, 0.45 m/s for F3 and 0.69 m/s for F2. The maximum speed is 0.75 m/s in F3 and 1.43 m/s in F2 and is found at the same node in the two simulations close to land. These high maximum values are probably due to a combination of the wind drag and land effects.

## 4.5 Nonlinear prognostic model

### 4.5.1 Model description

The prognostic simulations are performed with Quoddy. The model is described in detail by Lynch and Werner (1991) and Lynch et al. (1996). It is non-linear, 3-dimensional and hydrostatic, and includes a free surface and the 2.5 turbulence closure scheme by Mellor and Yamada (1982).

The Navier-Stokes equation is solved for the horizontal part of the velocity (momentum) with the usual Boussinesq and hydrostatic approximations

$$\frac{d\vec{v}}{dt} + \vec{f} \times \vec{v} = -g\nabla_{xy}\zeta - \frac{g}{\rho_0}\int_z^\zeta \nabla_{xy}\rho dz + \nabla_{xy}\left(A_h \nabla_{xy} \cdot \vec{v}\right) + \frac{\partial}{\partial z}\left(N_m \frac{\partial \vec{v}}{\partial z}\right) \tag{4.3}$$

where $\vec{v}$ is the velocity, $\vec{f}$ is the Coriolis parameter written as a vector pointing upward, $g$ is the gravity, $\zeta$ is the sea surface elevation, $\rho$ is the density, $A_h$ is the horizontal mixing coefficient, and $N_m$ is the vertical turbulent mixing coefficient. The vertical velocity $w$ is calculated using the continuity equation

$$\frac{\partial w}{\partial z} = -\nabla_{xy} \cdot \vec{v} \tag{4.4}$$

The free surface is defined by depth integrating the continuity equation

$$\frac{\partial \zeta}{\partial t} = -\nabla_{xy} \cdot \int_h^\zeta \vec{v} dz \tag{4.5}$$

This equation is not solved directly for the elevation. Instead it is rearranged together with eq. 4.3 to produce a wave equation. This is to preserve the gravity wave performance on the simple elements (Lynch and Gray, 1979). Equation 4.5 is differentiated with respect to time

$$\frac{\partial^2 \zeta}{\partial t^2} = -\nabla_{xy} \cdot \frac{\partial}{\partial t}\int_h^\zeta \vec{v} dz = -\nabla_{xy} \cdot \left(\vec{v}|_{z=\zeta}\frac{\partial \zeta}{\partial t} + \int_h^\zeta \frac{\partial \vec{v}}{\partial t} dz\right) \tag{4.6}$$

and adding eq. 4.5 multiplied a constant $\tau_0$ gives the wave equation

$$\frac{\partial^2 \zeta}{\partial t^2} + \tau_0 \frac{\partial \zeta}{\partial t} = -\nabla_{xy} \cdot \left(\vec{v}|_{z=\zeta}\frac{\partial \zeta}{\partial t} + \tau_0 \int_h^\zeta \vec{v} dz + \int_h^\zeta \frac{\partial \vec{v}}{\partial t} dz\right) \tag{4.7}$$

The last term on the right hand side is found by depth integrating eq. 4.3.

The spatial variations are discretized with the finite element method, with a finite difference time stepping. A three level time discretization

$$\zeta \approx \frac{\theta}{2}(\zeta^{n+1}+\zeta^{n-1})+(1-\theta)\zeta^n \qquad \frac{\partial \zeta}{\partial t} \approx \frac{\zeta^{n+1}-\zeta^{n-1}}{2\Delta t} \qquad \frac{\partial^2 \zeta}{\partial t^2} \approx \frac{\zeta^{n+1}-2\zeta^n+\zeta^{n-1}}{\Delta t^2} \tag{4.8}$$

with the weight $\theta \in [0;1]$, is used for the wave equation, and a two level ($n-1$ and $n$) discretization is used for the momentum equation.

### 4.5.2 Changes to the model

A few changes to the source code of the model have been made. Of these the implementation of the preconditioned conjugate gradient method is the major change. This iterative method is substituted for the direct solution of the wave equation originally performed in the model by the

LU method. Furthermore, the equation of state has been under consideration. First, a possible optimisation of the algorithm is investigated, motivated by the fact that the equation of state is a computationally expensive task in an ocean model. Secondly, the pressure dependence on the density is implemented. The topics of the conjugate gradient method and the equation of state are described in the following sections.

Finally, a flow relaxation scheme (see e.g. Martinsen and Engedahl, 1987) is implemented for the open boundary condition. In the diagnostic simulations a geostrophic condition was applied at the outflow boundary, but this conflicts with the conjugate gradient method, as described below. Instead flow relaxation is used for a zone along the boundary, where the temperature and salinity are relaxed toward the climatological fields, and horizontal velocities and elevation are relaxed toward the diagnostic solution. This means that after calculation of the value of a variable $\phi$, it is updated according to

$$\phi = \alpha\phi_{intern} + (1-\alpha)\phi_{extern}, \tag{4.9}$$

where $\phi_{intern}$ is the solution of the prognostic model before the relaxation, $\phi_{extern}$ is an external solution, i.e. the climatology and diagnostic solution and $\alpha$ is a weight varying from 0 at the boundary to 1 in the domain. In the interior domain inside the relaxation zone the internal solution is used by setting $\alpha = 1$. To facilitate a smooth transition between the internal domain and the relaxation zone, $\alpha$ varies quadraticly with the distance from the boundary, with the requirement that $\frac{\partial\alpha}{\partial s} = 0$ at the interface between the relaxation zone and the internal domain, with s the distance from the boundary.

This kind of open boundary is not mass- and momentum-conserving and is not physically and mathematically founded, but it seems to work. The same boundary condition is used in the simulations of the laboratory experiment described in section 2.3. It should be noted that when the solution is relaxed to climatological fields as is done here (and in section 2.3) the relaxation zone is sometimes called a sponge layer (e.g. Haidvogel and Beckmann, 1999).

### 4.5.3 Conjugate gradient method

One of the main tasks in the model is to solve the wave equation, which in the discrete formulation is formulated as a system of linear equations

$$A\vec{x} = \vec{b} \tag{4.10}$$

where $A$ is a $N \times N$ dimensional matrix, and $\vec{b}$ and $\vec{x}$ are $N$ dimensional vectors, with $N$ equal to the number of nodes. $A$ is defined by the dependency of the nodes on each other, $\vec{b}$ includes all terms evaluated at known time levels $n$ and $n-1$ and $\vec{x}$ is the change of the elevation with time, $x_i = \zeta_i^{n+1} - \zeta_i^{n-1}$. $A$ is sparse, banded, symmetric and positive definite. Furthermore, $A$ is constant in time, and originally, eq. 4.10 is solved with a LU decomposition which then is performed only once and the work needed in each time step is just a forward and a backward substitution. Due to the symmetry and positive definiteness, a Cholesky decomposition can be used (Kreyszig, 1988). This means that the upper triangular matrix is the transpose of the lower, and $A = L^T L$. Storage requirements are kept down, because $A$ is banded and symmetric, and it is therefore important to have as low a bandwidth as possible. For the mesh used here the half bandwidth is 64. Since there are 3420 nodes in the mesh, $A$ is actually a $3420 \times 3420$ matrix, but it is possible to store it in an array of dimensions $3420 \times 64$.

Due to the sequential execution of the LU method the algorithm is not easy parallelised and vectorised. This was the main reason to investigate the possibility of using other methods.

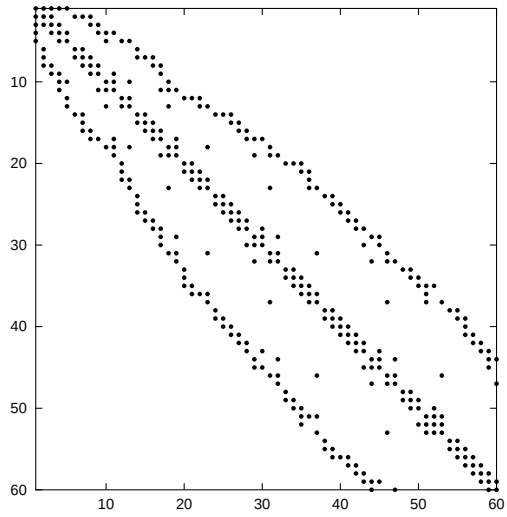


Figure 4.3: Upper left part of the sparse matrix. Numbers different from zero are marked.

Utilising that $A$ is symmetric and positive definite, the preconditioned conjugate gradient method has been implemented in the model as an alternative to the LU method. The theory leading to the algorithm of the conjugate gradient method will not be examinated here, see for example Golub and Van Loan (1989), Schewchuk (1994) or Van de Velde (1994) for a thorough treatment.

The conjugate gradient method is an iterative method, which solves eq. 4.10 given the matrix $A$ and the vector $\vec{b}$ and an initial guess $\vec{x}_0$. $A$ and $\vec{b}$ are given by the model equations, while $\vec{x}_0$ is specified by the user. Then the algorithm is

$$
\begin{aligned}
&k = 0;\ \vec{r}_0 = \vec{b} - A\vec{x}_0;\ C = \text{diag}(A);\ \vec{z}_0 = C^{-1}\vec{r}_0;\ \vec{p}_0 = \vec{z}_0;\\
&\text{do while } (k < N \text{ and } \vec{r}_k^T\vec{z}_k > \epsilon\vec{r}_0^T\vec{z}_0)\\
&\quad \alpha_k = \frac{\vec{r}_k^T\vec{z}_k}{\vec{p}_k^T A\vec{p}_k}\\
&\quad \vec{x}_{k+1} = \vec{x}_k + \alpha_k\vec{p}_k\\
&\quad \vec{r}_{k+1} = \vec{r}_k - \alpha_k A\vec{p}_k\\
&\quad \vec{z}_{k+1} = C^{-1}\vec{r}_{k+1}\\
&\quad \beta_k = \frac{\vec{r}_{k+1}^T\vec{z}_{k+1}}{\vec{r}_k^T\vec{z}_k}\\
&\quad \vec{p}_{k+1} = \vec{z}_{k+1} + \beta_k\vec{p}_k\\
&\quad k = k + 1
\end{aligned}
\tag{4.11}
$$

where $k$ is an iteration counter, $C$ is a preconditioning matrix (described below) here implemented as a diagonal matrix consisting of the diagonal elements of $A$, and $\vec{r}$ is the residual $\vec{r} = \vec{b} - A\vec{x}_k$. $\vec{z}$ and $\vec{p}$ are vectors, $\alpha$ and $\beta$ are scalar products and $\epsilon$ is a small number defining the stopping criterion (described below).

One of the advantages of the method is that $A$ need not be inverted directly, but is only used in a matrix-vector multiplication. This makes the method useful for sparse matrices. However, the method will not be efficient if the matrix is not sparse, since the multiplication then would be

too computationally expensive. From figure 4.3 it is seen that $A$ is indeed very sparse, with only a few non-zero elements. For the mesh used here the sparsity, i.e. the maximum number of non-zero elements in a row is 7. This means that $A$ is actually stored in an array of dimension $3420 \times 7$. The conjugate gradient method thus uses less computer memory than the LU method.

Owing to the nature of the iterative procedure, the solution and the number of iterations and, thereby, the execution time, depend on the chosen accuracy through the specification of $\epsilon$. This is one of the greatest disadvantages of the method and is tested below.

Another disadvantage is that $A$ has to be symmetric. This excludes the geostrophic boundary conditions that would make $A$ non-symmetric.

The positive definiteness of $A$ ensures convergence independent of the initial guess and it can be shown that the method will converge in at least $N$ iterations. For any mesh but for small test cases this is a large number and would require an incredible amount of computing. The strength of the method is that a satisfactory solution often is found in much fewer iterations.

Even though convergence is guaranteed, the algorithm should start with a sensible initial guess $\vec{x}_0$. $\vec{x}$ is the change of the surface elevation from one time step to the next. The $i$'th element of $\vec{x}$ is thus the change of elevation at the $i$'th node $\zeta_i^{n+1} - \zeta_i^{n-1}$. This is expected to be relatively small and the initial guess is simply zero, corresponding to steady state.

Improved convergence can be obtained by use of a preconditioner. This is called the preconditioned conjugate method and works by solving eq. 4.10 indirectly, by solving the equation multiplied on both sides of the equal sign by a matrix. After some rearranging one can get something very like the conjugate gradient method, but where the preconditioning matrix $C$ enters the algorithm in inverse form. From the derivation it follows that $C$, too, must be symmetric and positive definite. Setting $C$ to the unit matrix simply gives the conjugate gradient method without preconditioning.

It can be shown that the error in the k'th iteration is bounded by

$$\|\vec{x}_k - \vec{x}^*\|^2 \leq 2\|\vec{x}_0 - \vec{x}^*\|^2 \left(\frac{\sqrt{\kappa}-1}{\sqrt{\kappa}+1}\right)^k \tag{4.12}$$

where $\vec{x}^*$ is the true solution, i.e. $A\vec{x}^* = \vec{b}$, and $\kappa$ is the condition number of $C^{-1}A$ defined from a given matrix norm as

$$\kappa = \|C^{-1}A\| \cdot \|(C^{-1}A)^{-1}\| \tag{4.13}$$

If the spectral matrix norm is used, the condition number is the ratio of the maximum to the minimum eigenvalue of $C^{-1}A$. The eigenvalues are found by the power method as explained in appendix B. Equation 4.12 gives an upper limit of the error and shows that in each iteration this will decrease with $\frac{\sqrt{\kappa}-1}{\sqrt{\kappa}+1}$. This is in the following called the convergence factor. With a condition number of one, i.e. $C = A$, the method converges in one iteration. Thus, besides that the preconditioner must be symmetric and positive definite, the requirement is that the condition number for $C^{-1}A$ must be low. In other words, the preconditioner must be a good approximation to $A$.

$A$ enters the algorithm directly without being inverted. This is one of the strengths of the method. On the other hand $C^{-1}$ is used in the algorithm. Thus, apart from being a good approximation to $A$, the preconditioner must be easy to invert.

There is no unique way of constructing $C$, so $A$ has to be inspected. Figure 4.3 illustrates that $A$ is a band matrix with high density around the diagonal. Furthermore, the diagonal elements are in the order of 10 - 100 times larger than the off-diagonal elements. Thus, $A$ is diagonally dominant

and the preconditioner is chosen to be a diagonal matrix consisting of the diagonal elements of $A$

$$C_{ij} = \begin{cases} A_{ii} & i = j \\ 0 & i \neq j \end{cases} \tag{4.14}$$

This is called diagonal or Jacobi preconditioning and the inverse of $C$ is simply the reciprocal of the diagonal elements. It is stored as a vector, giving an easy implementation with small memory requirements.

Without the preconditioner the condition number is 218 giving a convergence factor of about 0.87. With the preconditioner the condition number is decreased to 6.05 with a convergence factor of 0.42. The efficiency of the preconditioner is due to the structure of $A$. Because $A$ is diagonally dominant with a relatively large difference in the values of the diagonal elements, the eigenvalues are also very different, with a large condition number as the result. With preconditioning the matrix $C^{-1}A$ is also diagonally dominant, but all diagonal elements are exactly one and the eigenvalues are all close to one, with a small condition number as the result.

The iteration procedure is terminated when the relative error on $\vec{x}$ is less than a small number. The error on $\vec{x}$ after $k$ iterations is defined as $\vec{x}_k - \vec{x}^*$. When multiplied by $A$ the error is expressed as the residual

$$r_k = -A(\vec{x}_k - \vec{x}^*) = \vec{b} - A\vec{x}_k \tag{4.15}$$

When the true solution is found, the error, and thereby the residual, is zero. The algorithm is terminated when

$$\vec{r}_k^T C^{-1} \vec{r}_k \leq \epsilon \vec{r}_0^T C^{-1} \vec{r}_0 \tag{4.16}$$

where $\epsilon$ is a small number and $C$ is the preconditioner. This ensures an upper bound of the error of $\|\vec{r}\|^2 \leq \epsilon \|\vec{b}\|^2$. Now the problem is to choose a proper value of $\epsilon$. It must be small enough to give a satisfactory solution of $\vec{x}$, but on the other hand $\epsilon$ should be large enough to give a quick execution.

### 4.5.4 Equation of state

As in other 3-dimensional ocean models the salinity and the temperature are prognostic variables and an equation of state is needed to close the system of equations. In the ocean both the *in situ* temperature (the temperature measured at a given position) and the density depend on the pressure. At higher pressure both temperature and density are increased. The pressure $p$ used here is defined as the pressure due to the weight of the water volume lying above, i.e. at the surface $p = 0$.

Actually, a numerical ocean model does not solve for *in situ* temperature, but for potential temperature. The latter is defined, as the temperature a given water parcel would have if it was moved adiabatically[2] to the surface. Thus the potential temperature is a measure of the content of heat in the water. Therefore, if a water parcel is moved to another depth, the potential temperature is unaltered, while the *in situ* temperature changes.

The present version of the model is built for coastal areas with small depth, where it is reasonable to ignore the pressure dependence on the temperature and the density. The potential and *in situ* temperature are therefore the same, and the density is calculated as a function of salinity $S$ and temperature $T$ according to the one atmosphere international equation of state of sea water

[2] Without exchange of heat with the surroundings.

| | | | | | |
|---|---|---|---|---|---|
| $a_0$ | 999.842594 | $b_0$ | 0.824493 | $c_0$ | $-5.72466 \cdot 10^{-3}$ |
| $a_1$ | $6.793952 \cdot 10^{-2}$ | $b_1$ | $-4.0899 \cdot 10^{-3}$ | $c_1$ | $1.0227 \cdot 10^{-4}$ |
| $a_2$ | $-9.095290 \cdot 10^{-3}$ | $b_2$ | $7.6438 \cdot 10^{-5}$ | $c_2$ | $-1.6546 \cdot 10^{-6}$ |
| $a_3$ | $1.001685 \cdot 10^{-4}$ | $b_3$ | $-8.2467 \cdot 10^{-7}$ | $d_0$ | $4.8314 \cdot 10^{-4}$ |
| $a_4$ | $-1.120083 \cdot 10^{-6}$ | $b_4$ | $5.3875 \cdot 10^{-9}$ | | |
| $a_5$ | $6.536332 \cdot 10^{-9}$ | | | | |

Table 4.2: Constants in the one atmosphere equation of state, eqs. 4.17 and 4.18.

(UNESCO, 1981)

$$\begin{aligned}\rho &= a_0 + a_1 T + a_2 T^2 + a_3 T^3 + a_4 T^4 + a_5 T^5 \\ &+ S(b_0 + b_1 T + b_2 T^2 + b_3 T^3 + b_4 T^4) \\ &+ S^{3/2}(c_0 + c_1 T + c_2 T^2) \\ &+ d_0 S^2\end{aligned} \tag{4.17}$$

with the constants $a_{0-5}$, $b_{0-4}$, $c_{0-2}$ and $d_0$ given in table 4.2. This polynomial is evaluated at all nodes in every time step, thus the algorithm is relatively expensive. Counting a power of an integer as a number of multiplications, for example $T^4$ as 3 multiplications, this algorithm executes 34 multiplications, 14 additions and 1 power of $3/2$.

By exploiting that the temperature enters almost all terms and can be set outside parenthesis, the polynomial is rewritten as

$$\begin{aligned}\rho &= a_0 + (a_1 + (a_2 + (a_3 + (a_4 + a_5 T)T)T)T)T \\ &+ S\Big[b_0 + (b_1 + (b_2 + (b_3 + b_4 T)T)T)T \\ &+ \sqrt{S}(c_0 + (c_1 + c_2 T)T) \\ &+ S d_0\Big]\end{aligned} \tag{4.18}$$

This algorithm executes only 14 multiplications, 14 adds and 1 square root, i.e. a reduction to about half the work of the original algorithm. A new routine of calculating the density is implemented using eq. 4.18 instead of eq. 4.17.

Figure 4.4 shows the density as a function of pressure at constant salinity of 35 psu and potential temperature of 2°C. At 500 m depth the density has increased by about 2.4 kg/m$^3$. In the model domain used in this study, the maximum depth is more than 3000 m. Then the density is increased by 13.7 kg/m$^3$, and it is expected that the pressure dependency should be included in the density calculations. The density is calculated at one atmosphere through eq. 4.17 or 4.18 according to the given salinity and temperature and then corrected for the pressure. It is of course possible to use eqs. 4.17 and 4.18 for the first step, since at one atmosphere the potential temperature is equal to the *in situ* temperature by definition. Two different routines performing the pressure correction are implemented and tested with respect to execution time.

In the international equation of state for sea-water (UNESCO, 1981) the density is corrected for the water pressure by $\rho(S,T,p) = \rho(S,T,0)/[1 - p/K(S,T,p)]$. The problem from a numerical perspective is that the secant bulk modulus $K$ is an even more complicated polynomial (not shown) in temperature, salinity and pressure than eq. 4.17, and that the *in situ* temperature is to

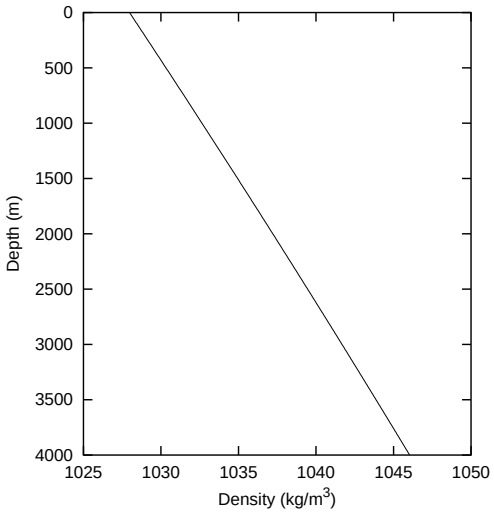


Figure 4.4: Density as function of pressure with constant salinity of 35 psu and potential temperature of 2°C. Calculated by eqs. 4.18, 4.20 and 4.21

be used. Jackett and McDougall (1995) let $K$ be a function of potential temperature instead, and Haidvogel and Beckmann (1999) give the secant bulk modulus and the density more conveniently, as functions of salinity, potential temperature and depth

$$\rho(S,\theta,z) = \frac{\rho(S,\theta,0)}{1+\frac{z}{K(S,\theta,z)}} \tag{4.19}$$

There is still the problem with $K$ that it is a fairly complex polynomial and slows down the execution. Instead, an algorithm proposed by Mellor (1991, 1996) is implemented. First the density at one atmosphere is calculated by 4.18. Then the density is corrected for the pressure as

$$\rho(S,\theta,p) = \rho(S,\theta,0) + \frac{p}{c^2}\left(1 - 2.0\cdot 10^{-5}\frac{p}{c^2}\right) \tag{4.20}$$

where

$$c = 1449.2 + 1.34(S-35) + 4.55\theta - 0.045\theta^2 + 8.21\cdot 10^{-7}p + 15.0\cdot 10^{-17}p^2 \tag{4.21}$$

with $c$ in m/s, $S$ in psu, $\theta$ in °C and $p$ in Pa. $c$ is close, but not exactly equal, to the speed of sound. Mellor (1991) compared values calculated by eqs. 4.20 and 4.21 with values of the standard equation of state and found very small deviations. Even with a pressure of $10^8$ Pa corresponding to a depth of approximately 10 km he found an error of the resulting geostrophic velocity much less than 1%. It is actually the depth and not the pressure that is known at the density points (that is why eq. 4.19 is convenient). For eqs. 4.20-4.21 the pressure is calculated by the hydrostatic equation $p = -g\rho_0 z$ with a constant reference density $\rho_0$. This seems to give a satisfactory accuracy and it is done, for example, in POM. However, it would not be much more difficult to perform a better integration down through the water column with the correct density.

## 4.6 Non-linear prognostic simulations

### 4.6.1 Set-up

Simulations with the prognostic ocean model are performed for the Cape Farewell area for the period March 17-27 1997 on the same mesh (figure 3.3) as the diagnostic simulations. Basically the same set-up is applied for the prognostic simulations. The simulations are summarised in table 4.3. The results are shown as elevation and velocity fields in figure 4.5, and surface current at a position about 50 km south of Cape Farewell is shown in figure 4.6. There is no direct comparison with observations.

Seven nodes are used in the vertical. This is a quite coarse resolution. In this study the results at depth are not investigated, since only the surface fields are used as forcing in the sea ice model. The time usage is kept low by using a small number of nodes in the vertical and in the horizontal to be able to explore the model through series of simulations.

The result of the diagnostic simulation F0 is used as initial condition. This saves the spin-up usually performed to let the dynamics adjust to the initial density field and boundary conditions.

As in the diagnostic simulations the inflow at the northernmost boundary normal to the east coast is given through a specification of the elevation along the boundary. The simulations are performed with a clamped boundary with the elevation kept at the initial values

$$\frac{\partial \zeta}{\partial t} = 0 \qquad \text{or} \qquad \zeta^{n+1} = \zeta^n = \zeta^0 \tag{4.22}$$

The rest of the open boundary (the deep water and normal to the west coast) is intended to be a “passive” open boundary, where the water is allowed to flow out of the domain. For this purpose a flow relaxation, described in section 4.5.2, is used. The width of the flow relaxation zone is 100 km, and the salinity, temperature, horizontal velocities and elevation are relaxed toward the climatological fields and the corresponding diagnostic solution, i.e. the same as the initial fields.

The simplest simulation Q0 is only forced by the boundary conditions. The result is expected to differ from that of F0 mainly due to non-linear effects. The other simulation Q1 is forced by 6-hourly analysed HIRLAM wind fields. The same drag law and coefficient as in F3 are used. Here the prognostic simulation is expected to show its superiority due to the inclusion of the evolution of the wind fields, and thereby of the ocean state, with time.

The efficiency of the conjugate gradient method is compared to the LU method through a number of simulations, using the elevation as an error measure. The simulations are performed for a 3 days period and are timed with the program gprof. Only the cpu usage and the error are reported. Because the iterative conjugate gradient method is implemented with an initial guess assuming stationarity, a simulation with only small changes in time would favour the conjugate gradient method. Therefore the test is performed with oscillating elevation, $\zeta = \zeta^0 \cos(\omega t)$, on the inflow boundary.

| No. | $C_{aw}$ | Equation of state | Boundary condition | Matrix solver | cpu (s) |
|---|---|---|---|---|---|
| Q0 | 0 | barotropic | clamped | PCGM | 7171.9 |
| Q1 | $0.7 \cdot 10^{-3}$ | | | | 7185.3 |

Table 4.3: Simulations performed with the prognostic ocean model for the Cape Farewell area. Where no value is given, it is as in Q0.

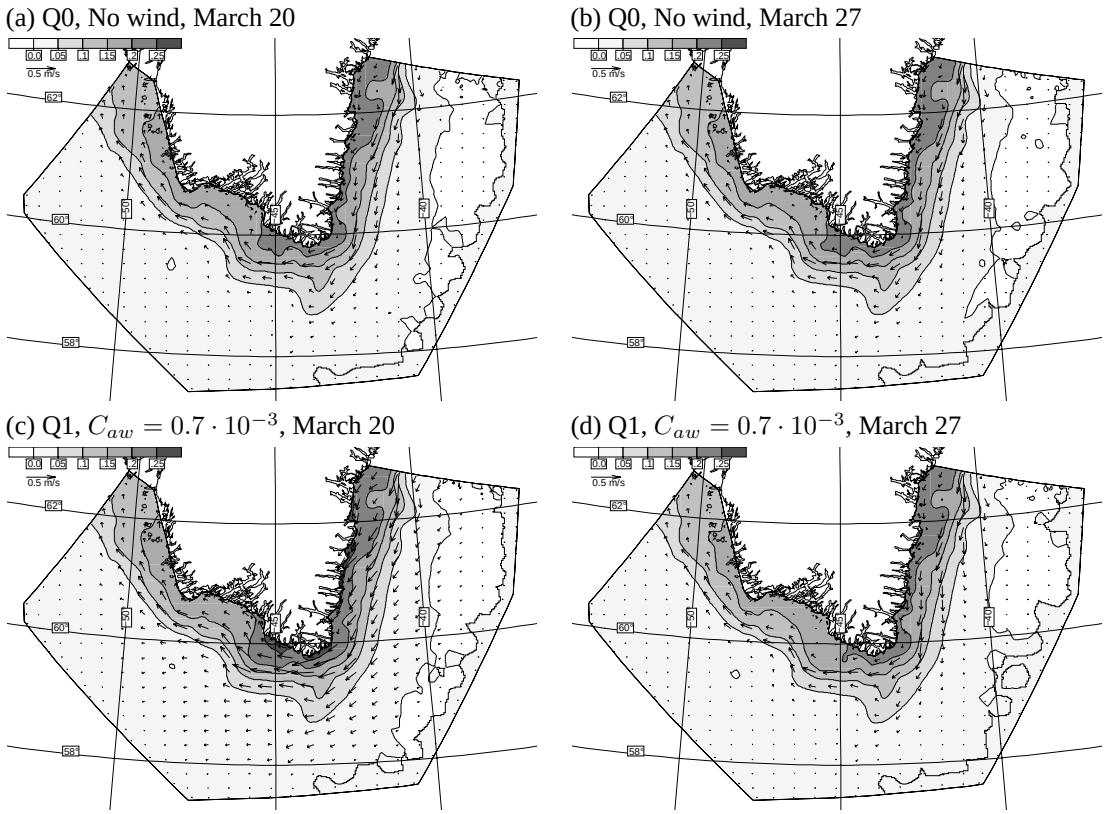


Figure 4.5: Sea surface current and elevation at March 20 and 27, non-linear prognostic simulations.

The simulations described above are barotropic, with salinity and temperature set to constant values. The baroclinic simulations were not stable, and the planned simulations are therefore not shown. Simulations including density calculations are therefore limited to a test of the cpu usage of the equation of state. The climatological salinity and temperature fields are read into the model, and evolving with time. The density is calculated, but the horizontal pressure gradient is barotropic calculated by the tilt of the sea surface. The simulations are performed for a 3 days period and are timed with the program gprof.

### 4.6.2 Results

The elevation and velocity fields of the simulations Q0 and Q1 after 3 days and 10 days are shown in figure 4.5. Both simulations are initialised with F0 (figure 4.2a).

In Q0 no wind forcing is applied, and the simulation is basically just a spin-up from the linear solution used as initial condition. In F0 the flow is highly topographically steered, and every little feature in the bathymetry is reproduced in the elevation field. This is smoothed a little in Q0 due to non-linear effects. After 3 days the state has changed slightly, the largest changes being most evident in the elevation field. A new state of equilibrium is reached at day 3, with only very small changes during the next 7 days. This becomes clearer in figure 4.6, showing surface current at a position about 50 km south of Cape Farewell. Small variations of the current are seen for the first

3 days, while no changes occur during the rest of the period.

Q1 is forced by the wind. Strong northeasterly winds in the first part of the period give an increased coastal set-up after 3 days, and the surface current is strengthened and turned towards the coast (see figure 4.5c). Near the end of the period the wind turns towards the east and the coastal set-up and strong surface current decrease. At March 27 the Q0 and Q1 elevation and current fields are very similar. Figure 4.6 shows the large variations of the current south of Cape Farewell within Q1. It starts at 0.21 m/s given by F0 having two peaks; one after 3 days (0.37 m/s), and again after 6 days (0.46 m/s).

### 4.6.3 Conjugate gradient method

The effect of the preconditioner and the stopping criterion for the iteration in the conjugate gradient method is tested through a series of experiments for the first 3 days of the simulation period. As a reference solution, a similar simulation using the LU method is performed.

The simulations are summarised in table 4.4 showing the upper bound $\epsilon$ of the residual, the cpu time and number of iterations used by the conjugate gradient method, the total cpu time and the root mean square (rms) of the error of the elevation field after 3 days. The error is defined as the difference of elevation calculated with the conjugate gradient method and the reference solution calculated with the LU method. The rms error is calculated as an integration over the total domain

$$\mathrm{rms} = \sqrt{\frac{\int (\zeta - \zeta_{lu})^2 da}{\int da}} \tag{4.23}$$

In the elemental way this is a summation weighted with the area, $a_e$, of the e'th element

$$\mathrm{rms} = \sqrt{\frac{\sum_e \sum_{i=1}^{3} \frac{1}{3} a_e (\zeta - \zeta_{lu})^2}{\sum_e a_e}} \tag{4.24}$$

where $\sum_e$ is a sum over all elements and $\sum_{i=1}^{3}$ is a sum over the three local basis functions in an element. The rms error is given relative to the standard deviation of the reference solution, $\sqrt{\int \zeta_{lu}^2 da / \int da}$.

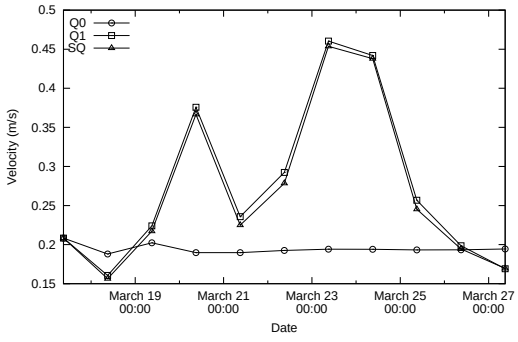


Figure 4.6: Velocity about 50 km south of Cape Farewell (position marked on figure 3.2). The model results are saved every 24 hours (marked on the curves). SQ is the coupled ice-ocean simulation described in section 5.6.1.

| Method | $\epsilon$ | no. of iterations | cpu solver (s) | cpu total (s) | rms error (%) |
|---|---|---|---|---|---|
| PCGM | $10^{-1}$ | $1-1$ | 21.35 | 1537.28 | 84.24 |
| PCGM | $10^{-2}$ | $1-2$ | 27.59 | 1544.34 | 76.34 |
| PCGM | $10^{-3}$ | $3-4$ | 36.19 | 1551.78 | 19.72 |
| PCGM | $10^{-4}$ | $4-5$ | 42.78 | 1561.48 | 2.99 |
| PCGM | $10^{-5}$ | $5-6$ | 55.43 | 1563.99 | 2.98 |
| PCGM | $10^{-6}$ | $6-7$ | 64.33 | 1582.55 | 3.29 |
| PCGM | $10^{-7}$ | $8-9$ | 70.14 | 1582.77 | 2.97 |
| PCGM | $10^{-8}$ | $9-10$ | 80.57 | 1591.14 | 3.27 |
| PCGM | $10^{-9}$ | $10-11$ | 90.60 | 1599.54 | 2.91 |
| PCGM | $10^{-10}$ | $11-12$ | 98.13 | 1602.29 | 3.26 |
| PCGM | $10^{-11}$ | $12-14$ | 104.43 | 1612.08 | 3.21 |
| PCGM | $10^{-12}$ | $14-15$ | 113.77 | 1620.43 | 2.99 |
| CGM | $10^{-12}$ | $61-86$ | 537.15 | 2015.33 | 3.07 |
| LU | | | 129.40 | 1644.48 | 0 |

Table 4.4: Tests of the conjugate gradient method with and without preconditioning in a 3-day simulation. The number of iterations and cpu time used by the algorithm are shown together with total cpu time of the simulation and the rms error of the elevation field after 3 days. $\epsilon$ specifies the stopping criterion (see eq. 4.16).

With the preconditioned method the number of iterations is seen to depend logarithmicly on $\epsilon$ ($\mathrm{no.\,iterations} \simeq -\log\epsilon$). The cpu time is mainly spent by the matrix-vector product in the algorithm ($A\vec{p}$ in eq. 4.11). This is performed once every iteration and the cpu time depends linearly on the number of iterations. None of the simulations are especially demanding compared to the total execution time, less than 10% for the best accuracy, and $\epsilon = 10^{-12}$ is used in the simulations of the total 10-day period shown in the following.

The effect of the preconditioner is clearly seen. The conjugate gradient method uses about 5 times as many iterations without preconditioning as with, and the execution time is correspondingly higher.

The simulation using the LU method is also tabulated to compare the cpu time used by the two methods. Since the LU decomposition is just performed once, it is not relevant in the comparison of time usage, and only the cpu time used by the back substitution is listed in the table. It is found that with respect to cpu time, little is gained by using the conjugate gradient method. It should be noted that a relatively small number of nodes is used in this study. Simulations on a larger mesh[3] have indicated that the difference of cpu time between the LU method and the preconditioned conjugate gradient method becomes more pronounced with increasing number of nodes, in favour of the latter method. In addition, the LU method depends on the bandwidth of $A$ (eq. 4.10), while the conjugate gradient method is independent of the node number ordering. Therefore, the complexity of the domain, for example the number of islands and narrow straits, may also play a role on the time usage for the LU method, but not for the conjugate gradient method.

[3]The testcase known by Quoddy users as G2S_M2 having 6756 nodes.

| Equation of state | Equations | Optimisation | cpu (s) |
|---|---|---|---|
| $\rho(S,\theta,0)$ | 4.17 | No | 74.37 |
| $\rho(S,\theta,0)$ | 4.18 | No | 60.76 |
| $\rho(S,\theta,0)$ | 4.17 | Yes | 19.70 |
| $\rho(S,\theta,0)$ | 4.18 | Yes | 18.77 |
| $\rho(S,\theta,p)$ | 4.18,4.19 | Yes | 61.02 |
| $\rho(S,\theta,p)$ | 4.18,4.20,4.21 | Yes | 42.94 |

Table 4.5: Tests of the different algorithms for the equation of state, showing the cpu time used by the equation of state in a 3 days simulation.

### 4.6.4 Equation of state

To test the work load of the different algorithms of the equation of state a series of simulations are performed for a 3-day period. The cpu time used by the algorithms solving the equation of state are shown in table 4.5. Without any optimisation eq. 4.18 uses 60 s and is quicker than eq. 4.17 using 74 s, although the benefit is not a doubling of the speed as suggested above. Full compiler optimisation gives a remarkable speed-up of the algorithms, both using about 19 s. The conclusion is, therefore, that with optimisation by the compiler, the two algorithms perform equally and there is no need to actually change the algorithm in the model. On the other hand there is no reason not to use eq. 4.18 instead of eq. 4.17 in new implementations.

The two different algorithms of the pressure-dependent equation of state are compiled with full optimisation. The international standard (eqs. 4.18 and 4.19) uses 61 s, almost three times as much as just the one atmosphere equation. The alternative algorithm (eqs. 4.18, 4.20 and 4.21) is quicker using 42 s, though this is still more than a doubling of the time used by the one atmosphere equation. Thus for reasons of efficiency the one atmosphere equation of state (eq. 4.17 or 4.18) should be used in coastal areas with small depth. If the depth increases, the pressure dependency on the density should be taken into account. For this purpose the algorithm proposed by Mellor (1991) (eqs. 4.18, 4.20 and 4.21) is more efficient than the international standard (eqs. 4.18 and 4.19).

## 4.7 Future work

### 4.7.1 Wind stress

In the present implementation the ocean models are fed with the surface wind velocity (10 meter wind) and the wind stress is calculated by a quadratic drag law with a constant drag coefficient. The wind is obtained from simulations with the atmospheric model HIRLAM. In fact, the wind stress is also available from the HIRLAM simulations. There are various reasons to use the wind stress directly in the ocean model instead of surface wind. First of all, since the stress depends not only on the surface velocity but also on the stability of the atmosphere (Nielsen, 1998), this would then be taken into account. Furthermore, the amount of momentum transported from the atmosphere to the ocean would be the same in the atmospheric and the ocean simulations. This is not the case in the present implementation. It should be easy to change the model source code and set-up to use the wind stress instead of the wind velocity, and it is proposed to do so.

### 4.7.2 Baroclinic forcing

The baroclinic simulations were not stable and were performed for a short test only. The baroclinic forcing is usually expected to be important and the instability must therefore be taken seriously. The reason for the instability is not known, and has been investigated only briefly. One explanation might be strange features in the bathymetry. It might have also to do with the temperature and salinity climatologies, giving rise to static instability. Other climatologies might be tried for the baroclinic forcing; there is a new global climatology (Gouretski and Jancke, 1998) that is partly based on the Levitus data, and there is one for the North Atlantic (Grey and Haines, 1999).

### 4.7.3 Comparison with laboratory experiment

In section 2.3 it was described how a laboratory experiment of the circulation in the Skagerrak is used as benchmark for a numerical model. The test case includes many important aspects of a baroclinic flow and is relevant not only for the Skagerrak, but for coastal regions in general. It might be regarded as a step beyond simple tests with known solutions.

In order to test the nonlinear finite element model, it is proposed to set it up for the laboratory experiment. The purpose should first of all be to investigate the ability of the model to simulate the circulation in a region characterised by a highly variable topography, but several numerical tests might be interesting. These could, for example, be the importance of the different resolutions, different outflow conditions etc.

### 4.7.4 Iterative method

The conjugate gradient method implemented in the prognostic ocean model is shown (section 4.5.3) to reduce the memory requirements and is therefore especially attractive for domains with a large number of nodes. The method gives only a small speed-up compared to the LU method for the domain used in this study, though it is suggested that for a larger number of nodes the conjugate gradient method is preferable. This could be investigated by measuring the cpu time on meshes with different numbers of nodes.

The conjugate gradient method requires that the involved matrix be symmetric. This is generally the case in the prognostic model, but conflicts, for example, with geostrophic boundary conditions. Since both the conjugate gradient method and the geostrophic boundary condition have valuable features it is proposed to implement other iterative methods, for example some kind of a biconjugate gradient method which would be able to solve for nonsymmetric matrices (e.g. Barrett et al., 1994). This would also be of interest for the diagnostic model. This model also solves a system of linear equations for the elevation. Here the matrix is nonsymmetric with complex elements. Since this model just solves for one step, time usage is not important, but again, the benefit with the iterative method will be in the saving of memory.

# Chapter 5

# Finite element sea ice simulations

## 5.1 Introduction to sea ice simulations

The sea ice consists of individual floes having sizes in the order of kilometres when they leave the Arctic Ocean though the Fram Strait. On their way along the east coast of Greenland they gradually break up, having sizes in the order of meters in the Cape Farewell area. On a large scale the ice is assumed to be a continuum, with state variables continuously varying (Flato, 1998; Leppäranta, 1998; Timokhov, 1998), and the ice state is described through a set of differential equations. The floe-floe interaction is parameterised through the internal stress term of the momentum equation. The parameterisation is termed the ice rheology. Sea ice models are usually distinguished by the ice rheology, while the basic equations more or less are the same for most models. See Leppäranta (1998) for a treatment of ice dynamics, Häkkinen (1990), Mellor and Häkkinen (1994) and Preller (1999) for reviews of ice and ice-ocean models, and Hibler and Flato (1992) for an overview of sea ice models in climate studies.

In a typical sea ice model the ice is assumed to be a continuum having a velocity, a thickness, and a concentration. The concentration, also referred to as the compactness, is the fraction of the area that is covered by ice. The model includes continuity equations for ice thickness and concentration, a momentum equation for the velocity, an expression that relates the ice strength (ice pressure) to the thickness characteristics, and the ice rheology for the internal ice stress. If thermodynamics are included, this enters the model through a sink/source term in the continuity equations (melting/freezing).

There are different rheologies that might be useful in the Cape Farewell area. The simplest is to set the internal ice stress to zero. This is called free drift and is probably sufficient in open water, if the ice concentration is not too high. When the concentration increases the internal ice stress becomes important, especially in areas of convergence, such as when the ice drifts towards land.

The most used rheology is the viscous-plastic proposed by Hibler (1979). This treats the ice in a plastic manner, with different behaviour in case of convergence and divergence. Flato and Hibler (1992) found the cavitating fluid rheology useful for large scale simulations and due to its simplicity and quick execution it is well suited for climate studies. Flato and Hibler (1992) extended the work to include shear stresses through the Mohr-Coulomb failure criteria. Then the ice is treated as a granular material, an ensemble of ice floes, which is a more physically realistic rheology. Tremblay and Mysak (1997) used the same rheology and give a detailed description. Another example of a floe collision rheology is that of Lu et al. (1989). It is based on collision

of disks of different sizes and used for the marginal ice zone in a meso-scale model. Hunke and Dukowicz (1997) developed an elastic-viscous-plastic rheology that uses a fully explicit time-stepping scheme. On large time scales the results using this rheology are similar to that using the viscous-plastic rheology (Hunke and Zhang, 1999).

The "Sea Ice Model Intercomparison Project" (Kreyscher et al., 1997; Lemke et al., 1997) compared different ice rheologies to determine the best ice model for climate studies. They made simulations of the Arctic with different ice rheologies for the same set-up and forcing fields and compared the results with observations on drift statistics, ice thickness in the central Arctic and ice transport through the Fram Strait. They compared the viscous-plastic, a viscous (Newtonian fluid), a cavitating fluid rheology, and an ice drift scheme with a step-function stoppage. They found the best overall result with the viscous-plastic rheology.

Rasmussen et al. (1999) performed simulations for the Greenland, Iceland and Norwegian Seas with a coupled ice-ocean model, where the ice model is that of Lu et al. (1989). They forced the model with six-hourly HIRLAM wind fields, as in this study, and with 6-hourly wind fields in a coarser resolution from the European Centre for Medium-Range Weather Forecasts (ECMWF). They found the high frequency temporal variability of the meteorological fields to be of importance for predicting the ice concentration and the position of the ice edge.

It is not always easy to verify the numerical simulations, due to lack of exact observations. Harder and Fischer (1999) made simulations of the sea ice in the Weddell Sea with a viscous-plastic model and compared simulated sea ice trajectories with observed buoy drift paths. They defined an error function based on the differences and optimised the model performance through sensitivity tests of the drag coefficients and the ice strength parameter.

Until recently numerical sea ice models were mainly used in climate studies on time scales of years and for large areas such as the entire Arctic. The models are thus developed and calibrated for the large scale simulations. In recent years the need for prognoses of the ice conditions a few days ahead has increased, mainly for ship routing and navigation purposes, and due to increasing oil exploration and production in ice-covered areas.

Yet only few forecast systems exist for ice-covered seas. Preller (1999) gives an introduction to four different forecast systems used in shallow areas. Russian forecast systems for the Arctic are used to assist ship routing along the Northern Sea Route in the coastal waters of the Russian Maritime Arctic. Seasonal as well as 1-5 day forecasts are produced. A Baltic forecast system has been developed as a joint Swedish-Finish project (see also Omstedt et al., 1994). The system produces a daily forecast of 48 hours. Besides the navigational purpose the results from the ice forecast is used in the HIRLAM system running at the Swedish Meteorological and Hydrological Institute. This has improved the atmospheric forecasts compared to the previous approach, where a climatology for the ice cover was used. A Chinese forecast system, based on the same model as that used by Sweden and Finland in the Baltic, is applied to the Bohai Sea. This is an economically very important area, containing one of Chinas major oil fields and several ports. The U.S. Navy runs a forecast system called the Polar Ice Prediction System 2.0 (PIPS 2.0) (see also Cheng and Preller, 1992; Riedlinger and Preller, 1991). It is not specifically developed for shallow seas, but the Arctic shelf areas are included in the model domain. The model is run daily to produce forecasts 5 days ahead.

Another forecast system is that used by the Canadian Ice Service[1]. It runs on a daily basis to produce forecasts of 48 hours for different limited areas. The sea ice model includes full dynamics and thermodynamics and attempts are made to couple it to POM.

[1] see http://www.cis.ec.gc.ca/model/eng

All the above mentioned modelling efforts have made use of the finite difference method. Only a few attempts to use the finite element method have been made. Thompson et al. (1988) compared different rheologies in a short-term model. They used two meshes; a stationary mesh for the momentum equation and an adaptive mesh for the advection equations. Thompson and Sykes (1990) performed sensitivity tests of the input parameters using an adjoint model. Sykes and Miller-Cushon (1992a,b) used a steady-state momentum equation together with an adjoint equation to perform sensitivity analysis of the ice motion near Adams Island. They simulated a limited area with a mesh size on the order of a few kilometres. Schulkes et al. (1998) investigated the effect of different rheologies on evolution of a large scale sea ice pack. Their model used an adaptive mesh which allowed the domain to deform under the action of external forces.

The advantages of the finite element method mentioned in section 4.1 apply for sea ice modelling as well as for ocean modelling. In the following, a dynamic finite element sea ice model is described and used for simulations of the Cape Farewell area.

## 5.2 Model description

Sea ice is treated as a continuum with a velocity field $\vec{v}$, a thickness field $h$, and a concentration field $A$. The thickness is the area mean thickness, and the actual ice thickness is equal to $h/A$ for $A \neq 0$.

The basic governing equations in the present modelling work are the same as usually seen in the literature. This includes a momentum equation and continuity equations for ice thickness and concentration. The difference compared to previous ice modelling efforts is that the spatial discretization is made by the finite element method giving a high flexibility of resolution and a relatively smooth representation of the coastline. The feasibility of the variable resolution has not really been investigated yet, but it is expected that, for instance, the ice edge or other interesting areas can be resolved in an appropriate manner.

The aim of this study is to produce sea ice simulations on a time scale of a few days up to one week and it is assumed that the thermodynamics only have a small effect. Hence, the model is a purely dynamical model (drift model) with no thermodynamics included. A few comments on the thermodynamics are given in section 5.7.6.

### 5.2.1 Spherical coordinates

To make the model suitable for large domains, it includes the ability of using latitude/longitude coordinates. This is done similar to Greenberg et al. (1998) by the transformation to curvilinear coordinates

$$\begin{aligned} dx &= R\cos(\phi)d\lambda \\ dy &= Rd\phi \end{aligned} \tag{5.1}$$

where $\lambda$ and $\phi$ denote the longitude and latitude, respectively, and $R$ is the radius of the earth. However, for simplicity the model is formulated in Cartesian coordinates in the following.

Of the simulations shown in the following, Cartesian coordinates are applied in the tests of the model (section 5.4) to keep these as simple as possible, while the simulations of the Cape Farewell area (section 5.5) are performed in spherical coordinates.

### 5.2.2 Advection-diffusion equation

The thickness and concentration fields evolve in time according to the advection-diffusion equations

$$\frac{\partial h}{\partial t} = -\nabla \cdot (\vec{v}h) + \nabla \cdot (D\nabla h) \tag{5.2}$$

and

$$\frac{\partial A}{\partial t} = -\nabla \cdot (\vec{v}A) + \nabla \cdot (D\nabla A) \tag{5.3}$$

where $D$ is a diffusion-coefficient. The diffusion is necessary to keep the solution smooth and stable as shown in section 5.4.3. Introducing a characteristic velocity scale $V$ and a length scale $\Delta l$ for the mesh, the ratio of the advection to the diffusion define the mesh Péclet number

$$Pe = \frac{V\Delta l}{D} \tag{5.4}$$

The model is run with a uniform mesh Péclet number throughout the domain and eq. 5.4 is used to calculate the diffusion coefficient for each element. $V$ is the mean speed in the element, and $\Delta l$ is the side length of the element assuming it is an equilateral triangle. Thus, the diffusion coefficient varies dependent upon the velocity and the distance between the nodes. It is noted that a high mesh Péclet number gives little diffusion and vice versa.

### 5.2.3 Momentum equation

The momentum equation includes the Coriolis force, a gravity force due to the tilt of the sea surface $\nabla\zeta$, the wind drag $\vec{\tau}_a$ on the ice, the surface current drag $\vec{\tau}_w$ on the ice, and a force $\vec{F}$ due to the divergence of the internal ice stress

$$\rho h \frac{\partial \vec{v}}{\partial t} + \rho h f \vec{k} \times \vec{v} = -g\rho h \nabla\zeta + \vec{\tau}_a + \vec{\tau}_w + \vec{F} \tag{5.5}$$

where $f$ is the Coriolis parameter, $\vec{k}$ a unit vector pointing upward and $\rho$ is the density of sea ice. The ice is a relatively thin layer with a small mass and contains only a small amount of momentum. It is assumed that the non-linear advection term influences the ice drift negligibly, and it is left out of the equation.

Since the two components of the velocity are coupled through the Coriolis term, they should preferably be solved simultaneously. This is done by a transformation of the vectors to complex numbers, such that the two components of the vector are the real and imaginary parts of the complex number. Denoting the complex number with a tilde, the velocity $\vec{v} = (u, v)$ is written as $\widetilde{v} = u + iv$, where $i$ is the imaginary unit with the property $i^2 = -1$. The $\nabla$-operator is transformed in a similar way to $\widetilde{\nabla} = \frac{\partial}{\partial x} + i\frac{\partial}{\partial y}$, and eq. 5.5 is then written

$$\rho h \left( \frac{\partial \widetilde{v}}{\partial t} + if\widetilde{v} \right) = -g\rho h \widetilde{\nabla}\zeta + \widetilde{\tau}_a + \widetilde{\tau}_w + \widetilde{F} \tag{5.6}$$

The wind and ocean current stresses are calculated using the quadratic formulations

$$\widetilde{\tau}_a = AC_{ai}\rho_a \left|\widetilde{v}_a - \widetilde{v}\right| \left(\widetilde{v}_a - \widetilde{v}\right) \tag{5.7}$$

$$\widetilde{\tau}_w = AC_{wi}\rho_w \left|\widetilde{v}_w - \widetilde{v}\right| \left(\widetilde{v}_w - \widetilde{v}\right) \tag{5.8}$$

where $C_{ai}$ and $C_{wi}$ are dimensionless air-ice and water-ice drag coefficients, $\rho_a$ and $\rho_w$ are the air and water densities, and $\widetilde{v}_a$ and $\widetilde{v}_w$ are the wind and surface current velocities.

### 5.2.4 Ice rheology

To examine the influence of the internal ice stress, simulations are carried out with free drift, with the ice as a cavitating fluid and with shear stresses included through a Newtonian fluid description.

The simplest rheology is to assume that there is no internal ice stress, i.e. $F = 0$. In this way the ice is allowed to move without interacting with the surrounding ice. One drawback with this is that in areas with convergence, it is possible that all the ice just moves to the same place piling up to a huge thickness, as shown later in section 5.4.3.

In nature there is an internal stress when the ice starts to pack. The cavitating fluid representation is the first step to model this plastic behaviour of the ice. This rheology assumes that there is no shear stress, and no internal stress in the case of divergence, but there is resistance to compression. The internal ice stress is then calculated as a pressure $P$, usually called the ice strength. As in Hibler (1979) and Flato and Hibler (1992), $P$ depends on the thickness and concentration as

$$P = P^* h e^{-C(1-A)} \tag{5.9}$$

where $P^*$ and $C$ are empirical constants.

The next step in the development of the model is to include shear stresses. Then the internal ice stress is written as a tensor and the force in the momentum equation is the divergence of the stress tensor

$$\widetilde{F} = \widetilde{\nabla}\sigma_{ij} \tag{5.10}$$

The shear is included through the relation of the ice stress to the strain rate by

$$\sigma_{ij} = 2\eta\dot{\epsilon}_{ij} + (\xi - \eta)\dot{\epsilon}_{kk}\delta_{ij} - \frac{P}{2}\delta_{ij} \tag{5.11}$$

where $\xi$ and $\eta$ are the viscosity coefficients, $\delta_{ij}$ is the Kronecker delta[2], and $\dot{\epsilon}_{ij}$ is the strain rate

$$\dot{\epsilon}_{11} = 2\frac{\partial u}{\partial x} \qquad \dot{\epsilon}_{22} = 2\frac{\partial v}{\partial y} \qquad \dot{\epsilon}_{12} = \dot{\epsilon}_{21} = \frac{\partial u}{\partial y} + \frac{\partial v}{\partial x} \tag{5.12}$$

Two rheologies including the shear stress are implemented. In the simplest the ice is treated as a viscous fluid with constant viscosity coefficient. With this, there is no difference in the forces for convergence and divergence.

A more sophisticated and often used rheology is the viscous-plastic rheology by Hibler (1979). The ice is treated as a plastic medium with limits set by the viscous state. For both the viscous and the plastic rheologies the viscosity coefficients are calculated as

$$\xi = \frac{P}{2\Delta} \tag{5.13}$$

$$\eta = \frac{\xi}{e^2} \tag{5.14}$$

where $e$ specifies the ellipticity of the yield curve. In the plastic state $\Delta$ is the strain rate invariant

$$\Delta = \sqrt{\left(\dot{\epsilon}_{11}^2 + \dot{\epsilon}_{22}^2\right)\left(1 + 1/e^2\right) + 4\dot{\epsilon}_{12}^2/e^2 + 2\dot{\epsilon}_{11}\dot{\epsilon}_{22}\left(1 - 1/e^2\right)} \tag{5.15}$$

and the viscous state is represented by a constant value, $\Delta_0$. Kreyscher et al. (1997) used the value $\Delta_0 = 10^{-7}$ s$^{-1}$ in their simulations with the viscous rheology.

[2] $\delta = 1$ if $i = j$ and $\delta = 0$ if $i \neq j$

## 5.3 Numerical scheme

The governing equations are discretized as in Quoddy, with a finite difference time stepping and the finite element method for the spatial (horizontal) variations.

### 5.3.1 Time stepping

A two-level scheme is used for both the momentum equation and the continuity equations. Due to reasons of stability it is necessary to apply an implicit scheme for the momentum equation, while it is sufficient to use an explicit scheme for the advection and diffusion [*Paul Budgell*, personal communication]. With all values known at time step $n$ the model first updates thickness and concentration for the next time step $n+1$ by

$$\frac{h^{n+1}-h^n}{\Delta t} = -\nabla\cdot(\bar{v}^n h^n) + \nabla\cdot(D\nabla h^n) \tag{5.16}$$

and similarly for the concentration. Then the velocities are updated with the terms centred at time level $n+\theta$ where $\theta \in [0;1]$

$$\rho h^{n+\theta}\left(\frac{\widetilde{v}^{n+1}-\widetilde{v}^n}{\Delta t} + if(\theta\widetilde{v}^{n+1}+(1-\theta)\widetilde{v}^n)\right) = -g\rho h^{n+\theta}\widetilde{\nabla}\zeta + \widetilde{\tau}_a + \widetilde{\tau}_w + \widetilde{F} \tag{5.17}$$

The values at time $n+\theta$ are found as a weighted average of values at time step $n+1$ and $n$, $h^{n+\theta} = \theta h^{n+1} + (1-\theta)h^n$. With $\theta = 0$ the scheme is explicit, while the other extreme $\theta = 1$ gives a fully implicit scheme. In this study the simulations are performed with $\theta = 1/2$.

The ocean stress is calculated as

$$\widetilde{\tau}_w = AC_{wi}\rho_w\,|\widetilde{v}_w - \widetilde{v}^n|\left(\widetilde{v}_w - (\theta\widetilde{v}^{n+1}+(1-\theta)\widetilde{v}^n)\right) \tag{5.18}$$

and likewise the wind stress. The reason not to centre the ice velocity at time $n+\theta$ in the absolute value of the difference of water and ice velocity is to keep the equation linear with respect to $\widetilde{v}^{n+1}$. It is found that due to stability reasons it is necessary to make the term semi-implicit by employing $\widetilde{v}^{n+1}$ in the last parenthesis.

The viscous and plastic ice stresses need to be implemented in implicit form [*Paul Budgell*, personal communication]. Since this complicates the model substantially, this is left for future work (see the discussion in section 5.7.4). The implementation and execution of an explicit version is relatively straight-forward and has been made for reasons of comparison. Then the strain rates are calculated explicitly based on the velocities at time level $n$.

A semi-implicit scheme for the advection was tested using $\frac{1}{2}(h^{n+1}+h^n)$ instead of $h^n$ on the right hand side of the continuity equation giving

$$\frac{h^{n+1}-h^n}{\Delta t} = \frac{1}{2}\nabla\cdot\left(\bar{v}^n\left(h^{n+1}+h^n\right)\right) + \frac{1}{2}\nabla\cdot\left(D\nabla\left(h^{n+1}+h^n\right)\right) \tag{5.19}$$

With finite differences this usually results in a substantial increase in the cpu time for one time step going from an explicit to an implicit scheme, since the implicit scheme involves a system of linear equations to be solved, while the solution is directly calculated with the explicit scheme. With the finite elements the explicit scheme itself involves a system of linear equations as discussed in the following section. But, while the matrix appearing in the linear system of equations is time-invariant with the explicit scheme, it is time dependent in the implicit scheme, because $h^{n+1}$

enters the right hand side of the advection equation, resulting in terms of $h^{n+1}$ multiplied by the time varying $\vec{v}$. Therefore the matrix is built only once with the explicit scheme, but has to be rebuilt in every time step with the implicit scheme. This creates two disadvantages of the implicit compared with the explicit scheme. First of all, it takes some cpu time to build the matrix every time step resulting in a slower execution, and secondly, the time-varying matrix makes it practically impossible to use other than iterative solvers, as for example, the conjugate gradient method discussed in section 4.5.3. In this sense, the explicit method is more general, since besides the iterative solution procedure it is possible to obtain the direct solution with the LU method. In the explicit case the LU decomposition is made only once, and just the back substitution is made every time step. However, only the preconditioned conjugate gradient method is implemented in the model due to the advantages of this method compared with the LU method.

### 5.3.2 Horizontal discretization

To be able to couple the sea ice model to the prognostic ocean model a horizontal discretization similar to that model is chosen. The finite element mesh consist of a number of triangles (see figure 3.3) with linear basis functions $\phi_i$. There are $N$ basis functions, where $N$ is the number of nodes in the mesh. The $i$'th basis function is defined as equal to 1 at the $i$'th node, 0 at all other nodes and varies linearly across the elements.

The weak form of the advection-diffusion equation for the ice thickness (eq. 5.2) is

$$\left\langle \frac{\partial h}{\partial t}\phi_i \right\rangle = -\left\langle \nabla\cdot(\vec{v}h)\phi_i \right\rangle + \left\langle \nabla\cdot(D\nabla h)\phi_i \right\rangle \tag{5.20}$$

Assuming no diffusive fluxes across open boundaries, that $D$ is element-wise constant, and splitting up the first term on the right hand side, gives

$$\left\langle \frac{\partial h}{\partial t}\phi_i \right\rangle = -\left\langle \left(\vec{v}\cdot\nabla h + h\nabla\cdot\vec{v}\right)\phi_i + D\nabla h\cdot\nabla\phi_i \right\rangle \tag{5.21}$$

The variables $h$ and $\vec{v}$ are expanded in the basis functions

$$h(x,y,t) = \sum_{j=1}^{N} h_j(t)\phi_j(x,y) \qquad \vec{v}(x,y,t) = \sum_{k=1}^{N} \vec{v}_k(t)\phi_k(x,y) \tag{5.22}$$

and inserting into eq. 5.21

$$\sum_{j=1}^{N} \frac{\partial h_j}{\partial t}\left\langle \phi_i\phi_j \right\rangle = -\sum_{j=1}^{N}\sum_{k=1}^{N}\left[h_j\vec{v}_k\cdot\left(\left\langle \phi_i\nabla\phi_j\phi_k \right\rangle + \left\langle \phi_i\phi_j\nabla\phi_k \right\rangle\right) + \left\langle D\nabla\phi_i\cdot\nabla\phi_j \right\rangle\right] \tag{5.23}$$

The weak form of the momentum equation (eq. 5.6) is

$$\left\langle \rho h\left(\frac{\partial \widetilde{v}}{\partial t} + if\widetilde{v}\right)\phi_i \right\rangle = \left\langle \left(-g\rho h\widetilde{\nabla}\zeta + \widetilde{\tau}_w + \widetilde{\tau}_a + \widetilde{F}\right)\phi_i \right\rangle \tag{5.24}$$

Nodal quadrature gives

$$\rho h_i\left(\frac{\partial \widetilde{v}_i}{\partial t} + if\widetilde{v}_i\right)\left\langle \phi_i\phi_i \right\rangle = -g\rho h_i\sum_{j=1}^{N}\zeta_j\left\langle \phi_i\widetilde{\nabla}\phi_j \right\rangle + \widetilde{\tau}_{w_i} + \widetilde{\tau}_{a_i} + \widetilde{F}_i \tag{5.25}$$

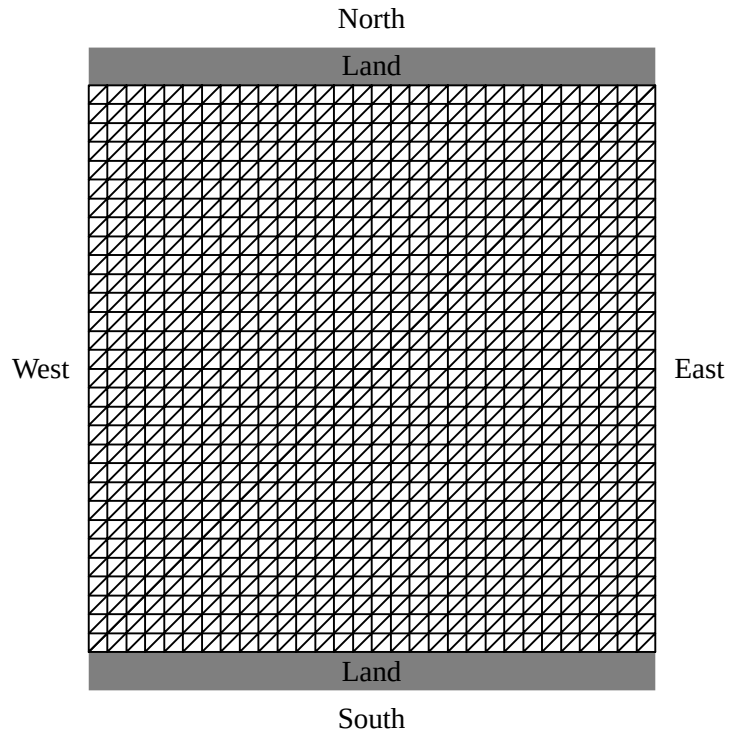


Figure 5.1: Mesh for the simple tests. There are 961 nodes and 1800 elements.

The ocean stress is calculated node-wise as

$$\widetilde{\tau}_{w_i} = A_i C_{wi} \rho_w \left|\widetilde{v}_{w_i} - \widetilde{v}_i\right| \left(\widetilde{v}_{w_i} - \widetilde{v}_i\right) \left\langle \phi_i \phi_i \right\rangle \tag{5.26}$$

and likewise the wind stress. It is noted that index $i$ in $C_{wi}$ stands for ice, but the other $i$'th stand for for the $i$'th basis function. With the cavitating fluid rheology the internal ice stress is simply the divergence of the ice strength

$$\widetilde{F}_i = \sum_{j=1}^{N} P_j \left\langle \phi_i \widetilde{\nabla} \phi_j \right\rangle \tag{5.27}$$

## 5.4 Simple tests

### 5.4.1 Set-up

The tests are carried out on a square with 961 nodes, arranged on a regular grid with 31 times 31 nodes, see figure 5.1. The grid size is 5 km. The northern and southern boundaries are land, while there are cyclic boundary conditions on the western and eastern boundaries.

### 5.4.2 Internal ice stress

The first test shows the importance of the internal ice stress when the ice is compact. The simulations are initialised with a homogeneous ice cover with a thickness of 0.5 m, a concentration of 0.5 and no velocity. There is no ocean forcing and the Coriolis parameter is set to zero. There is a

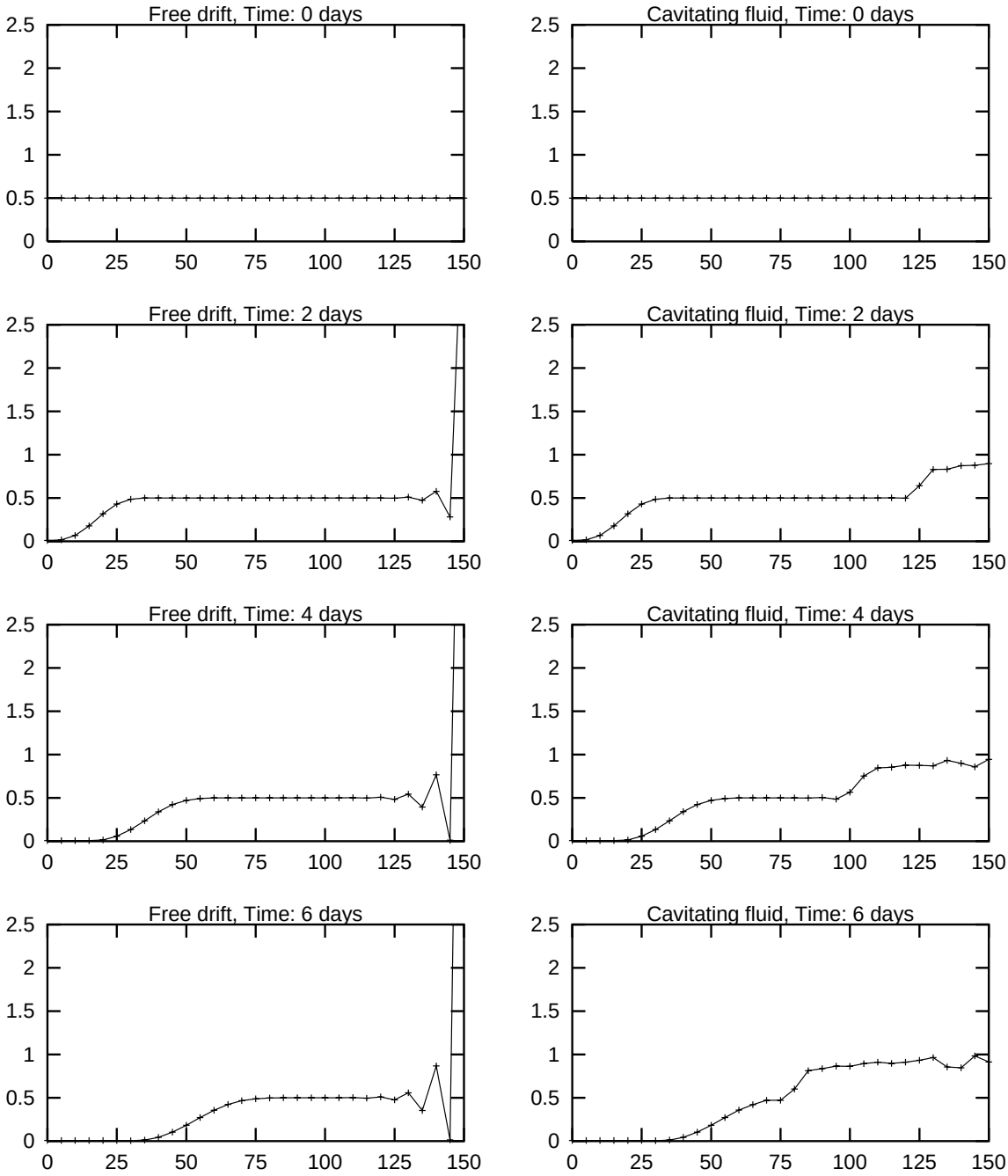


Figure 5.2: Ice thickness every second day for simulation with free drift (left column) and cavitating fluid (right column). x-axis is distance in kilometres from southern coast, and y-axis is thickness in meters.

constant southerly wind of 5 m/s giving a drift of the ice toward north, and there is thus divergence at the southern coast with the off-shore wind and convergence at the northern coast with the on-shore wind. The results are displayed in figure 5.2, showing ice thickness along a central section from south to north. The simulation period is 6 days and the results are shown every second day.

The left column in figure 5.2 shows the free drift simulation. The ice drifts away from the southern coast as expected. The thickness field does not show a sharp ice edge with an abrupt change from 0 to 0.5 meters as in the analytic solution. This is due to the diffusion term as seen in the other test discussed in section 5.4.3. On the northern coast it is found, that, except from some noise, the thickness is 0.5 m all the way to the last node, where the ice adds up to an incredible thickness of 11 m after 6 days. This is due to the lack of a resisting force when the ice starts to pack. The ice is simply allowed to move until it reaches the northern coast.

The right column shows the simulation with the ice as a cavitating fluid, i.e. with a simple formulation of an internal ice stress. The consequence is clearly seen on the northern coast. Now there exists a resistance against convergence and the thickness is 0.9 m at the coast after 6 days and decreasing away from the coast. At the southern coast the result is exactly the same as for the free drift. This is because the ice strength decreases with decreasing ice concentration and thickness, as seen from eq. 5.9.

### 5.4.3 Advection

Where the preceding test showed some of the physics of the model, this test illustrates a numerical problem that comes from the discretisation of the advection equation. This issue is not new and is described for example by Johnson (1987). It is not only present with the finite element method, but is also found with the finite difference method (e.g. Pietrzak, 1998). In the model, the advection equation is solved with the standard Galerkin method. It is of 2nd order, and the results are similar to what is found with a 2nd order centred finite difference scheme.

To focus on the problem, the momentum equation is discarded and the velocity is set constant to 0.5 m/s toward east. Initially there is a circular area in the middle of the domain with an ice thickness of 1 m in a radius of 25 km, i.e. 5 nodes, and no ice elsewhere. The analytical solution to the pure advection equation (eq. 5.2 with $D = 0$) is that the ice moves to the east without changing shape. The numerical results are shown in figure 5.3 and 5.4 as thickness at a section from west to east in the middle of the domain right through the ice covered area. The simulation period is 30 hours, and the results are shown every 10 hours.

The left column in figure 5.3 shows the results from the simulation with pure advection. The solution oscillates with over- and undershooting and even negative thickness. To get a smoother solution it is common to introduce some diffusion. This has been done in the right column by setting the mesh Péclet number to 2, with the consequence that the thickness field is smoothed too much and the sharp ice edge has disappeared. The balance is thus to add enough diffusion to filter out the oscillations, but not more than necessary. Figure 5.4 shows the results from simulations with lower diffusion coefficient (higher mesh Péclet number). It seems that the mesh Péclet number should be between 5 and 10. With $Pe = 5$ there is enough diffusion to keep the field smooth, but the sharp gradients are flatten off, while $Pe = 10$ tends not to smooth the gradient so much, but on the other hand does not give enough diffusion to remove all oscillations.

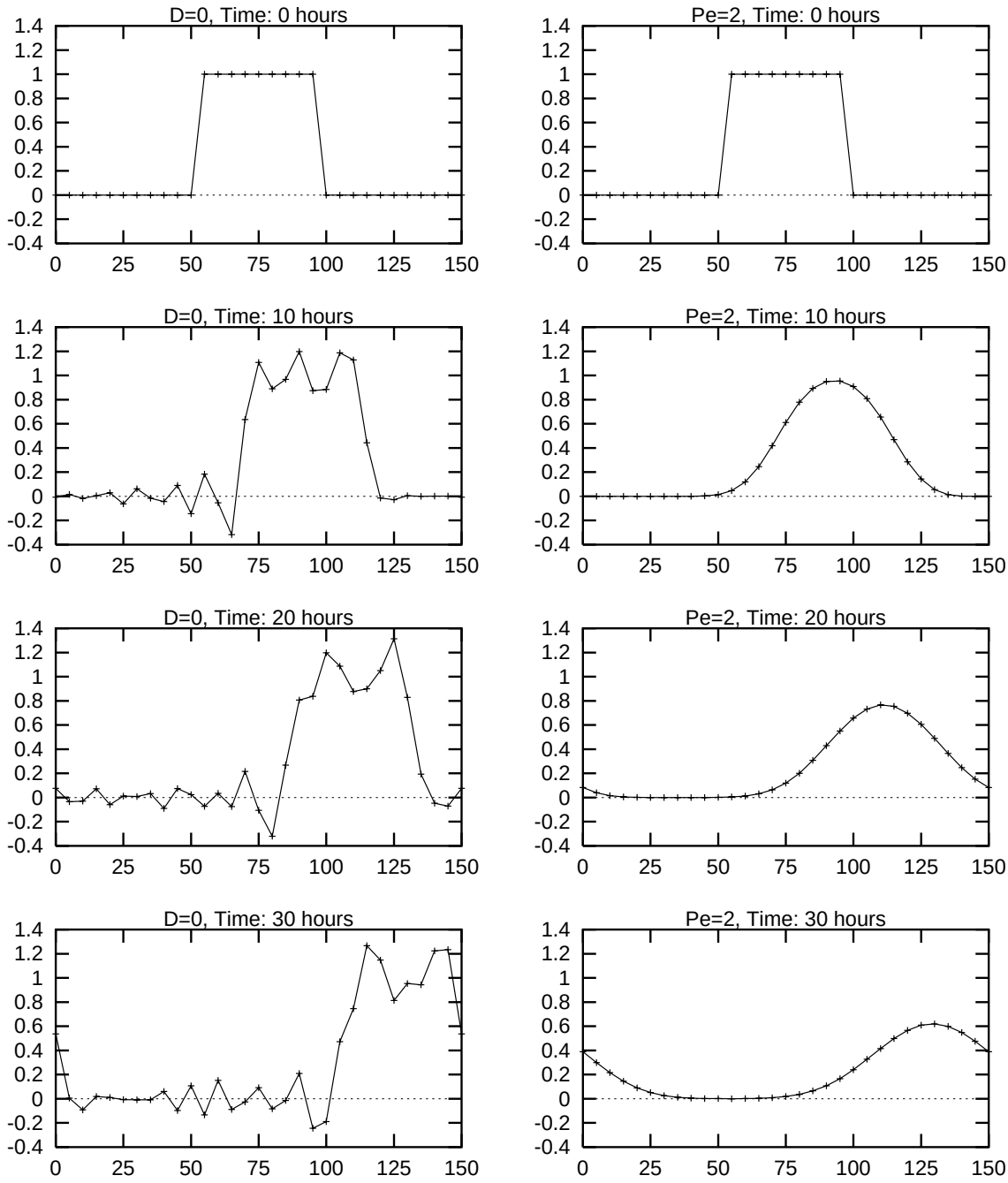


Figure 5.3: Ice thickness every 10 hours for simulation with pure advection (left column) and advection + diffusion, $Pe = 2$ (right column). x-axis is distance in kilometres from western boundary, and y-axis is thickness in meters.

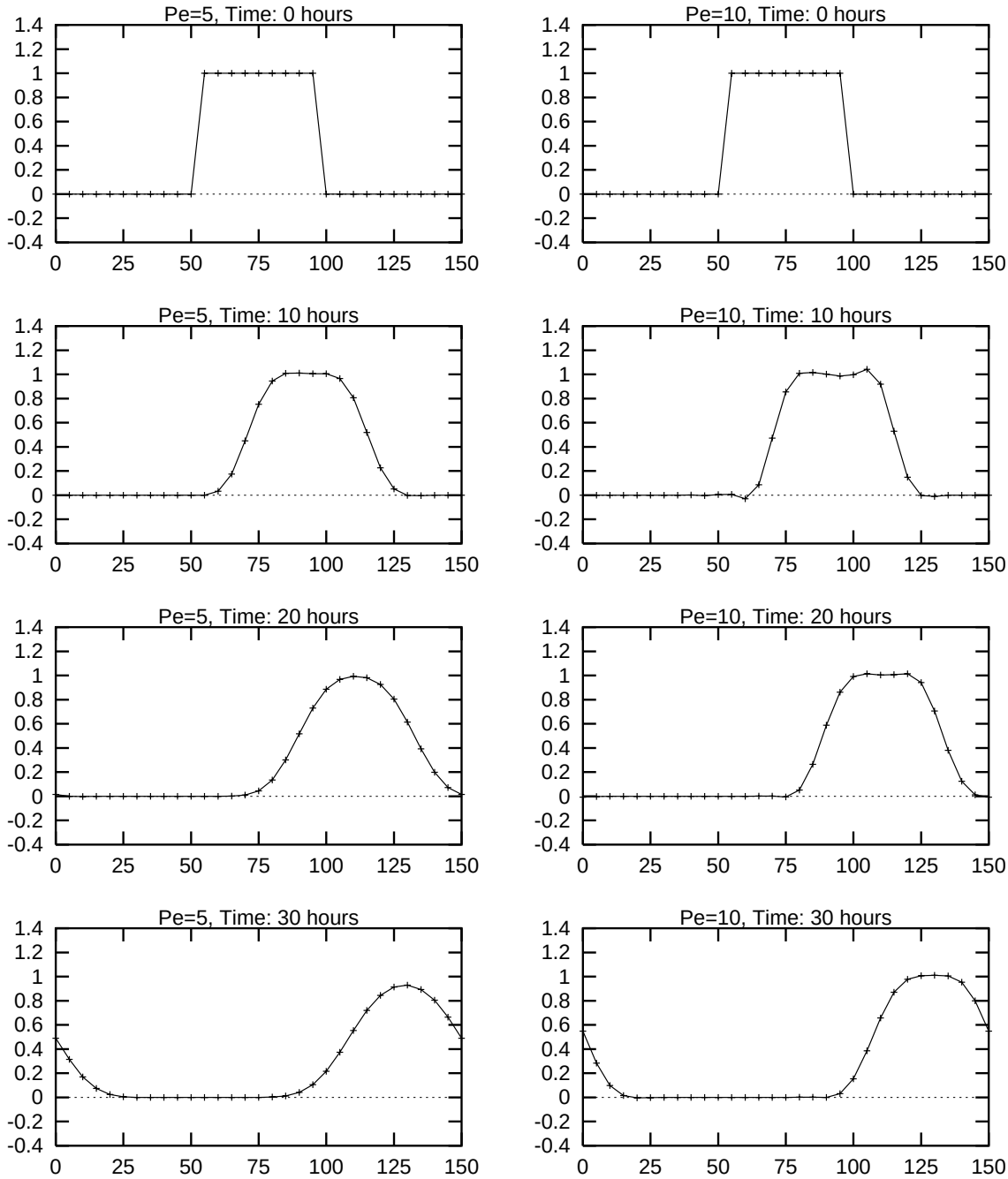


Figure 5.4: Ice thickness every 10 hours for simulation with $Pe = 5$ (left column) and $Pe = 10$ (right column). x-axis is distance in kilometres from western boundary, and y-axis is thickness in meters.

| No. | Ice rheology | $P^*$ (N m$^{-2}$) | $C_{ai}$ | $C_{wi}$ | $Pe$ | $\Delta t$ (s) | cpu (s) | rms error March 27 |
|---|---|---|---|---|---|---|---|---|
| S0 | Cavitating | $5.0 \cdot 10^3$ | $1.2 \cdot 10^{-4}$ | $1.0 \cdot 10^{-3}$ | 10 | 600 | 111.0 | 0.1180 |
| S1 | Free drift | | | | | | 106.9 | 0.1759 |
| S2 | Viscous | | | | | | 426.8 | 0.1563 |
| S3 | Viscous-Plastic | | | | | | 143.9 | 0.1990 |
| S4 | | $1.0 \cdot 10^3$ | | | | | 111.3 | 0.1319 |
| S5 | | $27.5 \cdot 10^3$ | | | | | 111.9 | 0.1217 |
| S6 | | $50.0 \cdot 10^3$ | | | | | 332.6 | 0.1637 |
| S7 | | $50.0 \cdot 10^3$ | | | | 60 | 1001.3 | 0.1365 |
| S8 | | | $1.2 \cdot 10^{-3}$ | $5.5 \cdot 10^{-3}$ | | | 113.6 | 0.1202 |
| S9 | | | $1.2 \cdot 10^{-3}$ | | | | 112.0 | 0.1965 |
| S10 | | | | $5.5 \cdot 10^{-3}$ | | | 110.9 | 0.1188 |
| S11 | | | 0 | | | | 111.8 | 0.1277 |
| S12 | | | | 0 | | | 111.8 | 0.3785 |
| S13 | | | | | 2 | | 109.5 | 0.1085 |
| S14 | | | | | 5 | | 111.1 | 0.1138 |
| S15 | | | | | 25 | | 111.5 | 0.1293 |
| S16 | | | | | | 10 | 6077.9 | 0.1174 |
| S17 | | | | | | 1200 | 61.6 | 0.1233 |

Table 5.1: Simulations performed with the sea ice model for the Cape Farewell area. Where no value is given, it as in S0.

## 5.5 Sea ice simulations

### 5.5.1 Set-up

Simulations with the sea ice model are performed for the Cape Farewell area on the same mesh (figure 3.3) and for the same period (March 17-27 1997) as used in the ocean simulations described in sections 4.3 and 4.5. A number of sea ice simulations are performed on basically the same set-up, but with different choices of parameters in order to make a simple sensitivity analysis, and to investigate the importance of the different terms. The simulations are summarised in table 5.1. The parameter values are shown in table 5.2. A comparison of the drag coefficients and the ice strength parameter with values found in the literature are shown in table 5.3. The drag coefficients are lower than usually used. A difference is to be expected, since the models described in the literature are usually calibrated for large-scale simulations of the Arctic, while the simulations presented here are performed for a limited area on a much finer scale. The drag coefficients are discussed further in section 5.5.6.

The initial ice concentration field is extracted from the ice concentration map at March 17 (figure 3.7a). The ice thickness field is not observed, and some assumptions are made for initial fields. Here the thickness in cm is set equal to the concentration in %. This does not imply any relation between the two variables, but it is seen that with this assumption the thickness is about 1 m along most of the east coast and decreases at Cape Farewell. This is in agreement with observations performed at the vessel “M/S Kista Arctica” in July 1999.

The initial velocity is calculated using a geostrophic balance between the sea surface tilt and the Coriolis force. The ice is a relatively thin layer with a small mass and only a small amount of momentum is contained in the ice. Therefore it is expected that the velocity quickly adjusts to the wind and ocean forcing and that it is sufficient to initialise with an approximation to the velocity field calculated without a priori knowledge of the wind.

| Variable | Symbol | Unit | Value |
|---|---|---|---|
| Density of ice | $\rho$ | kg m$^{-3}$ | 910.0 |
| Density of air | $\rho_a$ | kg m$^{-3}$ | 1.3 |
| Density of water | $\rho_w$ | kg m$^{-3}$ | 1025.0 |
| Air/ice drag coefficient | $C_{ai}$ | | $1.2 \cdot 10^{-4}$ |
| Water/ice drag coefficient | $C_{wi}$ | | $1.0 \cdot 10^{-3}$ |
| Ice strength parameter | $P^*$ | N m$^{-2}$ | $5.0 \cdot 10^{3}$ |
| Ice strength parameter | $C$ | | 20.0 |
| Viscous parameter | $\Delta_0$ | s$^{-1}$ | $2.5 \cdot 10^{-3}$ |
| Maximal plastic parameter | $\Delta_{max}$ | s$^{-1}$ | $4.0 \cdot 10^{-9}$ |
| Yield curve eccentricity | $\epsilon$ | | 2 |
| Weight for implicit scheme | $\theta$ | | 0.5 |
| Mesh Péclet number | $Pe$ | | $10.0$ |
| Gravitation | $g$ | m s$^{-2}$ | 9.81 |
| Earth radius | $R$ | m | $6.3675 \cdot 10^{6}$ |
| Earth rotation | $\Omega$ | s$^{-1}$ | $0.7292 \cdot 10^{-4}$ |

Table 5.2: Physical parameters and constants used in the reference simulation S0. Values in italics are varied in some simulations, see table 5.1.

A no-slip condition is applied at land boundary nodes where $\vec{v} = 0$ is specified. At the open boundaries the shear stress is set to zero, while most of the terms in the momentum actually can be calculated. The gradients of sea surface elevation and ice strength are based on the nearest interior elements. Dirichlet boundary conditions are applied to the thickness and concentration fields, using the initial values, i.e. clamped boundary conditions. This assures an inflow of ice throughout the simulation period. At outflow these boundary conditions are reflective and improper. In any case, in this study the open boundaries are sufficiently far away from the ice covered areas and the period is short enough that the ice will not reach the open outflow boundaries. The boundary conditions are therefore expected to be reasonable.

The model is forced by analysed wind fields at 6 hour intervals, and sea surface elevation and current fields at steady state. The wind fields are extracted from HIRLAM, the weather prediction

| | $C_{ai}$ $10^{-3}$ | $C_{wi}$ $10^{-3}$ | $P^*$ (kN m$^{-2}$) |
|---|---|---|---|
| Used here | 0.12 | 1.0 | 5.0 |
| Hibler (1979) | 1.2 | 5.5 | 5.0 |
| Riedlinger and Preller (1991) | 0.8 | 5.5 | 27.5 |
| Flato and Hibler (1992) | 1.2 | 5.5 | 5.0 |
| Tremblay and Mysak (1997) | 1.2 | 5.5 | 27.5 |
| Harder et al. (1998) | 2.2 | 5.5 | 7.0 |
| Harder and Fischer (1999) | 1.6 | 4.5 | 20.0 |
| Rasmussen et al. (1999) | 1.0 | 20.0 | |

Table 5.3: Drag coefficients and ice strength parameter.

model of the Danish Meteorological Institute (section 3.3.3). The sea surface elevation and current are obtained from the ocean simulation F0 (section 4.4).

The results are shown as concentration fields after 3 days and 10 days in figures 5.5-5.12. These are compared with the observed ice concentrations shown in figure 3.7. Furthermore, the rms error is calculated (see table 5.1) in order to give a more quantitative measure of the simulation results. The error is defined as the difference of the simulated and the observed concentration field, and the rms error is found by an integration over the total domain

$$\mathrm{rms} = \sqrt{\frac{\int (A_i - A_{obs})^2 da}{\int da}} \tag{5.28}$$

This is treated in elemental way as in eq. 4.24. The rms error should be regarded as an indication of how good the results are rather than an exact score of the simulation.

### 5.5.2 Cavitating Fluid

The ice concentration field in best agreement with the observations is achieved with simulation S0 using the cavitating fluid rheology and with the parameter values given in table 5.2. This simulation is therefore regarded as a reference simulation to which the other simulations are compared. The results of S0 are plotted on all the figures of the ice concentration to facilitate the comparisons. Thus the figures 5.5a, 5.7b, 5.9a, 5.11c and 5.13c are all the same, and so are 5.6a, 5.8b, 5.10a, 5.12c and 5.13d.

The simulation compares quite well with the observations. After the first 3 days the concentration field has changed little. There are still high concentrations along the east coast and a relatively sharp ice edge. Some activity has taken place on the ice edge. It is more meandering than initially and some small scale features have emerged. The sudden turn towards land seen in the observations at 61°N is, to some extent, reproduced in the simulation, although slightly more to the north. The ice cover has extended slightly further west of Cape Farewell, but the ice is not connected to land as seen in the observations.

At March 27 the ice cover along the east coast has broadened to almost the correct distance from land compared with the observations. However, this might be due to the diffusion discussed in section 5.5.7. Some of the meanders of the ice edge seen in the observations are also found in the simulation, particularly at the positions A and C marked on figure 3.7c. The ice cover west of Cape Farewell is simulated to a lower degree of accuracy, but it is still acceptable compared to the observations. The largest errors from a ship routing point of view are probably that the two ice-free areas seen in the observations, one just south of Cape Farewell and the other close to the west coast at 46°-48°W, are not reproduced by the simulation. Also the ice cover extends about 100 km too far to the west, reaching 50°W. The picture changes if areas with concentration less than 10% are disregarded in the comparison. Then the ice cover is not that far to the west, and the area with concentrations of 10-50% is off land. However, the shape of the ice cover is still not reproduced.

### 5.5.3 Free drift

The results of the free drift simulation S1 clearly show the lack of resistance to convergence in the same way as seen in the simple tests in the previous section. In the first 3 days with mainly on-shore wind on the east coast much of the ice is blown against the land (figure 5.5b) and the ice

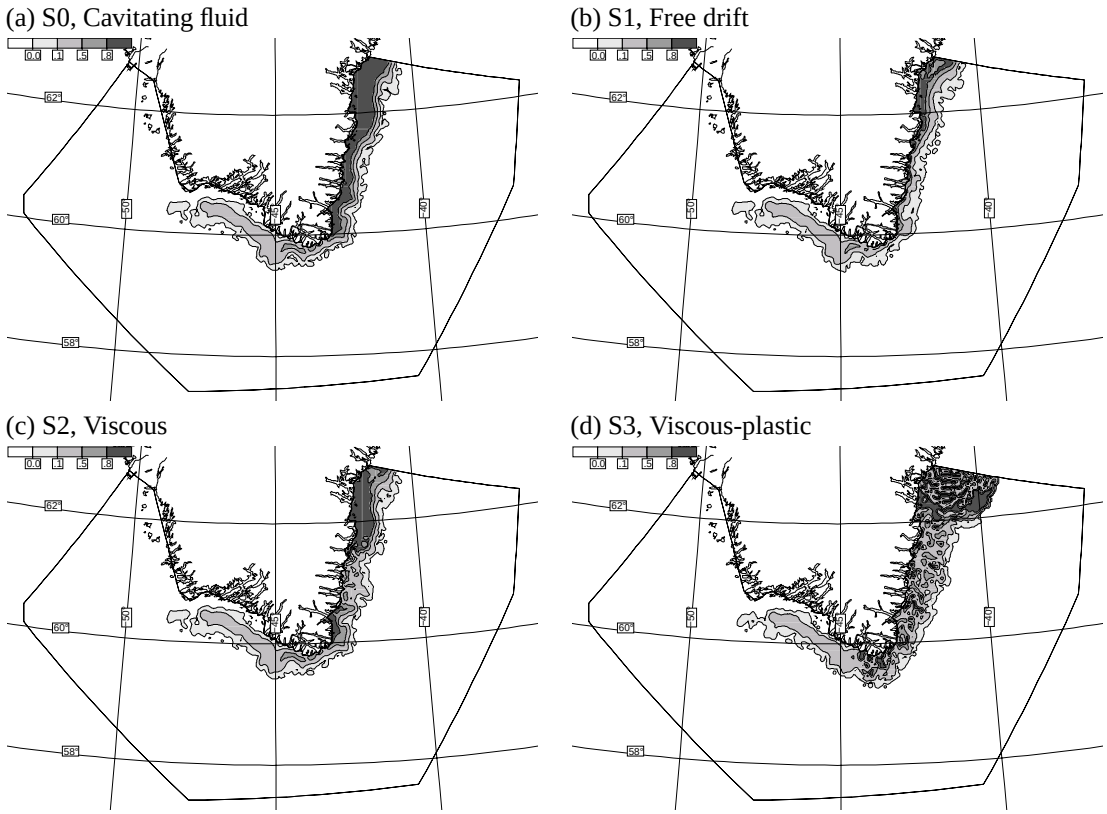


Figure 5.5: Ice concentration at March 20. Sensitivity of ice rheology. To be compared with figure 3.7b.

edge is much too close to land. The simulation never recovers from this lack of ice and at March 27 the ice concentration (figure 5.6b) is much too low along the east coast.

The concentration field west of Cape Farewell is similar to that of S0 showing that the ice is freely drifting in this area. This is probably so, because the ice is free of land, and due to the low concentrations (less than 50%) giving a relatively low ice strength and thereby small internal ice stress with the cavitating fluid rheology.

From the comparison of S0 and S1 it is concluded that the free drift simulation gives comparable results in some areas, but in general it is important with a good description of the internal ice stress. This leads to the question if the results can be improved by using more advanced ice rheologies, and motivates to try out the viscous and viscous-plastic rheologies.

### 5.5.4 Viscous and viscous-plastic fluid

Figures 5.5c,d and 5.6c,d show the results of simulations performed with the viscous and the viscous-plastic rheology respectively described by eqs. 5.10-5.14. In the plastic state the strain rate invariant $\Delta$ is calculated using eq. 5.15 and the viscous state is represented by a constant value, $\Delta_0$.

As mentioned in section 5.3.1 the implementations were made in explicit form with the strain rate calculated from the known velocities at time level $n$. The results clearly demonstrate that

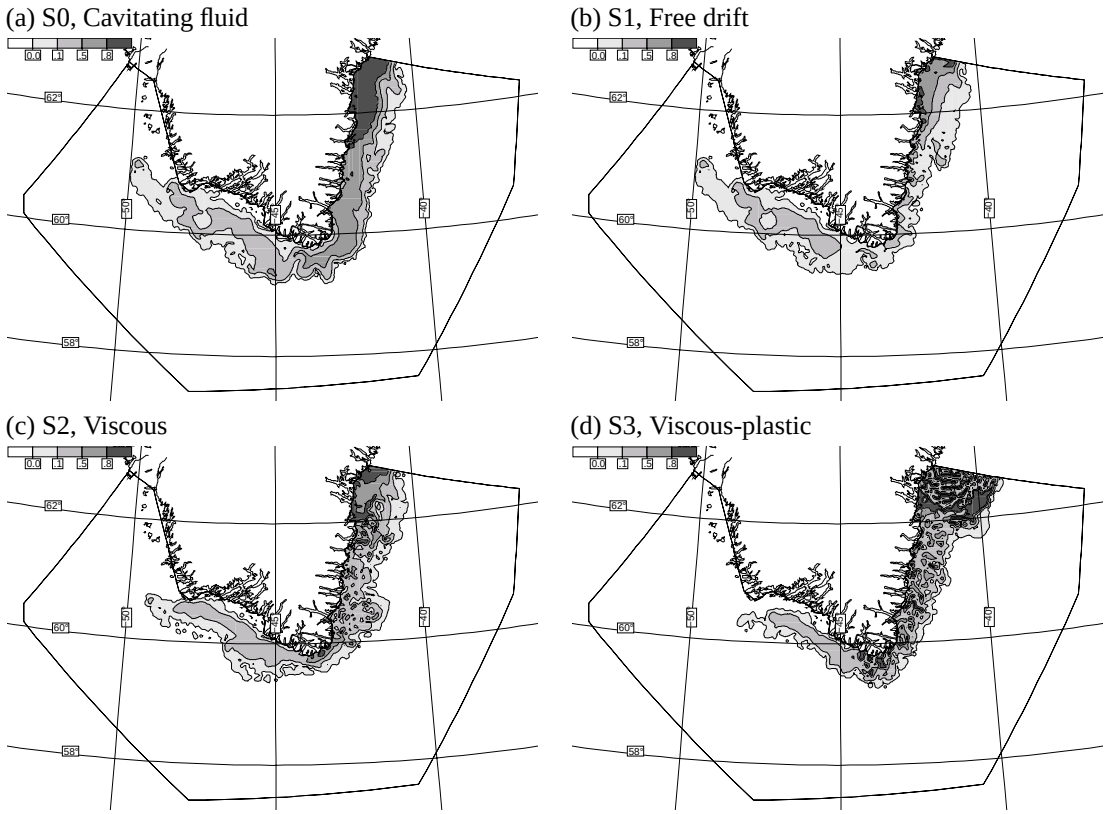


Figure 5.6: Ice concentration at March 27. Sensitivity of ice rheology. To be compared with figure 3.7c.

this is not sufficient to get a stable solution with the chosen time step. There have not been any sensitivity tests made of the time step for these two rheologies, but it is expected that to get a stable solution, the time step needs to be so small that it is not feasible to perform the simulations.

The results found with the viscous rheology are almost stable. These were obtained by adjusting $\Delta_0$ that enters the calculation of the viscosity coefficients, $\xi$ and $\eta$, in eq. 5.13 and 5.14. Kreyscher et al. (1997) used the value $\Delta_0 = 10^{-7}$ s$^{-1}$. With such a low value the viscosity coefficients become too high and the solution becomes unstable. Thus, a simple calibration of $\Delta_0$ was performed. The solution was found to be very sensitive to the value of $\Delta_0$. Here only the results from the simulation with the value $\Delta_0 = 2.5 \cdot 10^{-3}$ s$^{-1}$ are shown. If the viscosity coefficients are too low by setting $\Delta_0$ too high, the shear stresses are too low, and the result is similar to that of the cavitating fluid. When the viscosity coefficients are increased by decreasing $\Delta_0$, the solution becomes unstable.

The simulation S3 uses the values by Hibler (1979) and almost everybody else using the viscous-plastic rheology. The results are unstable and do not compare well with the observations. As mentioned above this probably has to do with the implementation of the rheology and not with the choice of parameter values. Therefore only one simulation was performed with this rheology and it is only included here to support the conclusion.

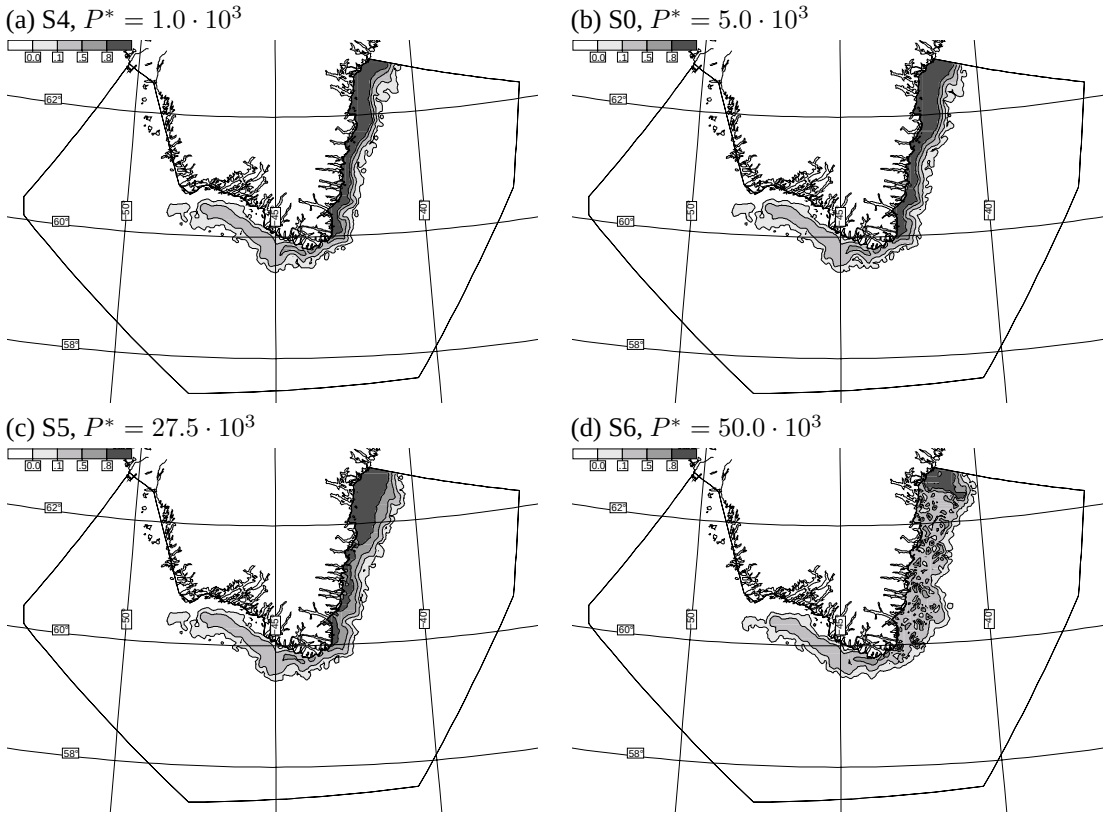


Figure 5.7: Ice concentration at March 20. Sensitivity of $P^*$. To be compared with figure 3.7b.

### 5.5.5 Sensitivity of the ice strength

The simulations S4, S0, S5 and S6 use the cavitating fluid rheology, with different values of the ice strength parameter $P^*$. A value of $27.5 \cdot 10^3$ N m$^{-2}$ (S5) was used by Flato and Hibler (1992) and Kreyscher et al. (1997), for the cavitating fluid rheology, while $5.0 \cdot 10^3$ N m$^{-2}$ (S0) was used by Hibler (1979) for the viscous-plastic rheology. The latter seems to be the standard for this rheology.

A simulation (S4) is performed with $P^*$ set to one fifth of the value of S0. The results are slightly sensitive to this reduction. After 3 days the concentration fields of S0 and S4 are indiscernible and even after 10 days the results are very similar. As $P^*$ is decreased the simulation should approach the free drift. A careful examination shows that there is slightly less ice and the ice edge is slightly closer to the east coast with S4 than with S0.

To test an increase of $P^*$ the simulation S6 is performed with $P^*$ ten times the value used in S0 and almost double of that of S5. The results are unstable with a fluctuating concentration field. This can be rectified by decreasing the time step. A simulation was performed with the same input parameters as in S6, but with the time step reduced by a factor of 10. The results (not shown) are very similar to S5. This indicates that as $P^*$ is increased above a certain value the results only change slightly, but the time step needs to be decreased to keep the solution stable.

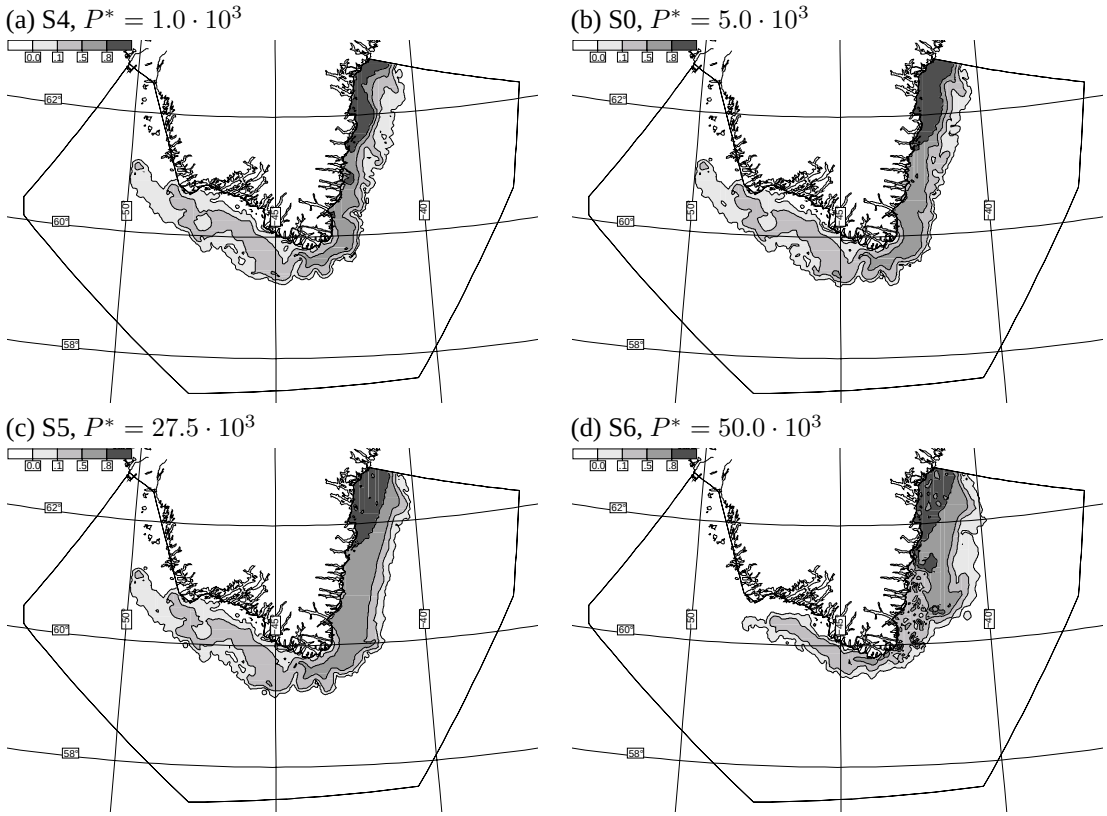


Figure 5.8: Ice concentration at March 27. Sensitivity of $P^*$. To be compared with figure 3.7c.

### 5.5.6 Sensitivity of the drag coefficients

The reference simulation S0 is performed with substantially lower drag coefficients than used by Hibler (1979) and found elsewhere in the literature, as shown in table 5.2. These values are calibrated for large-scale simulations with a climate perspective and it is therefore not surprising that other values give better results in the simulations performed here. Figures 5.9 and 5.10 show the results of simulations performed with different drag coefficients. In S8 the values by Hibler (1979) are used for both $C_{ai}$ and $C_{wi}$, while in S9 and S10 the coefficients are alternately set to the values by Hibler (1979). In S11 and S12 the coefficients are one at a time set to zero so that the wind and the ocean current are effectively switched off.

S8 with the higher drag coefficients can partly be explained by S9 and S10. During the first 3 days with relatively calm weather the difference from S0 is small. The internal ice stress is strong enough to resist the on-shore wind on the east coast, though the concentrations are slightly lower in both S8, S9 and S10 than in S0, indicating that some of the ice is drifted against the land. On the west coast there is not the same interaction of the ice with land, so that in S9, with increased $C_{ai}$, the higher wind drag has extended the ice cover further toward the west. This is not seen in S8, because the drag from the water is also increased keeping the high accelerations of the ice down. The wind drag is counteracted by the drag from the water. In S10 with the high water and low air drag coefficients the westward extent is even smaller.

During the next 7 days the wind was stronger and from changing directions and the ice is

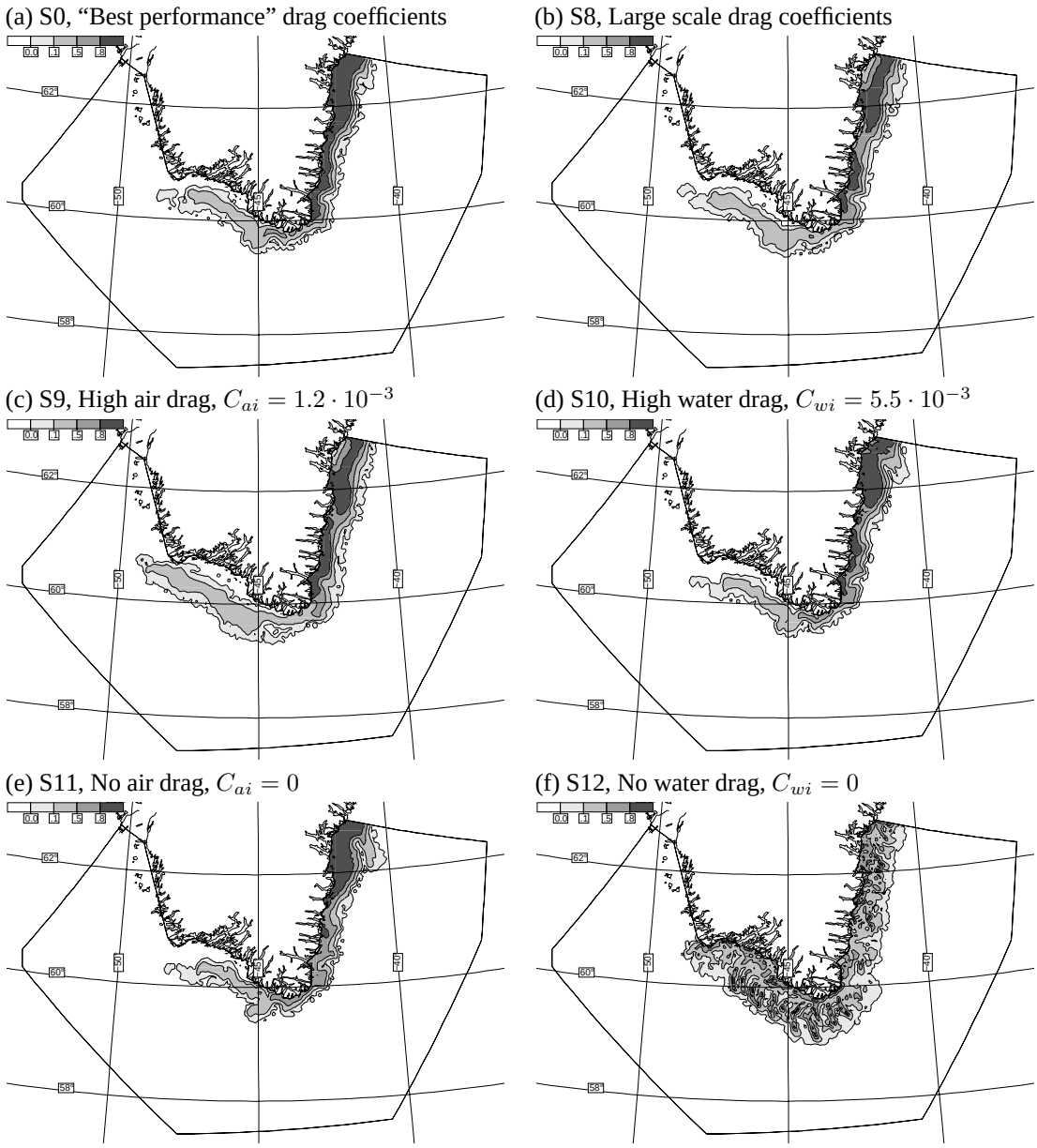


Figure 5.9: Ice concentration at March 20. Sensitivity of drag coefficients. To be compared with figure 3.7b.

(a) S0, “Best performance” drag coefficients

(b) S8, Large scale drag coefficients

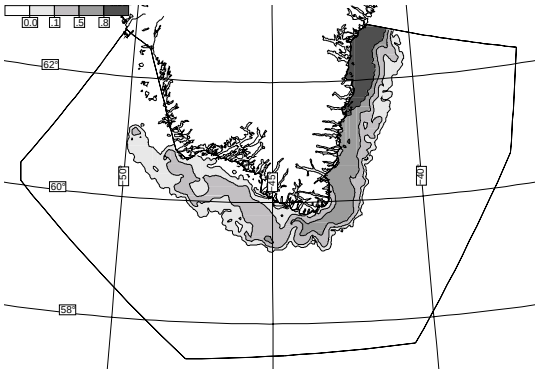


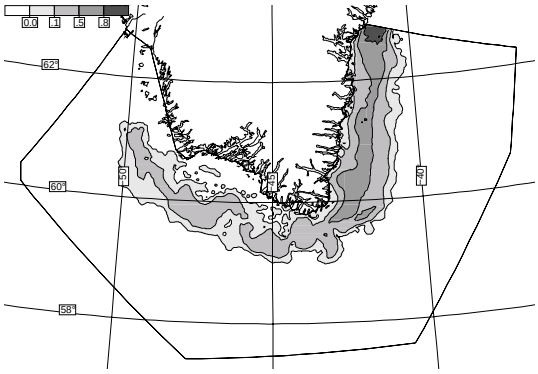


(c) S9, High air drag, $C_{ai} = 1.2 \cdot 10^{-3}$

(d) S10, High water drag, $C_{wi} = 5.5 \cdot 10^{-3}$

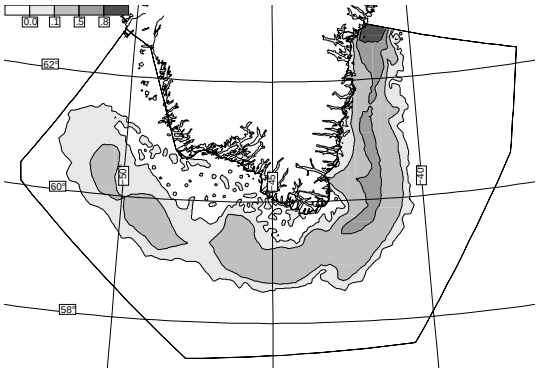


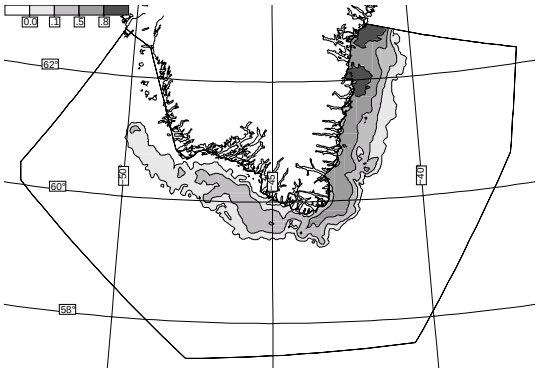


(e) S11, No air drag, $C_{ai} = 0$

(f) S12, No water drag, $C_{wi} = 0$

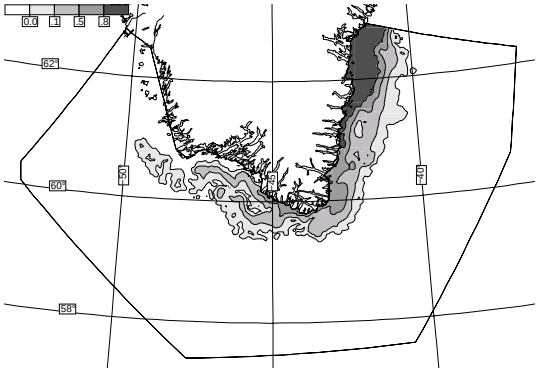


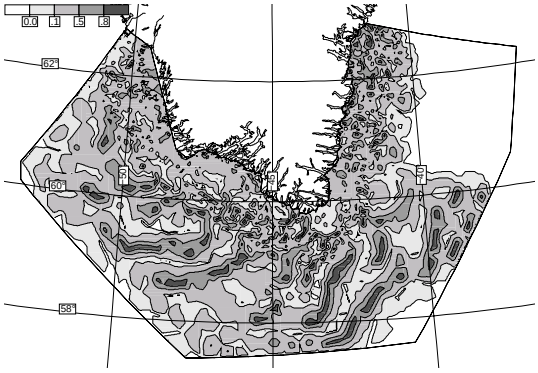


Figure 5.10: Ice concentration at March 27. Sensitivity of drag coefficients. To be compared with figure 3.7c.

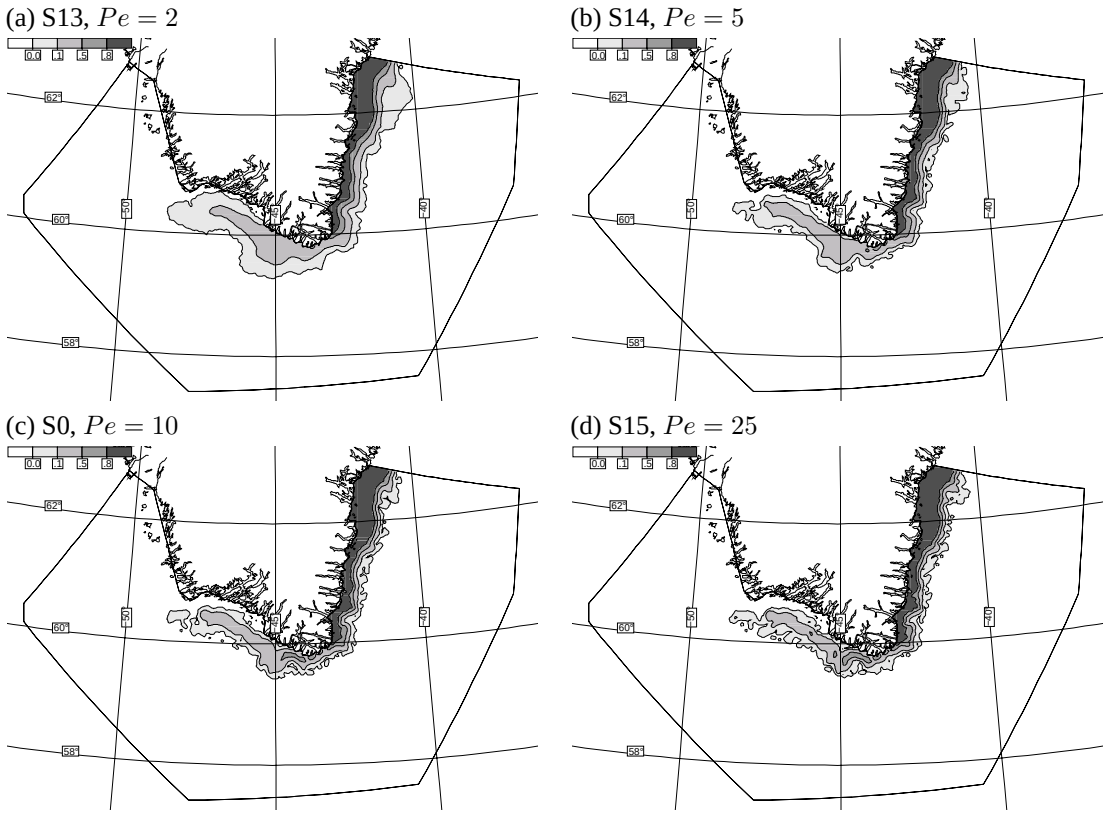


Figure 5.11: Ice concentration at March 20. Sensitivity of mesh Péclet number. To be compared with figure 3.7b.

spread over a large area in S9 with the high air drag coefficient. In particular, west of Cape Farewell the ice cover is extended, but also on the east coast the ice cover has broadened, and the position of maximum concentration is moved away from land. In S8 with high water drag as well, the extension is limited, even though the ice on the east coast is spread compared with S0 and the observations.

The results indicate that the balance between the air and water drag coefficients is very important, and that the water drag is important to hold back the ice drift. This is further demonstrated by S11 and S12.

S11 is performed with no wind forcing, $C_{ai} = 0$. The results are relatively good, with a low rms error and an ice extent comparable to the observation both after 3 and 10 days. The results after 10 days are surprisingly good, with results as good as in the simulations that includes the wind; there are several similarities between the simulated ice cover and the observations. Some of the meanders of the ice edge seen in the observations and marked A, B and C on figure 3.7c are also found in the simulation. This implies that these meanders are forced by the barotropic, steady-state ocean current field F0 (section 4.3).

As the other extreme the simulation S12 is performed with no ocean forcing on the ice, $C_{wi} = 0$. After 3 days the concentration field shows an unstable behaviour and after 10 days the ice is spread out over almost the entire domain. It is concluded that the ocean forcing is necessary to keep the ice together, while the wind more or less is a spreading factor. The wind drag is a source

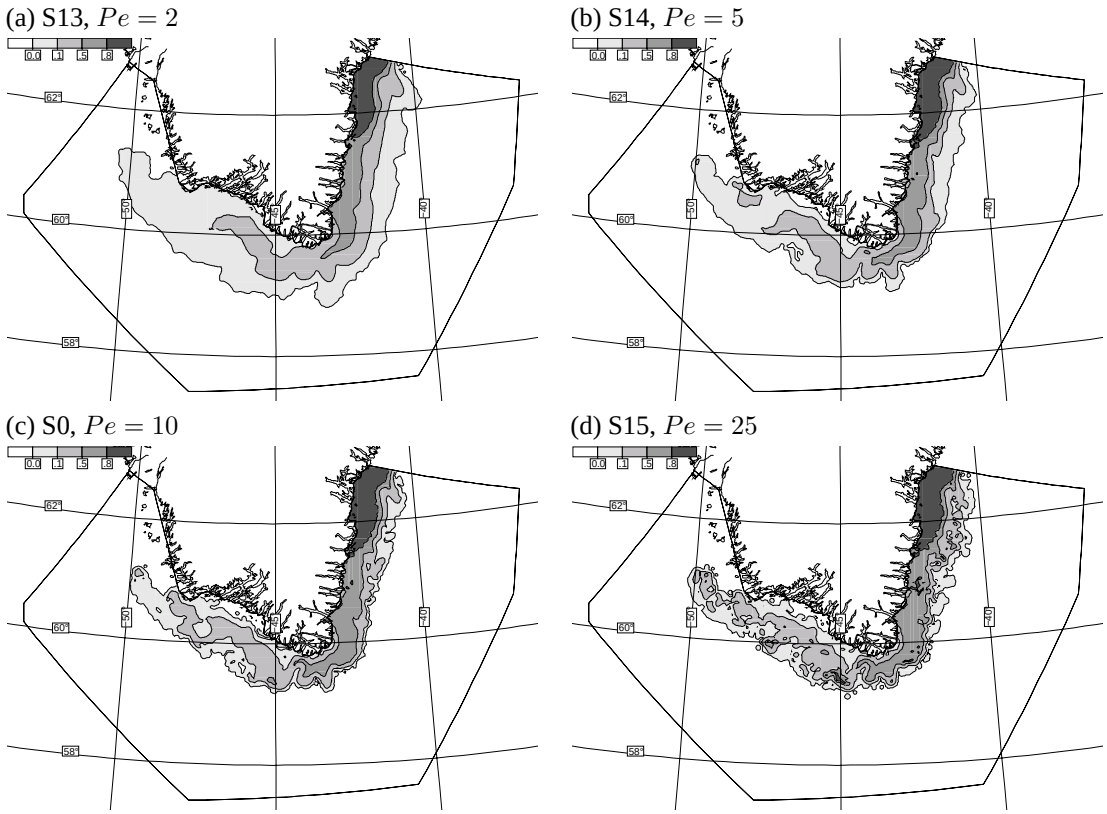


Figure 5.12: Ice concentration at March 27. Sensitivity of mesh Péclet number. To be compared with figure 3.7c.

of momentum for the ice drift, while the momentum is dissipated through the ocean. With zero ice-ocean drag there is very little to balance the input of momentum from the wind, and the ice accelerates in an unlimited fashion.

The main conclusion of comparing the observations with the simulations performed with different values of the drag coefficients is that the best result is obtained using smaller values than used by Hibler (1979). It is expected that the wind drag coefficient should be smaller than used by Hibler (1979), since he used an 8-day averaged geostrophic wind, while here is used 10 m wind analysed wind fields. The fact that the peaks of the high wind disappear in the averaging procedure justifies the use of higher drag coefficients. In addition, it is found by the comparisons that the retarding force of the water reduces the acceleration due to the wind drag. This means that the ratio of the drag coefficients are important and when the wind drag coefficient is decreased, the water drag coefficient too should be decreased. This was also found by Harder et al. (1998) who used a value of ratio of $C_{ai}/C_{wi} = 0.4$.

### 5.5.7 Sensitivity of the mesh Péclet number

Figures 5.11 and 5.12 show the results of simulations with different mesh Péclet numbers, i.e. with different diffusion coefficients. The impact of the mesh Péclet number on the solution is clearly seen. In S13 with small mesh Péclet number ($Pe = 2$) and accordingly high diffusion the solution

is smoothed substantially, and west of Cape Farewell the ice is spread over too large an area. As the mesh Péclet number is increased to 5 and 10, the ice edge along the east coast becomes sharper and more small scale features appear. In addition, the area of the ice cover west of Cape Farewell gets smaller and the concentration higher. As the mesh Péclet number is increased further, the concentration field becomes increasingly noisy, but the general results are changed only slightly. The preferred value is regarded as $Pe = 10$, even though the solution is stable for as high a mesh Péclet number as 25.

The cpu time is almost the same for all the simulations. As a small curiosity it is seen that S13 has a slightly smaller cpu time. This has probably to do with the time spent by the iterative solver used in the advection routine. When the field is smoother as in S13 the development in time is smoother and fewer iterations are needed for the solution to converge.

### 5.5.8 Sensitivity of time step

Simulations are performed with a small time step $\Delta t = 10$ s (S16) and a doubled time step $\Delta t = 1200$ s (S17). There are more small scale features, especially on the ice edge, in S16, but generally the concentration fields (not shown) are very similar to each other and to S0 as indicated by the values of the rms error, 0.1174, 0.1180 and 0.1233 for $\Delta t$ equal to 10 s, 600 s and 1200 s, respectively (see table 5.1). The cpu time scales linearly with the inverse of the size of the time step. The solution is unstable with a time step larger than about 30 minutes. Thus, to be sure to be on the right side of the stability limit a time step of 10 minutes is used for the reference simulation S0.

As described above (section 5.5.5) 10 minutes is too large a time step for the simulation S6 with a large $P^*$. In this case, the stability problems were rectified by decreasing the time step to 1 minute (S7). Thus, the instabilities found with the viscous and viscous-plastic rheologies would probably disappear by decreasing the time step. This has not been investigated, but it is expected that to stabilise these rheologies requires such a small time step that this is not feasible.

## 5.6 Coupled ice-ocean simulations

### 5.6.1 Model coupling

The sea ice simulations shown in the previous section are all performed with a steady ocean circulation. This means that the ocean does not respond to the wind and there is no feedback from the ice to the ocean. In order to capture these features, the ice model is coupled to the prognostic ocean model. This is performed through the ice-ocean stress and the sea surface tilt. In the ice model, the actual ocean surface elevation and velocity are used in the momentum equation (eq. 5.6) to calculate the surface tilt and the ocean stress (eq. 5.8). In the ocean model small changes are made in the surface stress; the ice-ocean stress is included and the wind stress is only calculated for the area of open water. The surface stress on the ocean is thus calculated as

$$\tau = (1 - A)\tau_{wind} + A\tau_{ice} \tag{5.29}$$

where $A$ is the ice concentration.

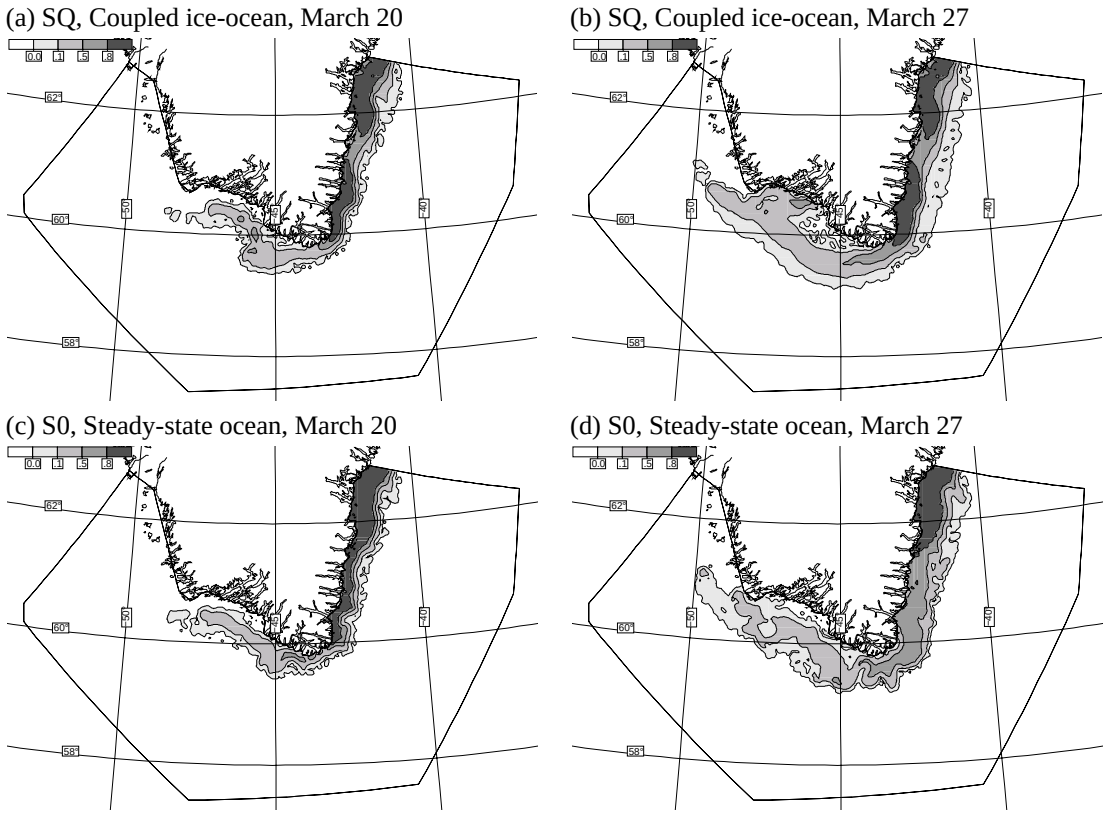


Figure 5.13: Ice concentration at March 20 and 27, coupled ice-ocean simulations and sea ice simulations forced with an ocean at steady state. To be compared with figures 3.7b,c.

### 5.6.2 Set-up

One simulation is performed with the coupled ice-ocean model. It is a mixture of S0 (see table 5.1) and Q1 (see table 4.3), such that parameters with respect to the ice model are the same as in S0 and parameters with respect to ocean model are the same as in Q1.

### 5.6.3 Results

Figures 5.13 and 5.14 show ice concentration, and sea surface elevation and current after 3 days and 10 days simulated with the coupled ice-ocean model. For comparison, the ice concentration of simulation S0 is shown on figure 5.13, as well.

The wind influences the ice drift in two ways; directly through the wind stress and indirectly

| No. | cpu (s) | rms error March 27 |
|---|---|---|
| SQ | 8948.1 | 0.1198 |

Table 5.4: Simulation performed with the coupled ice-ocean model for the Cape Farewell area. Input parameters are the same as in S0 and Q1.

through its influence on the sea surface elevation and current, which then influence the ice drift. The latter effect is not included in S0 with the steady-state ocean forcing by F0 (see table 4.1) and it was expected that the coupled model would perform better. This is confirmed in the literature and almost all references on coupled ice-ocean model emphasise the importance of the coupled system.

Nevertheless, the rms errors of S0 and SQ (table 5.1 and 5.4) indicate that the coupled model does not perform better with respect to ice concentration than the stand-alone ice model forced with ocean fields at steady state.

Figure 5.14 shows the sea surface elevation and current from SQ. Comparison with Q1 (figure 4.5c,d) shows that the ice cover has almost no influence on the ocean state. This is probably so, because the ice cover is just a narrow band along the coast and a large part of the domain is open water. This is also seen in figure 4.6. The ice damps the surface currents slightly, with the current in SQ being slightly smaller than in Q1.

The ocean is highly influenced by the wind, with increased elevation and stronger current along the coast compared to F0 (figure 4.2a) that is used as ocean forcing in S0. This is more clearly seen on figure 4.6 showing the current south of Cape Farewell. The velocity in the coupled model varies from 0.21 m/s initially up to 0.45 m/s at March 23 decreasing to 0.17 m/s at the end of the period, while the velocity at the same position within F0 is 0.21 m/s. With that background, the results of the ice concentration in S0 and SQ are surprisingly similar. This indicates that the ocean stress gives a mean drag along the coast of Greenland and transports the ice southward from the Fram Strait to the Cape Farewell area, while the wind has the main responsibility for the daily variations in the ice drift.

In this study, the same drag coefficients are used in the two simulations. Because the prognostic ocean model responds directly to the variable wind forcing, while the ocean at steady state does not, it is reasonable to expect different optimal values of the coefficients in the two cases. In the sea ice simulations with an ocean steady state, the indirect wind effect is, effectively parameterised through the drag coefficients. It is still expected that the wind effect is simulated better with the coupled ice-ocean model. It is probably more pronounced on larger time scales. However, other values of the coefficients should be used. Here the same values have been used and calibrating the

(a) SQ, Coupled ice-ocean, March 20

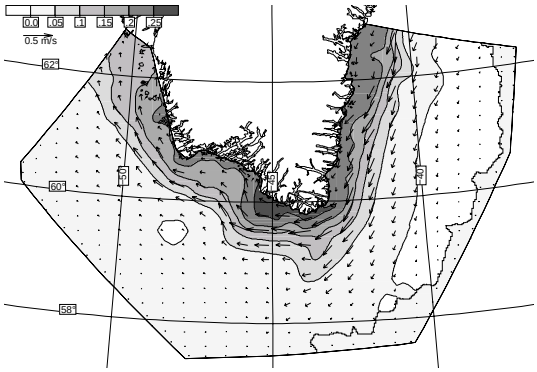


(b) SQ, Coupled ice-ocean, March 27

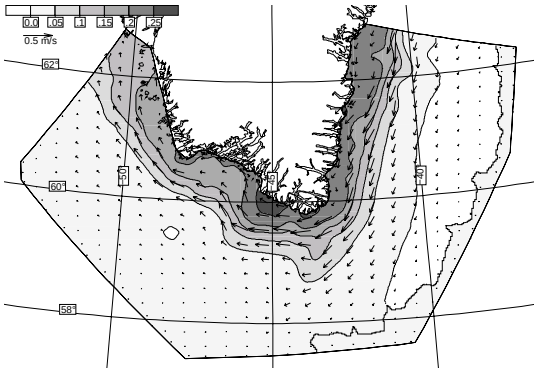


Figure 5.14: Sea surface current and elevation at March 20 and 27, coupled ice-ocean simulations.

coupled ice-ocean model is left as a topic for future work.

## 5.7 Future work

### 5.7.1 Forecast system

One of the goals of this study is to investigate the possibilities for producing sea ice forecasts for the Cape Farewell area. The simulations presented in the preceding sections show encouraging results with regard to this. The simulations also show some of the deficiencies of the sea ice model. The importance of the deficiencies depends upon the conditions that are simulated. For example, the ice rheology is more important close to land than on open water and the drag coefficients are obviously more important with strong wind than in calm weather.

In this section, a possible forecasting system is outlined. Once this is set up and running, further development of the sea ice model should be performed. In the following sections a few directions for further development are given. Some of the deficiencies of the model are discussed and possible rectifications are proposed.

A large part of the set-up for the sea ice simulations can be reused by the forecasting system. The result is not found to be better with the coupled ice-ocean model than with the ice model forced by an ocean at steady state. The latter uses much less cpu time and will therefore be used. The simulation S0 is found to have the best overall performance and the set-up and parameters of S0 will thus be used.

Maps of ice concentration are currently produced at the Danish Meteorological Institute. They are drawn manually based on remote sensed data. New observations are available every 2-3 days. These maps will be used as initial field for the forecasts. As soon as a new map is ready, it shall be digitised in a format useful for the sea ice model, and a new forecast is performed. This will be made for a 3-4 day period, i.e. not much longer than until the next ice map is ready. The procedure will be like this:

0. Receive new observations, and draw a new ice map.
1. Extract the concentration at each node in the mesh for use as initial value.
2. Extract wind fields for the period from the HIRLAM forecast.
3. Run the sea ice model to produce a new ice forecast.
4. Plot the result for presentation.
5. Save the results for later validation.

Only the first item has to be done manually. It is not really a part of the forecasting system, but is the basis for producing the forecasts. Once a new map is ready, a forecast for the next 3-4 days is produced automatically. The model is re-initialised for every new forecast and the predicted ice cover therefore does not drift away from reality.

### 5.7.2 Drag coefficients

The simulations show that the value of the air-ice drag coefficient and the relation between the air-ice drag and the water-ice drag coefficients have a large effect on the results. It is found that with the coefficient usually used for the large scale simulations of the Arctic, the results are not good.

A few simulations with different values for the coefficients have been performed. An obvious way to improve the model performance is to perform a proper calibration with respect to the drag coefficients.

### 5.7.3 Wind stress

As mentioned in section 4.7.1, the wind stress depends upon the stability of the atmosphere. The wind stress is available from the HIRLAM simulations and should be used directly instead of calculating it in the sea ice model based on the wind speed. Then the calibration of the drag coefficients suggested in the previous section is not necessary.

The issue of the wind stress is straight-forward in the case of pure ocean simulations (section 4.7.1). Since the flux of momentum leaving the atmosphere is obtained from the weather prediction model, this is simply specified on the ocean surface. Within the sea ice and coupled ice-ocean simulations the different roughness of the sea ice and the sea surface must be taken into account to divide the momentum correctly between the ice and the ocean.

Since HIRLAM uses climatological ice fields, a situation may occur where the climatology specifies open water in some areas that are ice covered in the actual sea ice simulation. In such a case the wind stress is not correct in the atmospheric simulation and a conversion is probably necessary to get the correct wind stress on the ice.

### 5.7.4 Ice rheology

As mentioned in section 5.3.1 the viscous and the viscous-plastic rheologies are implemented in explicit form. This is because the implicit form complicates the implementation, while the explicit form is easily implemented and quickly executed. However, the results of the simulations show that for stability reasons it is necessary to implement eqs. 5.11 and 5.12 in implicit form, with $u$ and $v$ centred at time level $n$. This gives a problem with the complex notation of the momentum equation (eq. 5.6) since it is not possible to formulate the internal ice stress implicitly in the complex notation, i.e. it is not possible to reduce eqs. 5.10-5.12 to something like $\widetilde{F} = \widetilde{a}\widetilde{v}^{n+1} + \widetilde{b}\widetilde{v}^{n}$ with $\widetilde{a}$ and $\widetilde{b}$ to complex factors. One way to deal with this problem is to solve for u and v separately, being implicit only for the velocity component that is solved, i.e. $F_x = f(u^n, u^{n+1}, v^n)$ and $F_y = f(u^n, v^n, v^{n+1})$. But solving for u and v separately will break the coupling through the Coriolis term, which was the argument for using the complex form of the momentum equation. In order to keep this, it is proposed to solve the momentum equation in two steps, by

$$\frac{\vec{v}^{n+1} - \vec{v}^{n}}{\Delta t} = \frac{\vec{v}^{n+1} - \vec{v}_c^{n+1}}{\Delta t} + \frac{\vec{v}_c^{n+1} - \vec{v}^{n}}{\Delta t} \tag{5.30}$$

where $\vec{v}_c$ is the solution to the complex momentum equation. First step is to find $\vec{v}_c^{n+1}$ by solving as much as possible of the momentum equation in complex notation, thus solving eq. 5.6, with $\vec{v}_c^{n+1}$ instead of $\vec{v}^{n+1}$. This gives the cavitating fluid velocity, and it is actually just what is currently done in the model. In the second step the velocity field is updated separately for $u$ and $v$ by $\rho h \frac{\vec{v}^{n+1} - \vec{v}_c^{n+1}}{\Delta t} = \nabla \cdot \sigma_{ij}$, with $\sigma_{ij}$ given by the shear as in eq. 5.11.

Once this is working, it should be relatively easy to implement a routine calculating the shear viscosity coefficients $\xi$ and $\eta$ using the Mohr-Coulomb granular rheology (Flato and Hibler, 1992; Tremblay and Mysak, 1997).

Another rheology worth studying is the Elastic-Viscous-Plastic approach of Hunke and Dukowicz (1997). It reduces to the viscous-plastic at the time scales associated with the wind forcing,

while an elastic wave equation is solved for shorter time scales (see also Hunke and Zhang, 1999). This leads to a fully explicit numerical scheme and the above mentioned awkward solution procedure is therefore not necessary. In addition, an explicit code is advantageous on vector and parallel computers.

### 5.7.5 Advection

A standard Galerkin formulation of the advection equation is used in the model. The simple test discussed in section 5.4 shows that it is necessary to include diffusion in order to get a stable and smooth solution, but this in turn smoothes the concentration and thickness fields. After the 10 days simulation period the maximum values decrease and the ice edge becomes a smooth transition from ice to water. In connection with sea ice forecasts, it is very important to predict the position of the ice edge.

There are two ways to get better results. One is simply to increase the resolution. This will make the ice edge sharper. From eq. 5.4 it is seen that for a fixed mesh Péclet number the diffusion coefficient decreases when the mesh length scale $\Delta l$ is decreased. For this model set-up, a 10 days simulation took less than 2 minutes and for a forecast length of 3-4 days, it is no problem to use a much larger number of nodes.

Another way of improving the results is to implement a more advanced advection scheme. Quoddy has problems related to the advection scheme and has difficulties preserving a sharp front [*Paul Budgell*, personal communication]. The sea ice model might be useful as a test model for more advanced advection algorithms, before they are implemented in the more complex 3 dimensional ocean model. The issue has been given no attention in this study and here only a few possible directions for further developments will be discussed.

Lagrangian methods are attractive for the advection of sea ice. Some of the methods, for example the particle methods, are suitable only for variables that are present in a part of the domain, and thus not for temperature or salinity in an ocean model. Johannessen et al. (1994) simulate ice tongues and vortex pairs in the marginal ice zone. They treat the ice as a passive tracer represented by a number of particles on top of an ocean model. The particles are advected by the surface ocean velocity, and the model does not include wind forcing and internal ice stress. This is included by Flato (1993) by a Particle-In-Cell sea ice model. There the ice is represented by a number of particles for the advection equations, while the ice momentum equation is solved on the mesh. This is an attractive method, when only a small part of the domain is covered by ice. The advantage with the method is the higher accuracy and the decreased diffusion. Furthermore, it is only necessary to calculate in the ice-covered areas and not in all the ice-free areas. The largest disadvantage of this method is related to the unstructured grid used within the finite element method, making it an expensive search procedure to determine which element a particle is moving into. This problem is treated by Giraldo (1997) who showed a significant speed-up using a tree structure of the mesh.

Thompson et al. (1988) and Schulkes et al. (1998) use an adaptive mesh for the advection equations. It is not clear, what to do if the ice cover splits into two or more areas, as is actually the case at March 27.

### 5.7.6 Thermodynamics

Thermodynamics have not been discussed yet and are not included in the model. The aim of this study is to conduct sea ice simulations for a time scale of a few days up to one week and it

is assumed that the thermodynamics would have only a small effect. However, from people who frequently sail in the waters around Greenland, it is reported that the ice occasionally disappears in one day, suggesting that the ice is melting. Thus, some thermodynamics would probably improve the results in these situations. Also, for simulations on longer time scales, for example in climate studies, the thermodynamics are supposed to be important. In order to make the model more complete it is therefore suggested to implement thermodynamics.

Freezing and melting of the ice are then included in the model as source and sink terms in eqs. 5.2 and 5.3. As the issue has been given no attention in this study, no proposals on the calculation of the sink and source terms will be given. A good starting point might be the work by Parkinson and Washington (1979) that is based on an energy balance and seems to be the standard method used elsewhere (e.g. Kreyscher et al., 1997; Makshtas, 1998).

# Appendix A

# Introduction to discrete methods

## A.1 Continuous description

Only a few ocean models use the finite element method while the finite difference method is more commonly used. Here just a very short introduction to both methods shall be given. Important aspects such as boundary conditions, requirements for stability etc. are not discussed. The reader is referred to text books for a more detailed treatment, see for example Kowalik and Murty (1993) for the finite difference method and Johnson (1987) for the finite element method.

The evolution of the ocean is described through a set of mathematical equations, usually partial differential equations. This is called the mathematical model. For example advection in one dimension with constant velocity $u$ is written as

$$\frac{\partial c}{\partial t} = -u\frac{\partial c}{\partial x} \tag{A.1}$$

where $c$ is the concentration, $t$ is time and $x$ is the space coordinate.

In reality, the concentration is a continuous field, having a value everywhere. It is not possible in general to solve the mathematical model with its infinite number of degrees of freedom. With discrete (numerical) methods the problem is reduced to a numerical model with a finite number of unknowns.

## A.2 Finite difference method

With the finite difference method the domain of interest $x \in [0; L]$ is divided into a grid with grid size $\Delta x$ (distance between two neighbouring grid points) and the concentration is calculated at the grid points only. Thus the field $c(x)$ is represented by a number of values $c_i$ where $i$ is an index of the grid point number. The differentials are approximated by differences. The spatial differential quotient centred at grid point $i$ is written

$$\frac{\partial c}{\partial x} \approx \frac{c_{i+1} - c_{i-1}}{2\Delta x} \tag{A.2}$$

The time is treated in the same manner dividing it into time steps $\Delta t$. With $n$ the index for time, the expression

$$\frac{\partial c}{\partial t} \approx \frac{c^{n+1} - c^n}{\Delta t} \tag{A.3}$$

is used in the span between time levels $n$ and $n+1$. Inserting eqs. A.2 and A.3 into eq. A.1 gives the numerical model. This is solved as an initial value problem, i.e. knowing all values at the initial time the values at the first time level are calculated, then the second and so forth.

In the explicit method all terms except the time derivative are calculated by known values. Thus the model sketched here becomes

$$\frac{c_i^{n+1} - c_i^n}{\Delta t} = -u \frac{c_{i+1}^n - c_{i-1}^n}{2\Delta x} \tag{A.4}$$

and the values at each grid point are calculated directly (explicitly) as

$$c_i^{n+1} = c_i^n - u \frac{\Delta t}{2\Delta x}(c_{i+1}^n - c_{i-1}^n) \tag{A.5}$$

In the implicit method the terms are calculated by values at the new time level

$$\frac{c_i^{n+1} - c_i^n}{\Delta t} = -u \frac{c_{i+1}^{n+1} - c_{i-1}^{n+1}}{2\Delta x} \tag{A.6}$$

This complicates the solution since $c_i^{n+1}$ can not be calculated directly, but depends on the values at the neighbour points at time level $n+1$.

$$c_i^{n+1} + u \frac{\Delta t}{2\Delta x}(c_{i+1}^{n+1} - c_{i-1}^{n+1}) = c_i^n \tag{A.7}$$

This can conveniently be written in vector notation, with the concentration as a vector $\vec{c}$ of dimension $N$, where the $i$'th element is equal to the concentration at the $i$'th point, and $N$ is the number of grid points. Then the model can be expressed as a $N \times N$ matrix $A$ where

$$A = \begin{pmatrix} 1 & u\frac{\Delta t}{2\Delta x} & 0 & 0 & \\ -u\frac{\Delta t}{2\Delta x} & 1 & u\frac{\Delta t}{2\Delta x} & 0 & \dots \\ 0 & -u\frac{\Delta t}{2\Delta x} & 1 & u\frac{\Delta t}{2\Delta x} & \\ 0 & 0 & -u\frac{\Delta t}{2\Delta x} & 1 & \\ & \vdots & & & \ddots \end{pmatrix} \tag{A.8}$$

and the implicit method involves the solution of

$$A\vec{c}^{n+1} = \vec{c}^n \tag{A.9}$$

## A.3 Finite element method

In the finite element method one starts by defining $N$ basis functions $\phi_j$, representing the variables in the basis

$$c \approx \sum_{j=1}^{N} c_j \phi_j \tag{A.10}$$

There are thus $N$ unknowns, the $c_j$'s, that must be found. Again the domain $x \in [0; L]$ is divided into a mesh[1] having $N$ nodes with the elements in between. The ocean models and the sea ice

[1] It is noted that in the finite difference method it is called a grid and points. In the finite element method it is usually called a mesh and nodes, even though it in reality is the same.

model described in Chapter 4 and 5 use the simple basis consisting of piecewise linear functions that are equal to 1 at one node, 0 at all the other nodes and varying linearly across the elements. Figure A.1 is an example of the $j$'th basis function in the 1 dimensional case. It is seen that with this basis $c_j$ is simply the value at the $j$'th node.

The time and spatial variations are split, such that the spatial variations are included in the basis functions, while the coefficients take care of the time variations

$$c(x,t) \approx \sum_{j=1}^{N} c_j(t)\phi_j(x) \tag{A.11}$$

The time and the spatial variations are thus treated independently, justified by the different nature of the problems. The time variation is an initial-value problem, while the spatial variation is a boundary-value problem. The derivatives are then approximated by

$$\frac{\partial c}{\partial x} \approx \sum_{j=1}^{N} c_j \frac{\partial \phi_j}{\partial x} \tag{A.12}$$

and

$$\frac{\partial c}{\partial t} \approx \sum_{j=1}^{N} \frac{\partial c_j}{\partial t} \phi_j \tag{A.13}$$

The expressions A.11-A.13 are only approximations, since $N$ is a finite number, and the basis is said to be incomplete. Thus by inserting into eq. A.1 the left hand side will not necessarily equal the right hand side, and there will be a residual. The equation is then solved for the coefficients $c_j$ such that the residual is as small as possible. This is performed with the method of weighted residual, where the equation is weighted (multiplied) by a function $\varphi$ and integrated over the model domain. In short notation this is written

$$\left\langle \frac{\partial c}{\partial t}\varphi \right\rangle = -\left\langle u\frac{\partial c}{\partial x}\varphi \right\rangle \tag{A.14}$$

$<>$ indicates the integration, in the 1 dimensional case simply $\int_0^L dx$. The residual is then made as small as possible with respect to the basis functions. This means that the residual is orthogonal the basis functions, so the inner product of the residual and each of the basis functions is zero.

The weighting function could be any function. When the basis functions are used as weighting functions, it is called the Galerkin method. Then

$$\left\langle \frac{\partial c}{\partial t}\phi_i \right\rangle = -\left\langle u\frac{\partial c}{\partial x}\phi_i \right\rangle \tag{A.15}$$

and must be valid for each basis function $\phi_i, i = 1, 2, ..., N$. This gives $N$ equations that can be solved for the $N$ unknown $c_j$'s.

It is recognised that the true solution to eq. A.1 also fulfils eq. A.15, though fulfilling eq. A.15 does not necessary guarantee that the true solution is found. Thus eq. A.15 is called the weak formulation of the advection equation A.1.

The expressions A.11-A.13 are inserted in the weak formulation to give

$$\sum_{j=1}^{N} \frac{\partial c_j}{\partial t} \langle \phi_i \phi_j \rangle = -u \sum_{j=1}^{N} c_j \left\langle \frac{\partial \phi_j}{\partial x}\phi_i \right\rangle \tag{A.16}$$

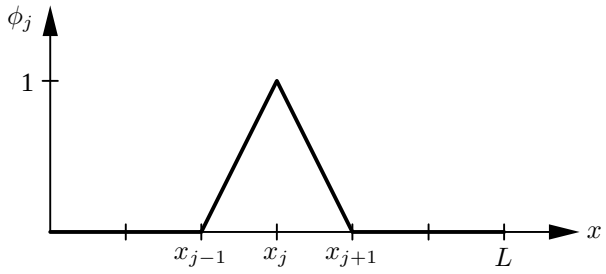


Figure A.1: Basis function $\phi_j$.

The inner product is by definition $\langle \phi_i \phi_j \rangle = \int_0^L \phi_i \phi_j dx$. Due to the shape of the basis functions the integration is easiest performed on each element. The $i$'th basis function is non-zero only on two elements $[x_{i-1}; x_i]$ and $[x_i; x_{i+1}]$, and $\langle \phi_i \phi_j \rangle = \int_{x_{i-1}}^{x_i} \phi_i \phi_j dx + \int_{x_i}^{x_{i+1}} \phi_i \phi_j dx$. By drawing the basis functions it is seen that most of them are zero in the same two elements, and only $j = i-1, i, i+1$ gives non-zero products.

Figure A.2 shows an element between two nodes. Only two basis functions are non-zero in that element. The different elements are identical with regards to this, and it is usually easier to perform the integrations in terms of local node number and local basis functions. Then

$$\begin{aligned} \int_{x_1}^{x_2} \phi_1 \phi_2 dx &= \frac{\Delta x}{6} \\ \int_{x_1}^{x_2} \phi_1 \phi_1 dx &= \int_{x_1}^{x_2} \phi_2 \phi_2 dx = \frac{\Delta x}{3} \end{aligned} \tag{A.17}$$

and

$$\begin{aligned} \int_{x_1}^{x_2} \frac{\partial \phi_1}{\partial x} \phi_1 dx &= \int_{x_1}^{x_2} \frac{\partial \phi_1}{\partial x} \phi_2 dx = -\frac{1}{2} \\ \int_{x_1}^{x_2} \frac{\partial \phi_2}{\partial x} \phi_1 dx &= \int_{x_1}^{x_2} \frac{\partial \phi_2}{\partial x} \phi_2 dx = \frac{1}{2} \end{aligned} \tag{A.18}$$

The expressions in local numbers form the building blocks for $\langle \phi_i \phi_j \rangle$ and $\left\langle \frac{\partial \phi_j}{\partial x} \phi_i \right\rangle$. The integration is thus performed element by element in terms of local node numbers and summed to give the full inner products. This is called the assembly process.

In the general case all elements may be of different sizes. For simplicity it is assumed here

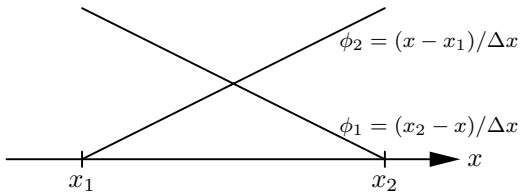


Figure A.2: Local basis functions in an element of length $\Delta x$.

that all elements have the same size, $\Delta x$. Then

$$\begin{aligned}
\langle \phi_i \phi_j \rangle &= 0, \qquad j \neq i-1, i, i+1 \\
\langle \phi_i \phi_{i-1} \rangle &= \langle \phi_{i-1} \phi_i \rangle = \int_{x_{i-1}}^{x_i} \phi_{i-1}\phi_i dx = \int_{x_1}^{x_2} \phi_1 \phi_2 dx = \frac{\Delta x}{6} \\
\langle \phi_i \phi_i \rangle &= \int_{x_{i-1}}^{x_i} \phi_i \phi_i dx + \int_{x_i}^{x_{i+1}} \phi_i \phi_i dx = \int_{x_1}^{x_2} \phi_2 \phi_2 dx + \int_{x_1}^{x_2} \phi_1 \phi_1 dx = \frac{2\Delta x}{3} \\
\langle \phi_i \phi_{i+1} \rangle &= \langle \phi_{i+1} \phi_i \rangle = \int_{x_i}^{x_{i+1}} \phi_i \phi_{i+1} dx = \int_{x_1}^{x_2} \phi_1 \phi_2 dx = \frac{\Delta x}{6}
\end{aligned} \tag{A.19}$$

and

$$\begin{aligned}
\left\langle \frac{\partial \phi_j}{\partial x} \phi_i \right\rangle &= 0, \qquad j \neq i-1, i, i+1 \\
\left\langle \frac{\partial \phi_{i-1}}{\partial x} \phi_i \right\rangle &= \int_{x_1}^{x_2} \frac{\partial \phi_1}{\partial x} \phi_2 dx = -\frac{1}{2} \\
\left\langle \frac{\partial \phi_i}{\partial x} \phi_i \right\rangle &= \int_{x_1}^{x_2} \frac{\partial \phi_2}{\partial x} \phi_2 dx + \int_{x_1}^{x_2} \frac{\partial \phi_1}{\partial x} \phi_1 dx = 0 \\
\left\langle \frac{\partial \phi_{i+1}}{\partial x} \phi_i \right\rangle &= \int_{x_1}^{x_2} \frac{\partial \phi_2}{\partial x} \phi_1 dx = \frac{1}{2}
\end{aligned} \tag{A.20}$$

The time variation is treated with the finite difference method in the sea ice and ocean models described in chapter 4 and 5. It will be so here as well, involving $\frac{\partial c_j}{\partial t}$ on the left hand side of eq. A.16. By collecting the $c_j$'s in a vector $\vec{c}$ the weak formulation (eq. A.16) is written in vector notation

$$A\vec{c}^{n+1} = \vec{b} \tag{A.21}$$

where the vector $\vec{b}$ includes all terms at known time levels. The matrix $A$ is defined by the dependency of the nodes on each other. Two steps are thus needed in the model. First perform the integrations for each $i$ and $j$ to get the elements in $A$ and $\vec{b}$ (the assembly process) and then solve the system of linear equations.

In explicit form the right hand side of eq. A.16 is calculated at time level $n$ to give

$$\sum_{j=1}^{N} c_j^{n+1} \langle \phi_i \phi_j \rangle = \sum_{j=1}^{N} c_j^n \langle \phi_i \phi_j \rangle - u\Delta t \sum_{j=1}^{N} c_j^n \left\langle \frac{\partial \phi_j}{\partial x} \phi_i \right\rangle \tag{A.22}$$

By inserting eqs. A.19 and A.20, $A$ and $\vec{b}$ are found to be

$$A = \begin{pmatrix} 2/3 & 1/6 & 0 & 0 & \\ 1/6 & 2/3 & 1/6 & 0 & \dots \\ 0 & 1/6 & 2/3 & 1/6 & \\ 0 & 0 & 1/6 & 2/3 & \\ & \vdots & & & \ddots \end{pmatrix} \tag{A.23}$$

and

$$b_i = \frac{1}{6} c_{i-1}^n + \frac{2}{3} c_i^n + \frac{1}{6} c_{i+1}^n - u \frac{\Delta t}{2\Delta x} \left( c_{i+1}^n - c_{i-1}^n \right) \tag{A.24}$$

$A$ is constant in time and therefore calculated only once.

One of the advantages of the finite element method is the possibility of a varying resolution. Nevertheless the example here is for constant element size $\Delta x$, that has been divided through the equations. The similarity to the explicit finite difference method (eq. A.5) is seen. This is so in the case of constant element size and will be more clear below in the discussion of nodal quadrature.

In implicit form the right hand side of eq. A.16 is calculated at time level $n+1$ to give

$$\sum_{j=1}^{N} c_j^{n+1} \langle \phi_i \phi_j \rangle + u\Delta t \sum_{j=1}^{N} c_j^{n+1} \left\langle \frac{\partial \phi_j}{\partial x} \phi_i \right\rangle = \sum_{j=1}^{N} c_j^n \langle \phi_i \phi_j \rangle \tag{A.25}$$

By inserting eqs. A.19 and A.20 $A$ and $\vec{b}$ are found to be

$$A = \begin{pmatrix} 2/3 & 1/6 + u\frac{\Delta t}{2\Delta x} & 0 & 0 & \\ 1/6 - u\frac{\Delta t}{2\Delta x} & 2/3 & 1/6 + u\frac{\Delta t}{2\Delta x} & 0 & \dots \\ 0 & 1/6 - u\frac{\Delta t}{2\Delta x} & 2/3 & 1/6 + u\frac{\Delta t}{2\Delta x} & \\ 0 & 0 & 1/6 - u\frac{\Delta t}{2\Delta x} & 2/3 & \\ & \vdots & & & \ddots \end{pmatrix} \tag{A.26}$$

and

$$b_i = \frac{1}{6} c_{i-1}^n + \frac{2}{3} c_i^n + \frac{1}{6} c_{i+1}^n \tag{A.27}$$

With the finite difference method it was seen that the explicit method solves directly for $c_j^{n+1}$, while in the implicit method $c_j^{n+1}$ depends on the neighbour points, and a system of linear equations must be solved. With the finite element method both the explicit and the implicit method give a system of linear equations. In the explicit method $A$ is usually constant in time and is only calculated once. In the implicit method this is not the case in general, and $A$ must be calculated every time step. Though, the computationally most expensive part is usually solving the system of linear equations. This work is reduced by the nodal quadrature.

The integrals in eqs. A.19 and A.20 are calculated analytically. The integration might instead be performed numerically as a summation over some given points, this is called quadrature. When the quadrature points coincide with the nodes, it is called nodal quadrature. It is noted that

$$\begin{aligned} \phi_1 = 1, \quad \phi_2 = 0 \quad & \text{for } x = x_1 \\ \phi_1 = 0, \quad \phi_2 = 1 \quad & \text{for } x = x_2 \\ \frac{\partial \phi_1}{\partial x} = -\frac{1}{\Delta x}, \quad \frac{\partial \phi_2}{\partial x} = \frac{1}{\Delta x} \quad & \text{for } x = x_1, x_2 \end{aligned} \tag{A.28}$$

Then using nodal quadrature

$$\begin{aligned} \int_{x_1}^{x_2} \phi_1 \phi_2 dx &= \frac{\Delta x}{2} [\phi_1(x_1)\phi_2(x_1) + \phi_1(x_2)\phi_2(x_2)] = 0 \\ \int_{x_1}^{x_2} \phi_1 \phi_1 dx &= \frac{\Delta x}{2} [\phi_1(x_1)\phi_1(x_1) + \phi_1(x_2)\phi_1(x_2)] = \frac{\Delta x}{2} \\ \int_{x_1}^{x_2} \phi_2 \phi_2 dx &= \frac{\Delta x}{2} [\phi_2(x_1)\phi_2(x_1) + \phi_2(x_2)\phi_2(x_2)] = \frac{\Delta x}{2} \end{aligned} \tag{A.29}$$

and eq. A.19 is simplified to

$$\langle \phi_i \phi_j \rangle = \begin{cases} 0 & i \neq j \\ \Delta x & i = j \end{cases} \tag{A.30}$$

Equation A.18 is unchanged, and so is eq. A.20. Inserting eqs. A.30 and A.20 into the explicit weak formulation (eq. A.22) gives the advection equation in explicit form using nodal quadrature. Then $A$ becomes the identity matrix

$$A = \begin{pmatrix} 1 & 0 & 0 & 0 & \\ 0 & 1 & 0 & 0 & \dots \\ 0 & 0 & 1 & 0 & \\ 0 & 0 & 0 & 1 & \\ & \vdots & & & \ddots \end{pmatrix} \tag{A.31}$$

and

$$b_i = c_i^n - u\frac{\Delta t}{2\Delta x}\left(c_{i+1}^n - c_{i-1}^n\right) \tag{A.32}$$

It is seen that this is actual the same system of linear equations as found with the explicit finite difference method (eq. A.5).

The same happens in the implicit case. Inserting eqs. A.30 and A.20 into the implicit weak formulation (eq. A.25) gives $b_i = 1$ and $A$ identical to what is found in the finite difference case (eq. A.8). Thus in this simple example with constant grid and element size in the two discrete methods respectively, the finite element method using nodal quadrature actual leads to the same algorithm as the finite difference method. This is explained by the fact that with nodal quadrature, only information from the nodes are used as within the finite difference method. In contrary the full finite element method uses the information from the entire element giving a different weighting of the neighbour nodes.

# Appendix B

# Condition number and the power method

The condition number $\kappa$ mentioned in section 4.5.3 is a measure of the efficiency of the conjugate gradient method. The condition number for a matrix $M$ is defined as

$$\kappa = \|M\| \cdot \|M^{-1}\| \tag{B.1}$$

where $\|M\|$ is some matrix norm. The condition number therefore varies, depending on which matrix norm is used. The definition might not be easy to use directly. First inverting the matrix to get $M^{-1}$ and then taking the norm can be very demanding. It can be shown (e.g. Schwarz, 1989) that the spectral norm equals the largest eigenvalue

$$\|M\| = \max|\lambda| \tag{B.2}$$

Since the eigenvalues of $M^{-1}$ are the reciprocals of the eigenvalues $M$ the condition number can be defined either as the multiplication of the largest eigenvalues of $M$ and $M^{-1}$ or as the ratio of the largest to the smallest eigenvalue of $M$

$$\kappa = \max|\lambda_M| \cdot \max|\lambda_{M^{-1}}| = \frac{\max|\lambda_M|}{\min|\lambda_M|} \tag{B.3}$$

The conjugate gradient method without preconditioning solves the system of linear equation $A\vec{x} = \vec{b}$ (see section 4.5.3). In this study $A$ is real and symmetric, and the eigenvalues $\lambda$ are therefore real. The largest eigenvalue is calculated by the power method (see e.g. Van de Velde, 1994). This is an iterative method, where a vector chosen at random is multiplied by $A$ a number of times. Thus the multiplication

$$\vec{x}_{k+1} = A\vec{x}_k \tag{B.4}$$

is iterated, always scaling $\vec{x}_k$ to unit length due to reasons of accuracy. After a number of iterations $\vec{x}_k$ approaches the eigenvector corresponding to the largest eigenvalue. Then $\lambda$ is calculated by exploiting that $\vec{x}_{k+1} = A\vec{x}_k = \lambda\vec{x}_k$.

The largest eigenvalue of $A^{-1}$ is found through an iteration of

$$A\vec{x}_{k+1} = \vec{x}_k \tag{B.5}$$

instead of eq. B.4. In each iteration the system of linear equations (eq. B.5) must be solved. This is performed with the LU method, though since $A$ is symmetric and positive definite, this can be performed with the conjugate gradient method as well.

The preconditioned conjugate gradient method solves in principle $C^{-1}A\vec{x} = C^{-1}\vec{b}$, and the condition number for the matrix product $C^{-1}A$ defines the efficiency of the method. $C^{-1}A$ is not symmetric, and the eigenvalues may therefore be complex. Since the matrix is real the complex eigenvalues occur in complex conjugate pairs. Here the power method is used to find the numerically largest pair. After a number of iterations $\vec{x}_k$ approaches a linear combination of the two eigenvectors corresponding to the largest pair. Thus three vectors $\vec{x}_{k+2}$, $\vec{x}_{k+1}$ and $\vec{x}_k$ is needed to calculate the eigenvalues, and the matrix norm is equal to the absolute value of the eigenvalues. In this case only the LU method is useful for eq. B.5. The conjugate gradient method is not suitable, since $(C^{-1}A)^{-1}$ is not symmetric.

# Appendix C

# Internet addresses

Except for the wind fields and the digitised ice maps, which are both produced by the Danish Meteorological Institute, all data and models that have been used in this study are freely available on the internet. Here is a list of links, that can be useful for students and other people, who would like to retrieve some of them. The grid generation and all the plotting for the finite elements simulations is made with the program Xscan/Genesis. It is, as far is known, free, but there seems currently not to exist an official web-site. A version may be available via the Quoddy User's Group. The sea ice model developed in this study, is currently not on the net, but is available from the author.

## Models

**Quoddy User's Group,** http://www-nml.dartmouth.edu/quoddy/QUG.html

**Finite element models,** http://www-nml.dartmouth.edu/Software
Source code for Quoddy, Fundy among others.

**POM,** http://www.aos.princeton.edu/WWWPUBLIC/htdocs.pom
Information about POM, link to source code, etc.

## Data bases

**Climate data library,** http://ingrid.ldgo.columbia.edu
ETOPO5, Levitus climatology, and much more.

**Coastline Extractor,** http://crusty.er.usgs.gov/coast/getcoast.html
Different coastline databases.

**Ice maps,** http://www.dmi.dk/vejr/gron/index.html
Ice maps and weather forecast for Greenland (in Danish)

# References


Adcroft, A., and D. Marshall, 1998: How slippery are piecewise-constant coastlines in numerical ocean models. *Tellus*, **50A**, 95–108.

Barrett, R., M. Berry, T. F. Chan, J. Demmel, J. Donato, J. Dongarra, V. Eijkhout, R. Pozo, C. Romine, and H. V. der Vorst, 1994: *Templates for the Solution of Linear Systems: Building Blocks for Iterative Methods, 2nd Edition*. SIAM, Philadelphia, PA, URL `http://www.netlib.org/templates/Templates.html`.

Beckmann, A., and D. B. Haidvogel, 1993: Numerical simulation of flow around a tall isolated seamount. part i: Problem formulation and model accuracy. *Journal of Physical Oceanography*, **23**, 1736–1753.

Blumberg, A. L., and G. L. Mellor, 1987: A describtion of a three-dimensional coastal ocean circulation model. *Three-Dimensional Coastal Ocean Models*, N. Heaps, ed., AGU, Washington, DC, vol. 4, pp. 1–16.

Cheng, A., and R. H. Preller, 1992: An ice-ocean coupled model for the northern hemisphere. *Geophysical Research Letters*, **19**, 901–904.

Dietrich, G., K. Kalle, W. Krauss, and G. Siedler, 1980: *General Oceanography, An Introduction*. John Wiley, New York, second edn.

Ezer, T., and G. L. Mellor, 1994: Diagnostic and prognostic calculations of the North Atlantic circulation and sea level using a sigma coordinate ocean model. *Journal of Geophysical Research*, **99**, 14 159–14 171.

—, 1997: Simulations of the Atlantic Ocean with a free surface sigma coordinate ocean model. *Journal of Geophysical Research*, **102**, 15 647–15 657.

Flato, G. M., 1993: A particle-in-cell sea-ice model. *Atmosphere-Ocean*, **31**, 339–358.

—, 1998: The thickness variable in sea-ice models. *Atmosphere-Ocean*, **36**, 29–36.

Flato, G. M., and W. D. Hibler, III, 1992: Modeling pack ice as a cavitating fluid. *Journal of Physical Oceanography*, **22**, 626–651.

Foreman, M. G. G., and R. E. Thomson, 1997: Three-dimensional model simulations of tides and buoyancy currents along the west coast of vancouver island. *Journal of Physical Oceanography*, **27**, 1300–1325.

Fortunato, A. B., and A. M. Baptista, 1996: Evaluation of horizontal gradients in sigma coordinates shallow water models. *Atmosphere-Ocean*, **34**, 489–514.

Gan, J., L. A. Mysak, and D. N. Straub, 1998: Simulations of the South Atlantic Ocean circulation and its seasonal variability. *Journal of Geophysical Research*, **103**, 10 241–10 251.

Gill, R. S., 1998: Evaluation of the RADARSAT imagery for the operational mapping of sea ice around Greenland in 1997. Scientific Report 98-5, DMI, Copenhagen, Denmark.

Gill, R. S., and H. H. Valeur, 1996: Evaluation of the RADARSAT imagery for the operational mapping of sea ice around Greenland. Scientific Report 96-9, DMI, Copenhagen, Denmark.

—, 1999: Ice cover discrimination in the Greenland waters using first-order texture parameters of

ERS SAR images. *International Journal of Remote Sensing*, **20**, 373–385.

Giraldo, F. X., 1997: Lagrange-Galerkin methods on spherical geodesic grids. *Journal of Computational Physics*, **136**, 197–213.

Golub, G. H., and C. F. Van Loan, 1989: *Matrix Computations*. Johns Hopkins University Press.

Gouretski, V. V., and K. Jancke, 1998: A new World Ocean Climatology: optimal interpolation of historical and WOCE hydrographic data on neutral surfaces. WOCE Report 162/98, WOCE. WHP SAC Technical Report No. 3.

Greenberg, D. A., F. E. Werner, and D. R. Lynch, 1998: A diagnostic finite-element ocean circulation model in sperical-polar coordinates. *Journal of Atmospheric and Oceanic Technology*, **15**, 942–958.

Grey, S. M., and K. Haines, 1999: Climatological hydrography of the North Atlantic. *Int. WOCE Newsl.*, **36**, 23–25.

Haidvogel, D. B., and A. Beckmann, 1999: *Numerical Ocean Circulation Modeling*. Imperical College Press, London, UK.

Häkkinen, S., 1990: Models and their applications to polar oceanography. *Polar Oceanography*, W. O. Smith, Jr., ed., Academic Press, San Diego, California, pp. 335–384.

—, 1993: An arctic source for the great salinity anomaly: a simulation of the arctic ice-ocean system. *Journal of Geophysical Research*, **98**, 16 379–16 410.

—, 1999: Variability of the simulated meridional heat transport in the North Atlantic for the period 1951-1993. *Journal of Geophysical Research*, **104**, 10 991–11 007.

Haney, R. L., 1991: On the pressure gradient force over steep topography in sigma coordinate ocean models. *Journal of Physical Oceanography*, **21**, 610–619.

Harder, M., 1997: Roughness, age and drift trajectories of sea ice in large-scale simulations and their use in model verifications. *Annales Geophysicæ*, **25**, 237–240.

Harder, M., and H. Fischer, 1999: Sea ice dynamics in the Weddell Sea with an optimized model. *Journal of Geophysical Research*, **104**, 11 151–11 162.

Harder, M., P. Lemke, and M. Hilmer, 1998: Simulation of sea ice transport through Fram Strait: Natural variability an sensitivity to forcing. *Journal of Geophysical Research*, **103**, 5595–5606.

Hibler, W. D., III, 1979: A dynamic thermodynamic sea ice model. *Journal of Physical Oceanography*, **9**, 817–846.

Hibler, W. D., III, and G. M. Flato, 1992: Sea ice models. *Climate System Modeling*, K. E. Trenberth, ed., Cambridge University Press, pp. 413–436.

Holland, D. M., L. A. Mysak, and J. M. Oberhuber, 1996: Simulation of the mixed-layer circulation in the Arctic Ocean. *Journal of Geophysical Research*, **101**, 1111–1128.

Hunke, E. C., and J. K. Dukowicz, 1997: An elastic-viscous-plastic model for sea ice dynamics. *Journal of Physical Oceanography*, **27**, 1849–1867.

Hunke, E. C., and Y. Zhang, 1999: A comparison of sea ice dynamics models at high resolution. *Monthly Weather Review*, **127**, 396–408.

Jackett, D. R., and T. J. McDougall, 1995: Minimal adjustment of hydrographic profiles to achieve static stability. *Journal of Atmospheric and Oceanic Technology*, **12**, 381–389.

Johannessen, O. M., S. Sandven, W. P. Budgell, J. A. Johannessen, and R. A. Shuchman, 1994: Observation and simulation of ice tongues and vortex pairs in the marginal ice zone. *The Polar Oceans and Their Role in Shaping the Global Environment*, O. M. Johannessen, R. D. Muench, and J. E. Overland, eds., AGU, Washington, DC, vol. 85 of *Geophysical Monograph*, pp. 109–136.

Johnson, C., 1987: *Numerical solution of partial differential equations by the finite element method*. Studentlitteratur, Lund, Sweden.

Källén, E., 1996: HIRLAM documentation manual. System 2.5. Tech. rep., SMHI, Norrköping, Sweden.

Kliem, N., and J. D. Pietrzak, 1999: On the pressure gradient error in sigma coordinate ocean models: A comparison with a laboratory experiment. *Journal of Geophysical Research*, **104**, 29 781–29 800.

Kowalik, Z., and T. S. Murty, 1993: *Numerical modeling of ocean dynamics*. World Scientific, Singapore.

Krauss, W., 1995: Currents and mixing in the Irminger Sea and the Iceland Basin. *Journal of Geophysical Research*, **100**, 10 851–10 871.

Kreyscher, M., M. Harder, and P. Lemke, 1997: First results of the Sea-Ice Model Intercomparison Project (SIMIP). *Annales Geophysicæ*, **25**, 8–11.

Kreyszig, E., 1988: *Advanced engineering mathematics*. John Wiley & Sons, New York, sixth edn.

Lemke, P., W. D. Hibler, G. M. Flato, M. Harder, and M. Kreyscher, 1997: On the improvement of sea-ice models for climate simulations: the Sea Ice Model Intercomparison Project. *Annales Geophysicæ*, **25**, 183–187.

Leppäranta, M., 1998: The dynamics of sea ice. *Physics of Ice-Covered Seas*, M. Leppäranta, ed., Helsinki University Printing House, Helsinki, Finland, vol. 1, pp. 305–342.

Levitus, S., and T. P. Boyer, 1994: World Ocean Atlas 1994 Volume 4: Temperature. NOAA Atlas NESDIS 4. U.S. Department of Commerce, Washington, D.C. 117 pp.

Levitus, S., R. Burgett, and T. P. Boyer, 1994: World Ocean Atlas 1994 Volume 3: Salinity. NOAA Atlas NESDIS 3. U.S. Department of Commerce, Washington, D.C. 99 pp.

Lu, Q.-M., J. Larsen, and P. Tryde, 1989: On the role of ice interaction due to floe collisions in marginal ice zone dynamics. *Journal of Geophysical Research*, **94**, 14 525–14 737.

Lynch, D. R., and W. R. Gray, 1979: A wave equation model for finite element tidal computations. *Comput. Fluids*, **7**, 207–228.

Lynch, D. R., J. T. C. Ip, C. E. Namie, and F. E. Werner, 1996: Comprehensive coastal ciculation model with application to the Gulf of Maine. *Continental Shelf Res.*, **16**, 875–906.

Lynch, D. R., and F. E. Werner, 1987: Three-dimensional hydrodynamics on finite elements. Part I: Linearized harmonic model. *Int. J. Numer. Methods Fluids*, **7**, 871–909.

—, 1991: Three-dimensional hydrodynamics on finite elements. Part II: Non-linear time-stepping model. *Int. J. Numer. Methods Fluids*, **12**, 507–533.

Lynch, D. R., F. E. Werner, D. A. Greenberg, and J. W. Loder, 1992: Diagnostic model for baroclinic, wind-driven and tidal circulation in shallow seas. *Continental Shelf Res.*, **12**, 37–64.

Makshtas, A. P., 1998: Thermodynamics of sea ice. *Physics of ice-covered seas*, M. Leppäranta, ed., Helsinki University Printing House, Helsinki, Finland, vol. 1, pp. 289–304.

Martinsen, E. A., and H. Engedahl, 1987: Implementation and testing of a lateral boundary scheme as an open boundary condition in a barotropic ocean model. *Coastal Eng.*, **11**, 603–627.

McCalpin, J. D., 1994: A comparison af second-order and fourth-order pressure gradient algorithms in a $\sigma$-co-ordinate ocean model. *Int. J. Numer. Methods Fluids*, **18**, 361–383.

McClimans, T. A., 1990: The role of laboratory experiments and models in the study of sea straits. *The Physical Oceanography of Sea Straits*, L. J. Pratt, ed., Academic, San Diego, Calif., pp. 373–388.

McClimans, T. A., J. H. Nilsen, and B. O. Johannessen, 1996: Laboratory simulation of the ocean circulation in the skagerrak. Tech. Rep. STF22 F96201, The Foundation of Scientific and Industrial Research at the Norwegian Institute of Technology, Trondheim, Norway.

McClimans, T. A., J. D. Pietrzak, V. Huess, N. Kliem, J. H. Nilsen, and B. O. Johannessen, 2000:

Laboratory and numerical simulation of the Skagerrak circulation. *Continental Shelf Res.*, **20**, 941–974.

McLaren, A. S., R. H. Bourke, J. E. Walsh, and R. L. Weaver, 1994: Variability in sea-ice thickness over the North Pole from 1958 to 1992. *The Polar Oceans and Their Role in Shaping the Global Environment*, O. M. Johannessen, R. D. Muench, and J. E. Overland, eds., AGU, Washington, DC, vol. 85 of *Geophysical Monograph*, pp. 363–371.

Mellor, G. L., 1991: An equation of state for numerical models of ocean and estuaries. *Journal of Atmospheric and Oceanic Technology*, **8**, 609–611.

—, 1996: *Introduction to Physical Oceanography*. AIP Press, Woodbury, New York.

Mellor, G. L., T. Ezer, and L. Y. Oey, 1994: The pressure gradient conundrum of sigma coordinate ocean models. *Journal of Atmospheric and Oceanic Technology*, **11**, 1126–1134.

Mellor, G. L., and S. Häkkinen, 1994: A review of coupled ice-ocean models. *The Polar Oceans and Their Role in Shaping the Global Environment*, O. M. Johannessen, R. D. Muench, and J. E. Overland, eds., AGU, Washington, DC, vol. 85 of *Geophysical Monograph*, pp. 21–31.

Mellor, G. L., and T. Yamada, 1982: Development of a turbulens closure model for geophysical fluid problems. *Reviews of Geophysics and Space Physics*, **20**, 851–875.

Meyers, P. G., and A. J. Weaver, 1995: A diagnostic barotropic finite-element ocean circulation model. *Journal of Atmospheric and Oceanic Technology*, **12**, 511–526.

Mortensen, J., 1997: *Satellite Altimetry and Circulation in the Denmark Strait and adjacent Seas*. Ph.D. thesis, University of Copenhagen, Department of Geophysics.

NGDC, 1988: Digital relief of the Surface of the Earth. Data Announcement 88-MGG-02, National Geophysical Data Center, NOAA, Boulder, Colorado, URL `http://www.ngdc.noaa.gov/mgg/global/etopo5.HTML`.

Nielsen, N. W., 1998: Inclusion of free convection and a smooth sea surface in the parameterization of surface fluxes over sea. *Hirlam Newsletter*, **32**, 44–51.

Omstedt, A., L. Nyberg, and M. Leppäranta, 1994: A coupled ice-ocean model supporting winter navigation in the Baltic Sea. Part 1. Ice dynamics and water levels. SMHI RO 17, SMHI, Norrköping, Sweden.

Parkinson, C. L., and W. M. Washington, 1979: A large-scale numerical model of sea ice. *Journal of Geophysical Research*, **84**, 311–337.

Pietrzak, J. D., 1998: The use of TVD limiters for forward-in-time upstream-biased advection schemes in ocean modeling. *Monthly Weather Review*, **126**, 812–830.

Pond, S., and G. L. Pickard, 1983: *Introductory Dynamical Oceanography*. Pergamon Press, Oxford, England, second edn.

Preller, R. H., 1999: Prediction in ice-covered shallow seas. *Coastal Ocean Prediction*, C. N. K. Mooers, ed., AGU, Washington, DC, vol. 56 of *Coastal and Estuarine Studies*, pp. 405–441.

Rasmussen, E., J. Pietrzak, and R. Brandt, 1999: A coupled ice-ocean model for the Greenland, Iceland and Norwegian Seas. *Deep-Sea Research*, **46**, 1169–1198.

Riedlinger, S. H., and R. H. Preller, 1991: The development of a coupled ice-ocean model for forecasting ice conditions in the Arctic. *Journal of Geophysical Research*, **96**, 16 955–16 977.

Schewchuk, J. R., 1994: An introduction to the conjugate gradient method without the agonizing pain, URL `http://www.cs.cmu.edu/ quake-papers/painless-conjugate-gradient.ps`.

Schmitz, W. J., and M. S. McCartney, 1993: On the North Atlantic circulation. *Reviews of Geophysics*, **31**, 29–49.

Schulkes, R. M. S. M., L. W. Morland, and R. Staroszczyk, 1998: A finite-element treatment of sea ice dynamics for different ice rheologies. *Int. J. Numer. Anal. Meth. Geomech.*, **22**, 153–174.

Schwarz, H. R., 1989: *Numerical Analysis: A Comprehensive Introduction*. John Wiley & Sons, Chichester, UK.

Slørdal, L. H., 1997: The pressure gradient force in sigma-co-ordinate ocean models. *Int. J. Numer. Methods Fluids*, **24**, 987–1017.

Stelling, G. S., and J. A. T. M. van Kester, 1994: On the approximation of horizontal gradients in sigma co-ordinates for bathymetry with steep bottom slopes. *Int. J. Numer. Methods Fluids*, **18**, 915–935.

Svendsen, E., J. Berntsen, M. Skogen, B. Ådlandsvik, and E. Martinsen, 1996: Model simulation of the skagerrak circulation and hydrography during Skagex. *J. Mar. Sys.*, **8**, 219–236.

Sykes, J. F., and J. D. Miller-Cushon, 1992a: Adjoint sensitivity theory for a pack ice momentum model. *Can. Geotech. J.*, **29**, 881–889.

—, 1992b: Sensitivity analysis of ice motion near Adams Island. *Can. Geotech. J.*, **29**, 890–901.

Thomas, D., S. Martin, D. Rothrock, and M. Steele, 1996: Assimilating satellite concentration data into an Artic sae ice mass balance model,1979-1985. *Journal of Geophysical Research*, **101**, 20 849–20 868.

Thompson, N. R., and J. F. Sykes, 1990: Sensitivity and uncertainty analysis of a short-term sea ice motion model. *Journal of Geophysical Research*, **95**, 1713–1739.

Thompson, N. R., J. F. Sykes, and R. F. McKenna, 1988: Short-term ice motion modeling with application to the Beaufort Sea. *Journal of Geophysical Research*, **93**, 6819–6836.

Timokhov, L. A., 1998: Ice dynamics models. *Physics of ice-covered seas*, M. Leppäranta, ed., Helsinki University Printing House, Helsinki, Finland, vol. 1, pp. 343–380.

Tremblay, L.-B., and L. A. Mysak, 1997: Modeling sea ice as a granular material, including the dilatancy effect. *Journal of Physical Oceanography*, **27**, 2342–2360.

UNESCO, 1981: Tenth report of the joint panel on oceanographic tables and standards. *Technical Papers in Marine Science*, **36**, 24.

Uotila, J., J. Launianen, and T. Vihma, 1997: An analysis of buoy drift in the northern north atlantic with detection of drouge loss events. *Atmosphere-Ocean*, **35**, 471–494.

Van de Velde, E. F., 1994: *Concurrent Scientific Computing*, vol. 16 of *Texts in Applied Mathematics*. Springer Verlag, New York.

Vested, H. J., J. W. Nielsen, H. R. Jensen, and K. B. Kristensen, 1995: Skill assessment of an operational hydrodynamic forecast system for the North Sea and Danish Belts. *Quantitative Skill Assessment for Coastal Ocean Models*, D. R. Lynch and A. M. Davies, eds., no. 47 in Coastal and Estuarine Studies, AGU, Washington, DC, pp. 373–396.

Vinje, T., N. Nordlund, and Å. Kvambekk, 1998: Monitoring ice thickness in Fram Strait. *Journal of Geophysical Research*, **103**, 10 437–10 449.

Wheless, G. H., and A. Vale-Levinson, 1996: A modeling study of tidally driven estuarine exchange through a narrow inlet onto a sloping shelf. *Journal of Geophysical Research*, **101**, 25 675–25 687.

## DANISH METEOROLOGICAL INSTITUTE

### Scientific Reports

Scientific reports from the Danish Meteorological Institute cover a variety of geophysical fields, i.e. meteorology (including climatology), oceanography, subjects on air and sea pollution, geomagnetism, solar-terrestrial physics, and physics of the middle and upper atmosphere.

Reports in the series within the last five years:

No. 97-1
**E. Friis Christensen og C. Skøtt:** Contributions from the International Science Team. The Ørsted Mission - a pre-launch compendium

No. 97-2
**Alix Rasmussen, Sissi Kiilsholm, Jens Havskov Sørensen, Ib Steen Mikkelsen:** Analysis of tropospheric ozone measurements in Greenland: Contract No. EV5V-CT93-0318 (DG 12 DTEE): DMI's contribution to CEC Final Report Arctic Trophospheric Ozone Chemistry ARCTOC

No. 97-3
**Peter Thejll:** A search for effects of external events on terrestrial atmospheric pressure: cosmic rays

No. 97-4
**Peter Thejll:** A search for effects of external events on terrestrial atmospheric pressure: sector boundary crossings

No. 97-5
**Knud Lassen:** Twentieth century retreat of sea-ice in the Greenland Sea

No. 98-1
**Niels Woetman Nielsen, Bjarne Amstrup, Jess U. Jørgensen:** HIRLAM 2.5 parallel tests at DMI: sensitivity to type of schemes for turbulence, moist processes and advection

No. 98-2
**Per Høeg, Georg Bergeton Larsen, Hans-Henrik Benzon, Stig Syndergaard, Mette Dahl Mortensen:** The GPSOS project
Algorithm functional design and analysis of ionosphere, stratosphere and troposphere observations

No. 98-3
**Mette Dahl Mortensen, Per Høeg:**
Satellite atmosphere profiling retrieval in a nonlinear troposphere
Previously entitled: Limitations induced by Multipath

No. 98-4
**Mette Dahl Mortensen, Per Høeg:** Resolution properties in atmospheric profiling with GPS

No. 98-5
**R.S. Gill and M. K. Rosengren:** Evaluation of the Radarsat imagery for the operational mapping of sea ice around Greenland in 1997

No. 98-6
**R.S. Gill, H.H. Valeur, P. Nielsen and K.Q. Hansen:** Using ERS SAR images in the operational mapping of sea ice in the Greenland waters: final report for ESA-ESRIN's: pilot projekt no. PP2.PP2.DK2 and 2nd announcement of opportunity for the exploitation of ERS data projekt No. AO2..DK 102

No. 98-7
**Per Høeg et al.:** GPS Atmosphere profiling methods and error assessments

No. 98-8
**H. Svensmark, N. Woetmann Nielsen and A.M. Sempreviva:** Large scale soft and hard turbulent states of the atmosphere

No. 98-9
**Philippe Lopez, Eigil Kaas and Annette Guldberg:** The full particle-in-cell advection scheme in spherical geometry

No. 98-10
**H. Svensmark:** Influence of cosmic rays on earth's climate

No. 98-11
**Peter Thejll and Henrik Svensmark:** Notes on the method of normalized multivariate regression

No. 98-12
**K. Lassen:** Extent of sea ice in the Greenland Sea 1877-1997: an extension of DMI Scientific Report 97-5

No. 98-13
**Niels Larsen, Alberto Adriani and Guido DiDonfrancesco:** Microphysical analysis of polar stratospheric clouds observed by lidar at McMurdo, Antarctica

No.98-14

**Mette Dahl Mortensen:** The back-propagation method for inversion of radio occultation data

No. 98-15
**Xiang-Yu Huang:** Variational analysis using spatial filters

No. 99-1
**Henrik Feddersen:** Project on prediction of climate variations on seasonel to interannual timescales (PROVOST) EU contract ENVA4-CT95-0109: DMI contribution to the final report:Statistical analysis and post-processing of uncoupled PROVOST simulations

No. 99-2
**Wilhelm May:** A time-slice experiment with the ECHAM4 A-GCM at high resolution: the experimental design and the assessment of climate change as compared to a greenhouse gas experiment with ECHAM4/OPYC at low resolution

No. 99-3
**Niels Larsen et al.:** European stratospheric monitoring stations in the Artic II: CEC Environment and Climate Programme Contract ENV4-CT95-0136. DMI Contributions to the project

No. 99-4
**Alexander Baklanov:** Parameterisation of the deposition processes and radioactive decay: a review and some preliminary results with the DERMA model

No. 99-5
**Mette Dahl Mortensen:** Non-linear high resolution inversion of radio occultation data

No. 99-6
**Stig Syndergaard:** Retrieval analysis and methodologies in atmospheric limb sounding using the GNSS radio occultation technique

No. 99-7
**Jun She, Jacob Woge Nielsen:** Operational wave forecasts over the Baltic and North Sea

No. 99-8
**Henrik Feddersen:** Monthly temperature forecasts for Denmark - statistical or dynamical?

No. 99-9
**P. Thejll, K. Lassen:** Solar forcing of the Northern hemisphere air temperature: new data

No. 99-10
**Torben Stockflet Jørgensen, Aksel Walløe Hansen:** Comment on "Variation of cosmic ray flux and global coverage - a missing link in solar-climate relationships" by Henrik Svensmark and Eigil Friis-Christensen

No. 99-11
**Mette Dahl Meincke:** Inversion methods for atmospheric profiling with GPS occultations

No. 99-12
**Hans-Henrik Benzon; Laust Olsen; Per Høeg:** Simulations of current density measurements with a Faraday Current Meter and a magnetometer

No. 00-01
**Per Høeg; G. Leppelmeier:** ACE - Atmosphere Climate Experiment

No. 00-02
**Per Høeg:** FACE-IT: Field-Aligned Current Experiment in the Ionosphere and Thermosphere

No. 00-03
**Allan Gross:** Surface ozone and tropospheric chemistry with applications to regional air quality modeling. PhD thesis

No. 00-04
**Henrik Vedel:** Conversion of WGS84 geometric heights to NWP model HIRLAM geopotential heights

No. 00-05
**Jérôme Chenevez:** Advection experiments with DMI-Hirlam-Tracer

No. 00-06
**Niels Larsen**: Polar stratospheric clouds micro-physical and optical models

No. 00-07
**Alix Rasmussen**: "Uncertainty of meteorological parameters from DMI-HIRLAM"

No. 00-08
**A.L. Morozova**: Solar activity and Earth's weather. Effect of the forced atmospheric transparency changes on the troposphere temperature profile studied with atmospheric models

No. 00-09
**Niels Larsen, Bjørn M. Knudsen, Michael Gauss, Giovanni Pitari**: Effects from high-speed civil traffic aircraft emissions on polar stratospheric clouds

No. 00-10
**Søren Andersen:** Evaluation of SSM/I sea ice algorithms for use in the SAF on ocean and sea ice, July 2000

No. 00-11
**Claus Petersen, Niels Woetmann Nielsen:** Diagnosis of visibility in DMI-HIRLAM

No. 00-12

**Erik Buch:** A monograph on the physical oceanography of the Greenland waters

No. 00-13
**M. Steffensen:** Stability indices as indicators of lightning and thunder

No. 00-14
**Bjarne Amstrup, Kristian S. Mogensen, Xiang-Yu Huang:** Use of GPS observations in an optimum interpolation based data assimilation system

No. 00-15
**Mads Hvid Nielsen:** Dynamisk beskrivelse og hydrografisk klassifikation af den jyske kyststrøm

No. 00-16
**Kristian S. Mogensen, Jess U. Jørgensen, Bjarne Amstrup, Xiaohua Yang and Xiang-Yu Huang:** Towards an operational implementation of HIRLAM 3D-VAR at DMI

No. 00-17
**Sattler, Kai; Huang, Xiang-Yu:** Structure function characteristics for 2 meter temperature and relative humidity in different horizontal resolutions

No. 00-18
**Niels Larsen, Ib Steen Mikkelsen, Bjørn M. Knudsen m.fl.:** In-situ analysis of aerosols and gases in the polar stratosphere. A contribution to THESEO. Environment and climate research programme. Contract no. ENV4-CT97-0523. Final report

No. 00-19
**Amstrup, Bjarne:** EUCOS observing system experiments with the DMI HIRLAM optimum interpolation analysis and forecasting system

No. 01-01
**V.O. Papitashvili, L.I. Gromova, V.A. Popov and O. Rasmussen:** Northern polar cap magnetic activity index PCN: Effective area, universal time, seasonal, and solar cycle variations

No. 01-02
**M.E. Gorbunov:** Radioholographic methods for processing radio occultation data in multipath regions

No. 01-03
**Niels Woetmann Nielsen, Claus Petersen:** Calculation of wind gusts in DMI-HIRLAM

No. 01-04
**Vladimir Penenko; Alexander Baklanov:** Methods of sensitivity theory and inverse modeling for estimation of source parameter and risk/vulnerability areas

No. 01-05
**Sergej Zilitinkevich; Alexander Baklanov; Jutta Rost; Ann-Sofi Smedman, Vasiliy Lykosov and Pierluigi Calanca:** Diagnostic and prognostic equations for the depth of the stably stratified Ekman boundary layer

No. 01-06
**Bjarne Amstrup:** Impact of ATOVS AMSU-A radiance data in the DMI-HIRLAM 3D-Var analysis and forecasting system

No. 01-07
**Sergej Zilitinkevich; Alexander Baklanov:** Calculation of the height of stable boundary layers in operational models

No. 01-08
**Vibeke Huess:** Sea level variations in the North Sea – from tide gauges, altimetry and modelling

No. 01-09
**Alexander Baklanov and Alexander Mahura:** Atmospheric transport pathways, vulnerability and possible accidental consequences from nuclear risk sites: methodology for probabilistic atmospheric studies

No. 02-01
**Bent Hansen Sass and Claus Petersen:** Short range atmospheric forecasts using a nudging procedure to combine analyses of cloud and precipitation with a numerical forecast model

No. 02-02
**Erik Buch:** Present oceanographic conditions in Greenland waters

No. 02-03
**Bjørn M. Knudsen, Signe B. Andersen and Allan Gross:** Contribution of the Danish Meteorological Institute to the final report of SAMMOA. CEC contract EVK2-1999-00315: Spring-to.-autumn measurements and modelling of ozone and active species